

**DIRECTIONAL SOLIDIFICATION
CHARACTERISTICS OF HYPER-EUTECTIC Al-Cu
ALLOYS UNDER VARYING GRAVITY CONDITIONS**

by

Hong Yu

A thesis to the faculty of Graduate Studies in partial fulfilment
of the requirement for the degree of Master of Science

**Department of Mechanical & Industrial Engineering
Metallurgy Science Laboratory**

Winnipeg, Manitoba

1993



National Library
of Canada

Acquisitions and
Bibliographic Services Branch

395 Wellington Street
Ottawa, Ontario
K1A 0N4

Bibliothèque nationale
du Canada

Direction des acquisitions et
des services bibliographiques

395, rue Wellington
Ottawa (Ontario)
K1A 0N4

Your file Votre référence

Our file Notre référence

The author has granted an irrevocable non-exclusive licence allowing the National Library of Canada to reproduce, loan, distribute or sell copies of his/her thesis by any means and in any form or format, making this thesis available to interested persons.

L'auteur a accordé une licence irrévocable et non exclusive permettant à la Bibliothèque nationale du Canada de reproduire, prêter, distribuer ou vendre des copies de sa thèse de quelque manière et sous quelque forme que ce soit pour mettre des exemplaires de cette thèse à la disposition des personnes intéressées.

The author retains ownership of the copyright in his/her thesis. Neither the thesis nor substantial extracts from it may be printed or otherwise reproduced without his/her permission.

L'auteur conserve la propriété du droit d'auteur qui protège sa thèse. Ni la thèse ni des extraits substantiels de celle-ci ne doivent être imprimés ou autrement reproduits sans son autorisation.

ISBN 0-315-86108-8

Canadä

Name _____

Dissertation Abstracts International is arranged by broad, general subject categories. Please select the one subject which most nearly describes the content of your dissertation. Enter the corresponding four-digit code in the spaces provided.

Metallurgy

SUBJECT TERM

0743

SUBJECT CODE

U·M·I

Subject Categories

THE HUMANITIES AND SOCIAL SCIENCES

COMMUNICATIONS AND THE ARTS

Architecture	0729	Psychology	0525
Art History	0377	Reading	0535
Cinema	0900	Religious	0527
Dance	0378	Sciences	0714
Fine Arts	0357	Secondary	0533
Information Science	0723	Social Sciences	0534
Journalism	0391	Sociology of	0340
Library Science	0399	Special	0529
Mass Communications	0708	Teacher Training	0530
Music	0413	Technology	0710
Speech Communication	0459	Tests and Measurements	0288
Theater	0465	Vocational	0747

EDUCATION

General	0515
Administration	0514
Adult and Continuing	0516
Agricultural	0517
Art	0273
Bilingual and Multicultural	0282
Business	0688
Community College	0275
Curriculum and Instruction	0727
Early Childhood	0518
Elementary	0524
Finance	0277
Guidance and Counseling	0519
Health	0680
Higher	0745
History of	0520
Home Economics	0278
Industrial	0521
Language and Literature	0279
Mathematics	0280
Music	0522
Philosophy of	0998
Physical	0523

LANGUAGE, LITERATURE AND LINGUISTICS

Language	
General	0679
Ancient	0289
Linguistics	0290
Modern	0291
Literature	
General	0401
Classical	0294
Comparative	0295
Medieval	0297
Modern	0298
African	0316
American	0591
Asian	0305
Canadian [English]	0352
Canadian [French]	0355
English	0593
Germanic	0311
Latin American	0312
Middle Eastern	0315
Romance	0313
Slavic and East European	0314

PHILOSOPHY, RELIGION AND THEOLOGY

Philosophy	0422
Religion	
General	0318
Biblical Studies	0321
Clergy	0319
History of	0320
Philosophy of	0322
Theology	0469

SOCIAL SCIENCES

American Studies	0323
Anthropology	
Archaeology	0324
Cultural	0326
Physical	0327
Business Administration	
General	0310
Accounting	0272
Banking	0770
Management	0454
Marketing	0338
Canadian Studies	0385
Economics	
General	0501
Agricultural	0503
Commerce-Business	0505
Finance	0508
History	0509
Labor	0510
Theory	0511
Folklore	0358
Geography	0366
Gerontology	0351
History	
General	0578

THE SCIENCES AND ENGINEERING

BIOLOGICAL SCIENCES

Agriculture	
General	0473
Agronomy	0285
Animal Culture and Nutrition	0475
Animal Pathology	0476
Food Science and Technology	0359
Forestry and Wildlife	0478
Plant Culture	0479
Plant Pathology	0480
Plant Physiology	0817
Range Management	0777
Wood Technology	0746
Biology	
General	0306
Anatomy	0287
Biostatistics	0308
Botany	0309
Cell	0379
Ecology	0329
Entomology	0353
Genetics	0369
Limnology	0793
Microbiology	0410
Molecular	0307
Neuroscience	0317
Oceanography	0416
Physiology	0433
Radiation	0821
Veterinary Science	0778
Zoology	0472
Biophysics	
General	0786
Medical	0760
EARTH SCIENCES	
Biogeochemistry	0425
Geochemistry	0996

Geodesy	0370
Geology	0372
Geophysics	0373
Hydrology	0388
Mineralogy	0411
Paleobotany	0345
Paleoecology	0426
Paleontology	0418
Paleozoology	0985
Palynology	0427
Physical Geography	0368
Physical Oceanography	0415

HEALTH AND ENVIRONMENTAL SCIENCES

Environmental Sciences	0768
Health Sciences	
General	0566
Audiology	0300
Chemotherapy	0992
Dentistry	0567
Education	0350
Hospital Management	0769
Human Development	0758
Immunology	0982
Medicine and Surgery	0564
Mental Health	0347
Nursing	0569
Nutrition	0570
Obstetrics and Gynecology	0380
Occupational Health and Therapy	0354
Optphthalmology	0381
Pathology	0571
Pharmacology	0419
Pharmacy	0572
Physical Therapy	0382
Public Health	0573
Radiology	0574
Recreation	0575

PHYSICAL SCIENCES

Pure Sciences	
Chemistry	
General	0485
Agricultural	0749
Analytical	0486
Biochemistry	0487
Inorganic	0488
Nuclear	0738
Organic	0490
Pharmaceutical	0491
Physical	0494
Polymer	0495
Radiation	0754
Mathematics	0405
Physics	
General	0605
Acoustics	0986
Astronomy and Astrophysics	0606
Atmospheric Science	0608
Atomic	0748
Electronics and Electricity	0607
Elementary Particles and High Energy	0798
Fluid and Plasma	0759
Molecular	0609
Nuclear	0610
Optics	0752
Radiation	0756
Solid State	0611
Statistics	0463
Applied Sciences	
Applied Mechanics	0346
Computer Science	0984

PSYCHOLOGY

General	0621
Behavioral	0384
Clinical	0622
Developmental	0620
Experimental	0623
Industrial	0624
Personality	0625
Physiological	0989
Psychobiology	0349
Psychometrics	0632
Social	0451



DIRECTIONAL SOLIDIFICATION CHARACTERISTICS OF HYPER-EUTECTIC
Al-Cu ALLOYS UNDER VARYING GRAVITY CONDITIONS

BY

HONG YU

A Thesis submitted to the Faculty of Graduate Studies of the University of Manitoba in partial fulfillment of the requirements for the degree of

MASTER OF SCIENCE

© 1993

Permission has been granted to the LIBRARY OF THE UNIVERSITY OF MANITOBA to lend or sell copies of this thesis, to the NATIONAL LIBRARY OF CANADA to microfilm this thesis and to lend or sell copies of the film, and UNIVERSITY MICROFILMS to publish an abstract of this thesis.

The author reserves other publications rights, and neither the thesis nor extensive extracts from it may be printed or otherwise reproduced without the author's permission.

ACKNOWLEDGEMENTS

I would like to express my gratitude to Prof. K.N. Tandon and Prof. J.R. Cahoon for providing me the opportunity for this research and for their supervision.

Warm thanks are also extended to Mr. J. Van Dorp and Mr. Don Mardis, as well as other colleagues for their assistance and friendship.

Special thanks also go to the secretarial and support staff.

Finally, the author acknowledges the financial support from the Canadian Space Agency, as well as the technical assistance from the Bristol Aerospace Ltd. and Queen's University.

ABSTRACT

The present work deals with the solidification behaviour of hyper-eutectic Al-Cu alloys. Various aspects of solidification in the Al-Cu system were studied.

A three-zone gradients freeze QUESTS furnace was specially designed to carry out unidirectional solidification on ground as well as aboard the space shuttle. The experiments were carried out under different cooling conditions. The temperature gradients ranged from $G=2-5\text{ (K/mm)}$ and the cooling rates range from $3\times 10^{-2} - 1\text{ (K/s)}$. The microstructure features of Al-Cu were studied over a composition range from Al with 35-50wt% Cu. The faceting behaviour of primary Al_2Cu (θ) phase has been examined as a function of alloy composition and growth rate. Solidification in the microgravity of space environment promoted a dendrite growth of large primary θ phase. The fluid motion during solidification has been analyzed. Results indicate that lack of convection was the reason for large dendritic growth.

The spacings of primary θ phase and the inter θ -phase lamellar eutectic have been investigated. Smaller spacings between primary θ phase particles in ground-based sample have been observed. It is suggested that convective mixing present in the ground-based sample breaks off the fine dendrite arms of θ phase and distributes them throughout the melt providing nuclei for the growth of more θ phase particles. Mathematical analysis has shown that convection induced shear flow is too small to support this mechanism. Calculations have concentrated on analyzing the viscous stress at the solid surface and comparing it with the solid-liquid interface attachment energy. It has been concluded that the viscous stress due to natural convection disturbs the atoms not allowing them to incorporating into crystals. Furthermore, the physical motion of nucleation sites due to natural convection may provide more nuclei for the growth of θ phase particles. Therefore, the θ phase particles in the ground-based sample are smaller, more numerous and more finely spaced than the phase particles in the microgravity space sample.

The segregation phenomena of the hyper-eutectic Al-Cu alloys was also examined in both vertical and horizontal unidirectional solidification in unit gravity as well as in the microgravity environment. The longitudinal segregation in ground-based samples showed that the gravity driven natural convection is the main driving forces for fluid flow in the casting. However, in the case of vertical upwards solidification, the gravity effect is more pronounced. Lack of convection in the microgravity environment, where solidification contraction and maragoni convection are the only driving force for fluid flow, allowed large dendrites to grow. Moreover, solidification shrinkage is compensated mostly by deformation of the ingot rather than by interdendritic fluid flow. Therefore no significant macrosegregation is present in the ingot solidified in microgravity.

TABLE OF CONTENTS

ACKNOWLEDGEMENT	ii
ABSTRACT	iii
TABLE OF CONTENTS	v
LIST OF FIGURES	vii
LIST OF TABLES	xiv
CHAPTER I INTRODUCTION	1
CHAPTER II LITERATURE REVIEW	4
2-1 Solidification and Thermodynamics of Interfaces	4
2-1-1 Basic Concepts of Solidification	4
2-1-2 Thermodynamics of The Interface	10
2-2 Primary Phase Solidification	17
2-2-1 Dendritic Growth	17
2-2-2 Faceted Growth	22
2-3 Eutectic Solidification	33
2-3-1 Regular Eutectic Growth	33
2-3-2 Irregular Eutectic Growth	37
2-3-3 Hypo- and Hyper-eutectic Al-Cu Alloys	39
2-4 Segregation	42
2-4-1 Microsegregation	42
2-4-2 Macrosegregation	51
2-4-2-1 Normal Segregation	51
2-4-2-2 Inverse Segregation	52
2-4-2-3 Gravity Segregation	60
2-5 Effect of Convection	61
2-6 Microgravity Experiments	69
2-7 Proposed Research	72
CHAPTER III EXPERIMENTAL TECHNIQUES AND PROCEDURE	74
3-1 Preparation of Alloys	74

3-2	Test Specimens and Apparatus Used	75
3-3	Macro- and Microstructure Examination	86
3-4	Macrosegregation Analysis	86
3-5	Measurement of Spacings	87
3-6	Microgravity Samples	89
CHAPTER IV EXPERIMENTAL RESULTS AND DISCUSSION.....		91
4-1	Cooling Characteristic	91
4-2	Macrostructure of the Specimens	97
4-3	Microstructure of Hypereutectic Al-Cu Alloys	103
4-4	Inter-particle and Dendritic Spacings.....	117
4-5	Macrosegregation of the Specimen	123
4-5-1	Macrosegregation in Series A Samples	123
4-5-2	Macrosegregation in Series B Sample	127
4-5-3	Macrosegregation in Series C Samples	131
4-6	K-C 135 Samples	138
4-6-1	Macro- and Micro-structure	138
4-6-2	Macrosegregation	145
4-6-3	Dendritic Arm Spacings	151
4-7	Attachment Energy for Solid-liquid interface of AL ₂ Cu.....	152
4-8	Effect of Convection on Al ₂ Cu Growth	156
CHAPTER V CONCLUSIONS		162
REFERENCES		164

LIST OF FIGURES

Page	
3	Figure 1.1 The Al-Cu phase diagram[6].
9	Figure 2.1 The composition and temperature profiles for plane front solidification[6]. (a) Constrained growth during plane front solidification (b) Schematic profiles of solute concentration (c) Temperature profile
15	Figure 2.2 Curves of relative surface free energy as a function of occupied fraction of surface sites, related to the quantity α [5].
16	Figure 2.3 The solid liquid interface growth modes for low and high α values. (a) Continuous (normal) growth (b) Layer (lateral) growth
20	Figure 2.4[6] (a) A single-phase region of a phase diagram showing the liquids and the solidus lines. (b) Constitutional supercooling diagram for line 2.
21	Figure 2.5 The evolution of instabilities due to solute accumulation in a grain boundary groove[7].
26	Figure 2.6 The growth anisotropy in a faceted crystal. As the crystal grows, loosely packed {100} planes grow faster, while slowly growing closely packed {111} planes outlines the morphology of the crystal. t is time, and v_1 , v_2 are the growth vectors relative to the planes[7].
27	Figure 2.7 Growth of surface by movement of step related the atom attachment at kinks[7].
28	Figure 2.8 The presence of defect structure increases the mobility of a faceted plane by energetically favouring the deposition of atoms at the defect sites[7]. (a) Twin plane re-entrant edges (b) Screw dislocation
29	Figure 2.9 The effect of undercooling on the presence of surface defect (screw

- dislocation) on the growth mode of a smooth interface[7].
- 30 Figure 2.10 Growth of a cubic crystal in a pure melt at undercooling ΔT (or an alloy melt of uniform temperature) at constitutional undercooling ΔT [4].
- 31 Figure 2.11 The development of branching in faceted growth occurs when the rate of generation for new steps becomes higher than the rate at which steps propagate[7].
(a) Lateral growth is higher than the frequency of new layer formation, the crystal has an idiomorphic morphology;
(b) The formation of new layers predominately occurs close to the vertices, and the rate of advance of the steps is faster along the edges than towards the centre of faces, which gives rise to a hopper-like crystal morphology;
(c) the layer formation rate is faster than the propagation rate of the layers;
(d) eventually leads to branching of the crystal.
- 32 Figure 2.12 Schematic diagram of dendritic tip for growth of cubic materials in the $<100>$ direction[19].
(a) faceted
(b) nonfaceted
- 36 Figure 2.13 Surface tension balance at the three-phase ($\alpha/\beta/l$) junction, and the resulting curvature of the solid/liquid interface[21].
- 38 Figure 2.14 Growth of irregular eutectic[6].
(a) Schematic of branching of the faceted phase at λ_{br} , termination at λ_{min} , and the corresponding shape of the solid/liquid interface.
(b) Iron-carbon eutectic alloy directionally solidified at $R=0.0017\mu\text{m}/\text{s}$.
Branching was induced by a rapid increase in R . Longitudinal section. As polished.
- 47 Figure 2.15 Solute redistribution in cellular growth[4].
(a) Cellular growth and solute distribution in the growth direction
(b) An enlarged "volume element" and solute distribution transverse to the growth direction

- 48 Figure 2.16 Effect of solid diffusion during solidification on the composition distribution across dendrite arms calculated for $t_f/d^2 = 3.3 \times 10^8$ [4].
- 49 Figure 2.17 Weight percent nonequilibrium eutectic formed as a function of $\dot{\eta}$ for several Al-Cu alloys with less copper than the solubility limit (linear growth) [54].
- 49 Figure 2.18 Weight percent nonequilibrium eutectic formed as a function of $\dot{\eta}$ for several Al-Cu alloys with less copper than the solubility limit. (parabolic growth) [54]
- 50 Figure 2.19 Microsegregation in cellular solidification. At the top are shown two idealized volume elements, the one on the left for elongated (two-dimensional) cells and the one on the right for regular cells. Dotted lines show isoconcentrates at the values of f_s noted. The graph plots microsegregation for an Al-4.5Cu alloy [4].
- 57 Figure 2.20 Parameters for calculating inverse segregation [54].
- 58 Figure 2.21 Experimental values for chill-face segregation in Al(rich)-Cu system [54].
- 59 Figure 2.22 Maximum segregation in $\text{Al}_2\text{Cu}-\text{Al}$
- 66 Figure 2.23 Situation analyzed: flat, parallel isotherms at an angle to the vertical [66].
- 67 Figure 2.24 The effect of gravity on the velocity of inter-dendritic liquid in AL-4.5wt% Cu alloy [67].
- 67 Figure 2.25 The effect of gravity force on macrosegregation in AL-4.5wt% Cu alloy [67].
- 68 Figure 2.26 Thermal and concentration convection in the space between the dendrites urged by gravity (schematically) [76].
- 68 Figure 2.27 Situations of microconvection $v_{\Delta V_{\text{conv}}}$ urged by the jump of changing the volume during phase transition liquid-solid having different velocity of crystallization (schematically) [76].
- 79 Figure 3.1 Schematic of the apparatus used in series a experiment [54].

- 80 Figure 3.2 Crucible assembly in series A furnace[54].
- 81 Figure 3.3 Front and top view of the test equipment used in KC-135 flight[54].
- 82 Figure 3.4 Crucible assebly for KC-135 samples[54].
- 83 Figure 3.5 Typical mould and chill arrangement for unidirectional solidification(series B).
- 84 Figure 3.6 Cross section view of gradient QUESTS furnace[88].
- 85 Figure 3.7 Cross section of gradient assembly[88].
Gradient assembly specifications: sample housing size(0.635cm dia, 8.90cm length); # of furnace heating zones (3); furnace max. sample temp.(1000°C); furnace max. case temp.(180°C)
- 94 Figure 4.1 Cooling curves for series A samples.
(a) Al-38Cu
(b) Al-50Cu
- 95 Figure 4.2 Cooling curves for QUESTS samples.
(a) Al-38Cu on ground(↑)
(b) Al-35Cu on ground(↑)
- 96 Figure 4.2 continued
(c) Al-40Cu on ground(↔)
(d) Al-38Cu microgravity
- 98 Figure 4.3 Longitudinal cross section of ingots.
(a) AL-38Cu (series A ↑)
(b) Al-50Cu (series A ↑)
(c) Al-41Cu (series B ↑)
(d) Al-47Cu (series B ↑)
- 99 Figure 4.3 continued
(e) Al-38Cu QUESTS on ground(↑) sample(52X).
- 100 Figure 4.3 continued
(f) AL-35Cu QUESTS on ground(↑) sample(52X).
- 101 Figure 4.3 continued

- (g) Al-40Cu QUESTS on ground(↔) sample(52X).
- 102 Figure 4.3 continued
- (h) Al-38Cu QUESTS space sample(52X).
- 108 Figure 4.4 Microstructure of hypereutectic Al-Cu alloys at different compositions (Longitudinal sections 600X).
- (a) Al-35Cu(series A)
- (b) Al-38Cu(series A)
- 109 Figure 4.4 continued
- (c) AL-50Cu(series A)
- 110 Figure 4.5 Longitudinal pictures showing the dendritic growth morphology of the Al_2Cu primary phase along the solidification direction in an alloy of 35Cu(series A).
- (a) at the top
- (b) at the chill
- 111 Figure 4.6 Longitudinal pictures showing the rounded primaries and less developed primary dendrites at the chill becoming fully faceted at the top of Al-38Cu(series A).
- (a) at the top
- (b) at the chill
- 112 Figure 4.7 longitudinal pictures of Al-50Cu showing the faceted morphology of Al_2Cu phase in the beginning of solidification and elongated grain structures as solidification progressed further (series A).
- (a) at the top
- (b) at the chill
- 113 Figure 4.8 Longitudinal pictures showing Al_2Cu primary phase undergoing a transition from a dendritic to a faceted growth morphology along the length of the Al-38Cu (series B).
- (a) at the top
- (b) at the chill

- 114 Figure 4.9 Transverse sections at the centre of samples show faceted morphology of Al_2Cu phase in the air cooled sample and in the furnace cooled sample of Al-40Cu (series A).
 (a) air-cooled sample
 (b) furnace-cooled sample
- 115 Figure 4.10 Transverse sections of QUESTS samples(series C).
 (a) Al-37Cu on ground(\uparrow)
- 116 Figure 4.10 continued
 (b) Al-38Cu space sample
- 125 Figure 4.11 Macrosegregation of Al-42Cu series A sample.
- 126 Figure 4.12 Macrosegregation of Al-50Cu series A sample.
- 130 Figure 4.13 Macrosegregation of AL-38Cu series B sample.
- 135 Figure 4.14 Macrosegregation of QUESTS samples in scaled concentration.
 (a) Al-37Cu on ground(\uparrow) sample
 (b) Al-35Cu on ground vertical up sample
- 136 Figure 4.14 continued
 (c) Al-40Cu on ground(\leftrightarrow) sample
- 137 Figure 4.15 Comparison of macrosegregation between Al-38Cu ground-based and space samples.
- 139 Figure 4.16 Longitudinal sections of KC-135 samples.
 (a) Al-36Cu, 0G
 (b) Al-36Cu, 1.8G
- 140 Figure 4.16 continued
 (c) Al-47Cu, 0G
 (d) Al-45Cu, 1.8G
- 141 Figure 4.17 Microstructure of KC-135 samples.
 (a) Al-36Cu, 0G sample, sections at the top and the chill
- 142 Figure 4.17 continued
 (b) Al-36Cu, 1.8G sample, sections at the top and chill

- 143 Figure 4.17 continued
 (c) Al-47Cu, 0G sample, sections at the top and the chill(250X)
- 144 Figure 4.17 continued
 (d) Al-45Cu, 1.8G sample, sections at the top and the chill(250X)
- 147 Figure 4.18 Macrosegregation of Al-36Cu 0G, KC-135 sample
- 148 Figure 4.19 Macrosegregation of Al-47Cu 0G, KC-135 sample
- 149 Figure 4.20 Macrosegregation of Al-36Cu 1.8G, KC-135 sample
- 150 Figure 4.21 Macrosegregation of Al-45Cu 1.8G, KC-135 sample
- 155 Figure 4.22 The unit crystal structure of Al_2Cu intermetallic compound. A, B, and C indicate the Al, Cu and Al atomic layers, respectively.
- 161 Figure 4.23 Mechanisms by which shear flow may remove dendrite from the primary surface.
- 161 Figure 4.24 Model for calculating the torque at point A due to shear stress.

LIST OF TABLES

Page	
69	Table 2-1 The relationship between solidification mechanism and gravity.
74	Table 3-1 The composition of alloys used in present study.
92	Table 4-1 Cooling Characteristics of Series A Samples.
92	Table 4-2 Cooling Characteristics of Series B Samples [47].
93	Table 4-3 Cooling Characteristics of Series C Samples.
121	Table 4-4 (a) Primary Arm Spacings (λ_1) between θ phase.
122	Table 4-4 (b) Measurement of Spacings for QUESTS Samples.
124	Table 4-5 Macrosegregation of Al-42Cu and Al-50Cu (series A samples).
129	Table 4-6 Macrosegregation of Al-38Cu (series B sample).
133	Table 4-7(a) Macrosegregation of QUESTS Ground-based Samples
134	Table 4-7(b) Macrosegregation of Al-38Cu QUESTS samples.
146	Table 4-8 Macrosegregation of KC Samples.
151	Table 4-9 Primary arm spacings of KC-135 Al-36%Cu ingot.
154	Table 4-10 Attachment energy for a group of Al_2Cu atoms for various solid-liquid interface planes[7].

CHAPTER I

INTRODUCTION

Considerable progress has been made in recent years towards an understanding of the solidification of the metals. For an Al-Cu system, Cu is mainly added to increase the strength, at low temperature by heat treatment, and, at higher temperatures, through the formation of compounds. There has been appreciable interest in the Al-CuAl₂ eutectic as a composite material because a more or less perfect lamellar structure can be obtained. A typical phase diagram for this alloy is shown in Figure 1.1. The phase diagram essentially indicates the existence of various phases (in equilibrium) in the alloy at a certain temperature and composition. The pressure is assumed as 1 atmosphere. Hypo-eutectic Al-Cu alloys contain less than 33.2 per cent Cu and having a structure of α (Al phase) matrix with eutectic θ phase distributed in it. Hyper-eutectic Al-Cu alloys contain from 33.2 to 52.5 per cent Cu and have a structure of primary θ phase in a eutectic matrix.

Gravity driven convective flow can significantly influence the microstructure of metals and alloys of commercial interest. Microgravity environment in materials processing offers the advantages of eliminating buoyancy-driven convection and sedimentation. The low gravity environment of space offers an attractive opportunity for performing critical tests to determine the role of convection in alloy solidification. The NASA KC-135 aircraft has been utilized for performing solidification in microgravity. This plane is capable of flying multiple parabolic trajectories which

provide alternating low-g (20-30 seconds at 0.01g) and high-g (approximately 90 seconds of 1.5-2g) periods. However, the short duration of the low-g environment on the KC-135 restricts the experimentation. Reduced effective gravity for extended periods of time is achieved on the Space Shuttle flights. Directional solidification under microgravity has been used to study various basic phenomena and processing methods in a number of different systems. The macro- and micro-segregation during solidification as well as the role of gravity-driven phenomena such as convection and sedimentation on micro-structures have been studied in various alloys. However, theories of fluid motion are still inadequate to explain the observed results.

In the present study, a special three-zone gradient freeze QUESTS furnace was used to carry out microgravity experiment aboard the space shuttle. Unidirectional solidification of hypereutectic Al-Cu alloys was performed on the ground as well as in a microgravity environment. The microstructure and spacings of primary θ phase and inter θ -phase eutectic were measured. The macrosegregation phenomena were analyzed. An attempt is made to explain the difference between the ground-based sample and the space sample. Interpretation is achieved by analyzing the inter-dendritic liquid flow and comparing the viscous stress due to natural convection with the solid-liquid interface attachment energy. A mechanism based on shear-induced torque retarding attachment at the surface is proposed to explain the difference in microstructure between the ingots solidified in unit gravity and that solidified aboard a space shuttle in zero gravity.

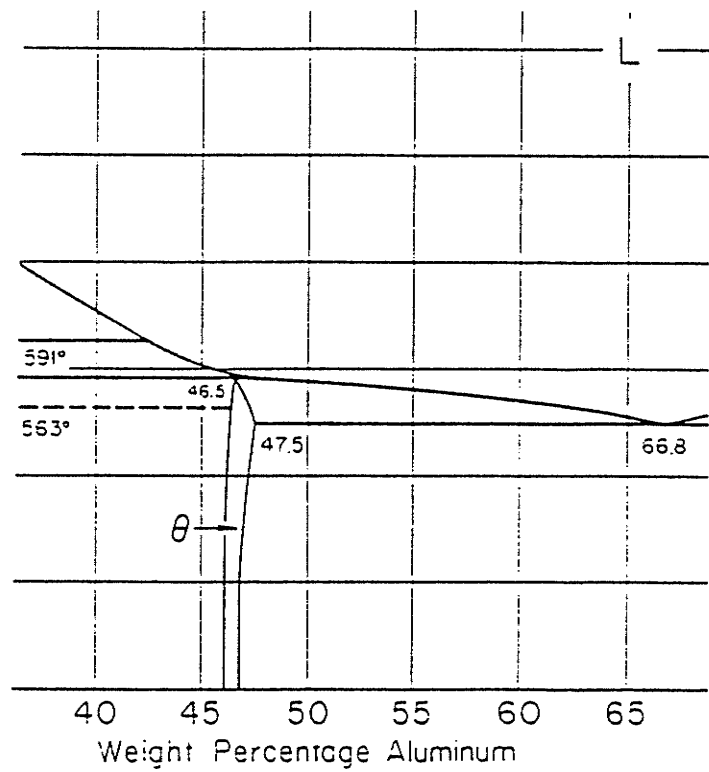
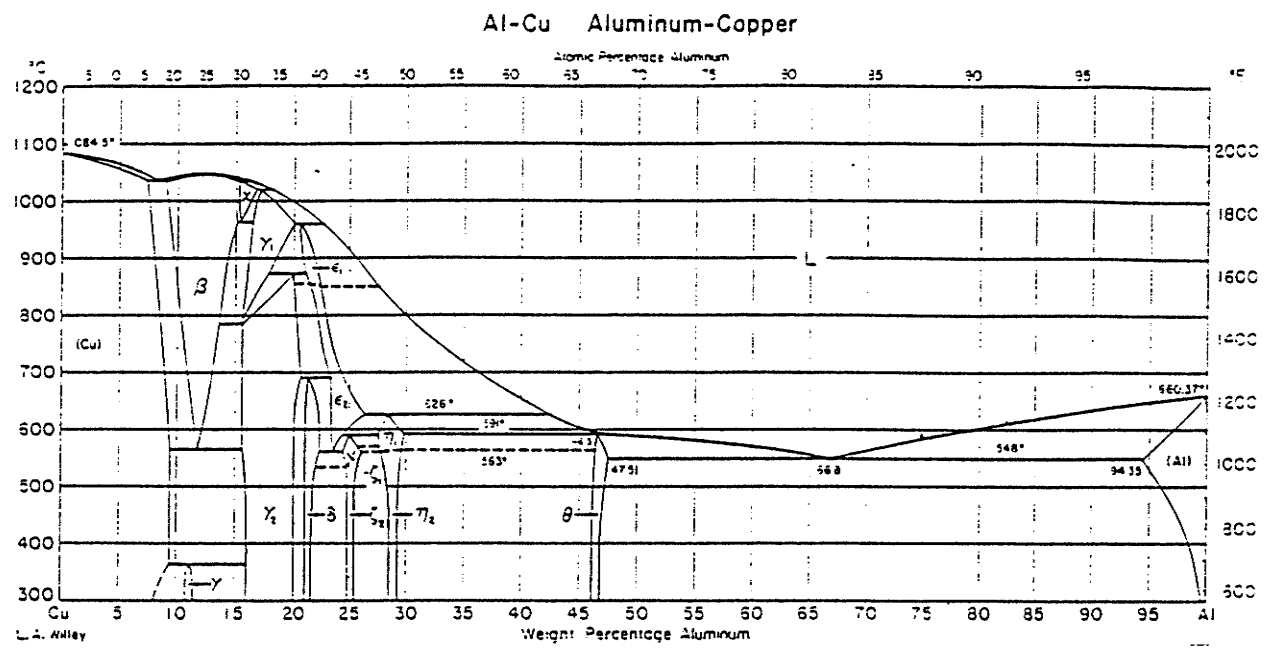


Figure 1.1 The Al-Cu phase diagram[6].

CHAPTER II

LITERATURE REVIEW

2-1 SOLIDIFICATION AND THERMODYNAMICS OF INTERFACES

2-1-1 BASIC CONCEPTS OF SOLIDIFICATION

Solidification is the transformation of molten liquid to a solid and, as in most phase transformations, involves nucleation and growth. The phenomenon of melting and freezing has been discussed in detail by Chalmers[1], particularly, to account for structures obtained in actual ingots. The fundamentals of solidification have been discussed extensively by Chalmers[2], Winegard[3], Flemings[4], Minkoff[5], Perepezko, Loesoult, Trivedi and Kurz[6]. Perepezko[6] showed that thermodynamically for solidification to occur, there is a departure from complete liquid-solid equilibrium. This departure brings the liquid into an undercooled state in which it is metastable because of the absence of one or more stable solid phases. The driving energy, ΔG , to initiate solidification is

$$\Delta G = (\Delta T \Delta H_f) / T_{mp} \quad (2.1)$$

where ΔT is the undercooling, ΔH_f is the enthalpy of fusion and T_{mp} is the equilibrium solidification temperature.

Solidification is a process that occurs by nucleation and growth. Gibbs[5]

analyzed the transformation of the liquid to a solid phase taking into account the change of free energy between phases and the free energy change created by the introduction of new surfaces. The free energy change for nucleation, therefore, can be represented by these two parts as:

$$\Delta G(r) = 4\pi r^2 \sigma + 4/3 \pi r^3 \Delta G_v \quad (2.2)$$

Here, σ is the surface free energy per unit area, ΔG_v is the free energy difference between a mole of the solid phase and a mole of the liquid phase, and $\Delta G(r)$ is the free energy change to form a cluster of size r . The activation barrier for nucleation, ΔG_{cr} , is reached at a critical size r_{cr} , given by:

$$r_{cr} = - (2\sigma/\Delta G_v) = - (2\sigma T_{mp}/\Delta H_f \Delta T) \quad (2.3)$$

and

$$\begin{aligned} \Delta G_{cr} &= (16\pi\sigma^3/3\Delta G_v^2) = (16\pi\sigma^3 T_{mp}^2) / (3\Delta G_v^2) \\ &= (16\pi\sigma^3 T_{mp}^2) / (3\Delta H_f^2 \Delta T^2) \end{aligned} \quad (2.4)$$

At increased values of undercooling, ΔT , r_{cr} is reduced ($r_{cr} \propto \Delta T^{-1}$) and G_{cr} is reduced more rapidly ($\Delta G_{cr} \propto \Delta T^2$). If solid nucleation is regarded as the growth of clusters past the critical size, the nucleation rate, I , can be represented by[6] :

$$I = V_{sl} S_{cr} C_{(nr)} = (D_l/a^2) (4\pi r_{cr}^2/a^2) C_l \exp(-\Delta G_{cr}/KT) \quad (2.5)$$

where V_{sl} is the jump frequency associated with atom jumps from the liquid to join the cluster and can be estimated from the liquid diffusivity, D_l , and jump distance, a , by D_l/a^2 . S_{cr} is the number of atoms surrounding a cluster, given approximately by $4\pi r_{cr}^2/a^2$. $C_{(nr)}$ is the concentration of critical clusters. Equation (2.5) indicates that the maximum nucleation rate occurs at $T=T_{mp}=(1/3)T_f$.

Homogeneous nucleation is the most difficult kinetic path to crystal formation because of the relatively large activation barrier for nucleus development. The energetics of heterogeneous nucleation(nucleation on a substrate) can be described by a modification of equation (2.2) to account for the different interfaces and the modified cluster volume involved in nucleus formation. The free energy change for heterogeneous nucleation is described in equation (2.6).

$$\Delta G(r)_{het} = \Delta G_{cr}(hom)[f(\theta)] \quad (2.6)$$

Here θ is the contact angle between the nucleus and the heterogeneous nucleation site.

After nucleation, the solid phase grows by mechanisms involving control by either thermal or mass diffusion, or by interface control. Metallic alloys generally grow by diffusion controlled mechanisms while non-metallic phases generally grow by mechanisms controlled by the interface structure.

Lesoult[6] described solidification as a succession of atomic events occurring in

series. The kinetic undercooling, ΔT_k , in the case of pure substances is:

$$\Delta T_k = T_{fk} - T^* = (a/D_L) (R T_f/\Delta S_f) V \quad (2.7)$$

where T_{fk} is the equilibrium temperature at the interface defined by $\Delta T_k = T_f - T_{fk} = \Gamma$ K, where K is the interface curvature and Γ is the Gibbs-Thomson coefficient. The T^* is the actual temperature of the moving interface, D_L is the liquid diffusivity, a is the atomic distance between the crystallographic planes parallel to the interface, and V is the velocity of the interface.

For a given driving force, the growth velocity of the interfaces parallel to atomically dense planes is smaller than any other growth velocity. For an fcc crystal, for example, the dense {111} planes will tend to spread laterally more or less rapidly and form pyramids that have fourfold symmetry axes, that is $\langle 100 \rangle$ axes. Therefore the well-known fact that dendrites of cubic metals exhibit $\langle 100 \rangle$ axes and branches is probably related to their slight growth anisotropies.

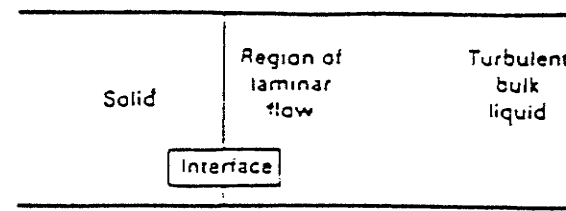
Solidification typically involves heat and mass transport phenomena on the microscopic and macroscopic levels. In the case of plane front solidification, the composition and temperature profiles at the interface are presented in Figure 2.1 (b) and 2.1 (c).

A departure from interface equilibrium during growth results not only in kinetic undercooling but also a dependence of the partition coefficient, k_v , on the velocity. The following functional form has been proposed to describe the effect of the velocity

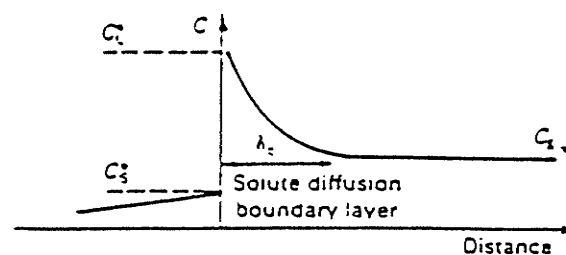
on k_v .

$$k_v = C_s^*/C_L = \{ k + (a_0/D_L)V\} / \{ 1 + (a_0/D_L)V\} \quad (2.8)$$

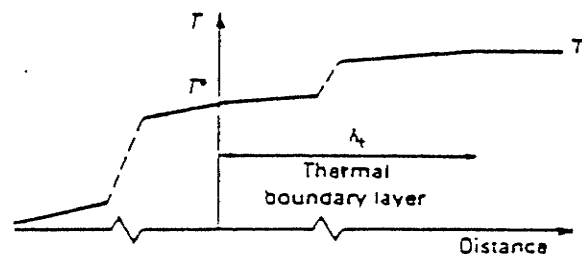
Here k is the equilibrium partition coefficient (assumed to be < 1) and a_0 is a length scale related to the interatomic distance with an estimated value of 0.5 to 5.0 nm (5 to 50 \AA^0).



(a)



(b)



(c)

Figure 2.1

The composition and temperature profiles for plane front solidification[6].

- (a) Constrained growth during plane front solidification
- (b) Schematic profiles of solute concentration
- (c) Temperature profile

2-1-2 THERMODYNAMICS OF THE INTERFACES

The equilibrium thermodynamic properties of interfaces were characterized first by Gibbs, who used a hypothetical dividing surface to separate the surface properties from those of bulk phases. This work has been reviewed by Apayadin and Smith[7]. The excess surface energy, E , for a multicomponent system is defined as:

$$E^i = TS^i + \sum \mu_x N_x^i + \sigma A \quad (2.9)$$

where S^i is the entropy of the interface, μ_x is the chemical potential of the component x , σ is the interface energy, N_x^i is the number of moles of x in i phase and A is the interface area.

By analyzing the relationship between the change in surface tension to the surface excess of the components, Gibbs described the interface energy change $d\sigma$, by the Gibbs absorption equation.

$$d\sigma = -S^i dT - \sum \Gamma_x d\mu_x \quad (2.10)$$

where Γ_x is the specific surface excess number of moles of component x .

In the case of constant temperature, equation (2.10) reduces to the Gibbs absorption isotherm:

$$\Gamma_x = -(\delta\sigma/\delta\mu_x)_{Ta} \quad (2.11)$$

where the subscripts T and a indicate constant temperature and a single phase, a, respectively.

In a binary system, absorption can be expressed as

$$\Gamma_{xz} = \Gamma_x - \Gamma_z \{ (C_x^a - C_x^b) / (C_z^a - C_z^b) \} \quad (2.12)$$

where the C_s are concentration of components X and Z in phases a and b, and Γ_{xz} is the relative absorption which becomes zero if the components x and z are present at the interface in the same ratio as in the bulk solution. This argument leads to the conclusion that the surface becomes relatively enriched in x for a positive absorption, $\Gamma_{xz}>0$, and depleted for a negative adsorption, $\Gamma_{xz}<0$.

Jackson[5] analyzed the distinction between two classes of materials which have smooth or rough interfaces in growth by examining the surface free energy changes on adding atoms to an atomically smooth surface. For a liquid-solid transformation, the change of surface free energy is:

$$\Delta F = - \Delta F_s - \Delta E_0 - \Delta E_l + T \Delta S_0 - T \Delta S_l - P \Delta V \quad (2.13)$$

Here, $P \Delta V$, the volume change for the transformation liquid to solid is taken to be approximately zero. ΔE_0 is the energy gained by transferring N_A atoms to the surface and ΔE_l is the average energy gained by the N_A atoms due to the presence of the other atoms on the surface. ΔS_0 is the entropy difference between solid and liquid phases,

while ΔS_1 is the entropy difference due to the possible randomness of the atoms on the surface. They are given by:

$$\Delta E_0 = 2L_0 (\eta/v) N_A \quad (2.14)$$

$$\Delta E_1 = L_0 (\eta_l/v) (N_A/N) N_A \quad (2.15)$$

and

$$\Delta S_0 = (L/T_E) N_A \quad (2.16)$$

where L_0 is the change of internal energy for the atom between the liquid and the solid state, η is the number of nearest neighbours, and v is the total possible number of nearest neighbours. N_A is the number of atoms on the surface and η_l is the number of nearest neighbours of a single atom on the plane surface, (N_A/N) is the fraction of occupied sites on the interface, and L is the latent heat of fusion.

Considering nearest neighbour interaction, and assuming a random distribution of atoms in the interface layer, the excess free energy, ΔF , may be expressed as a function of an atom concentration and a roughness parameter, α , by:

$$\begin{aligned} \Delta F/NkT = \alpha N_A & \left\{ (1 - N_A/N)^2 \right\} - \ln \left\{ N/(N-N_A) \right\} \\ & - (N_A/N) \ln \left\{ (N - N_A)/N_A \right\} \end{aligned} \quad (2.17)$$

where α is given by: $(L_0/KT_{mp})(\eta_l/v)$. The relationship is illustrated in Figure (2.2) for

different α . The decrease in free energy of an initially flat, solid-liquid interface is represented by the curves lying below the zero reference line. In this case, the deposition of liquid atoms on the interface takes place in a random manner, leading to surface roughening. (See Figure 2.3 (a).) This behaviour is called contiguous or normal growth. The curves above the reference line, on the other hand, correspond to an increase in free energy, where surface roughening is not thermodynamically stable. In this case, the interface motion is restricted to growth by layer extension in which deposition of the liquid atoms occurs selectively either at kinks or steps. The deposition leads to a flat interface during the growth, as represented in Figure 2.3 (b).

The solid /liquid interface is a region between two condensed phases in which interatomic cohesive energies are comparable. Physicists have successfully correlated the sharpness of the interface of pure substances to a faceting factor, F , which is defined as[6]:

$$F = \{Z^*/(1-Z^*)\} \{(A_m \sigma)/(R T_{mp})\} \quad (2.18)$$

The Z^* is the ratio between the number of near-neighbour atoms in the plane of the interface and the total number of near-neighbour atoms in the bulk ($Z^* = 0.5$ for planes of fcc crystals). Furthermore, A_m is the area occupied by 1 mole of atoms at the interface, σ is the solid/liquid interfacial tension, and T_{mp} is the melting temperature. Pure metals are expected to grow from their own melts with a diffuse interface as opposed to a sharp interface, because their faceting factors are approximately equal to

the critical value of 2.

The solid/liquid interfacial tension causes a change in equilibrium melting point, often called Gibbs-Thomson undercooling. For pure substances, this curvature undercooling ΔT_K is given by Equation (2.7). For most metals, Γ is of the order of 10^{-7} K.m. Therefore, the curvature undercooling might often appear negligible. Some nonmetallic eutectic phases, such as graphite or silicon in foundry alloys, exhibit strong anisotropies of interfacial tension in contact with the molten alloy.

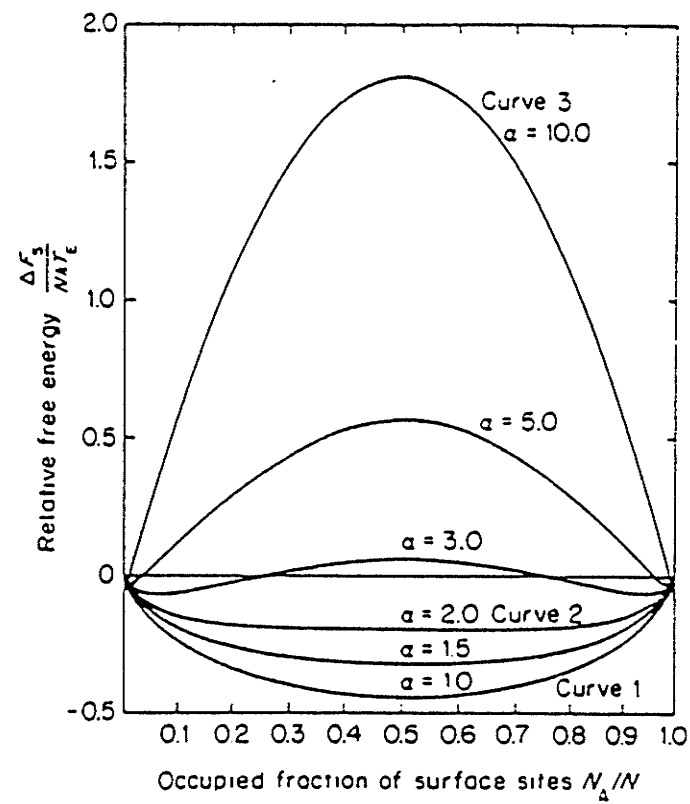
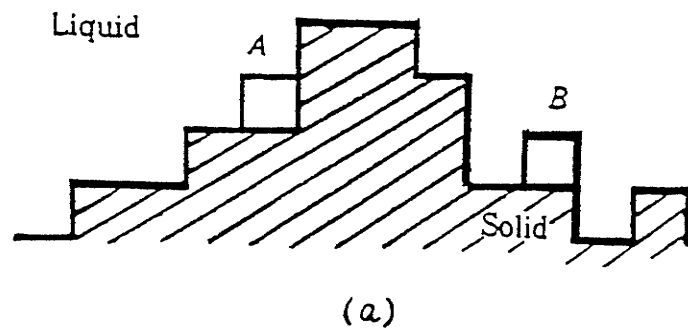
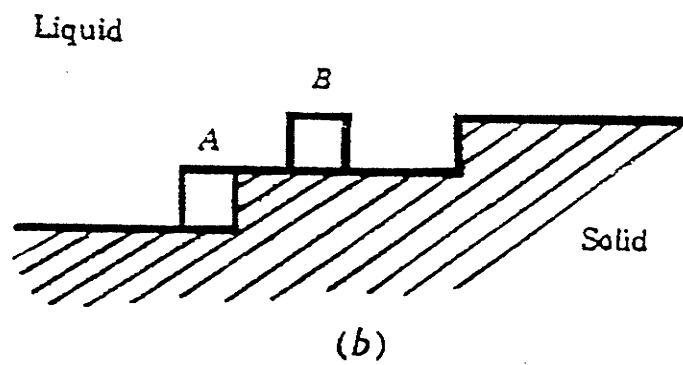


Figure 2.2

Curves of relative surface free energy as a function of occupied fraction of surface sites, related to the quantity α [5].



(a)



(b)

Figure 2.3

The solid liquid interface growth modes for low and high α values.

(a) Continuous (normal) growth

(b) Layer (lateral) growth

In (a), all available sites on the solid have the same energetic barrier for atoms A and B (liquid atoms) to become solid atoms.

In (b), the kink site at atom A has a lower energy barrier than the site occupied by B.

This favours growth by the lateral motion of steps[7].

2-2 PRIMARY PHASE SOLIDIFICATION

2-2-1 DENDRITIC GROWTH

Alloy solidification microstructures are controlled by two important factors, the composition of the alloy and the heat flow conditions in the mould. When an alloy of uniform liquid composition, C_0 , is cooled, the first solid that forms at temperature, T_i , will have a composition, kC_0 , which is lower than the liquid composition, C_0 (It is assumed $k < 1$). Thus, the excess solute rejected by the solid will give rise to a solute-rich layer in front of a growing interface, in which the liquid composition is a maximum C_0/k at the interface and decreases with increasing distance from the interface. This liquid composition profile gives rise to a variation in the liquids temperature with distance as illustrated in Figure (2.4)[6]. The stability of the solid-liquid interface can be disturbed by the growth conditions prevailing at the interface. Tiller et al[7] introduced the concept of constitutional supercooling to explain the breakdown of a planar interface into cellular and/or dendritic in terms of growth rate, R , and temperature gradient in the liquid at the solid-liquid interface, G_l . For a stable planar interface,

$$G_l \leq m_l C_0 \left\{ (k-1)/k \right\} (R/D_l) \quad (2.19)$$

where m_l is the slope of the liquids, C_0 is the alloy composition, k is the partition coefficient, and D_l is the diffusion coefficient of the solute in the liquid.

Instability occurs when the actual temperature profile in the liquid, in front of

the interface, is lower than the liquids temperature profile as seen in Figure 2.4 (b).

In this case, as supercooling increases with increasing distance from the interface, any perturbation developing on the interface is favoured to protrude into the melt, causing the interface to break down into cells and eventually dendrites. Figure (2.5) shows the evolution of instabilities at a grain boundary groove. Glickaman, Schaefer and Ayers[8] summarized a multiplicity of theories to describe dendritic growth. Among the theories, only three are in a form well suited to experimental testing. They are:

- (1) Trivedi's theory, which is an advanced form of Temkin's original model;
- (2) a "modified" version of Ivantsov's original model;
- (3) Nash and Glicksman's self-consistent model, in which the dendritic shape is derived as part of the solution and not related to an input parameter which merely constrains the solution.

Each of the three theories of steady-state dendritic growth yields a velocity (v) -supercooling (ΔT) relationship which, over a reasonably extensive range of supercooling, may be expressed as a power law: $v = \beta G \Delta\theta^n$. Here β and n are numerical constants specific to each theory. G is the lumped material parameter described as: $\alpha \Delta S_f L / C_p \gamma_{sl}$, where α and C_p are the thermal diffusivity and specific heat of the liquid phase, respectively. ΔS_f and L are the entropy and enthalpy for fusion, and γ_{sl} is the solid-liquid interfacial energy. $\Delta\theta$ is the normalized supercooling given by $\Delta T C_p / L$. Furthermore, the tip radius of curvature, tip temperature, and tip concentrations are predicted as functions of the growth rate and temperature gradient. An approximate model of dendritic interface growth, under controlled solidification

conditions was given by Bower et al.[9]. The tip temperature of cells and dendrites under unidirectional solidification was measured by Burden and Hunt [10]. By analyzing Zener's ideas[12] for diffusion at the tip, a theory for dendritic growth was developed[11]. A formulation was also developed by Trivedi[13] by introducing a constitutional supercooling parameter and assuming that the tendency for perturbation to grow is directly proportional to the parameter if there is any perturbation in the dendrite shape. Another approach was proposed by Kurz and Fisher[14], where the radius for curvature of a dendrite tip was assumed to be proportional to the wavelength of perturbation in a planar interface. Miyata and Suzuki[15] developed a consistent theory of dendritic growth which takes into account the heat flow and the solute around the dendritic front. The experimental studies have been carried out on aluminum-copper alloy to obtain data on cellular and dendritic growth[16,17].

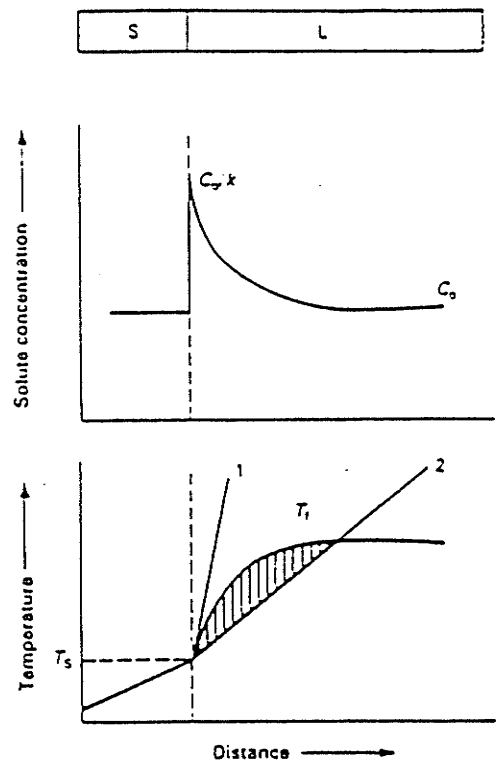
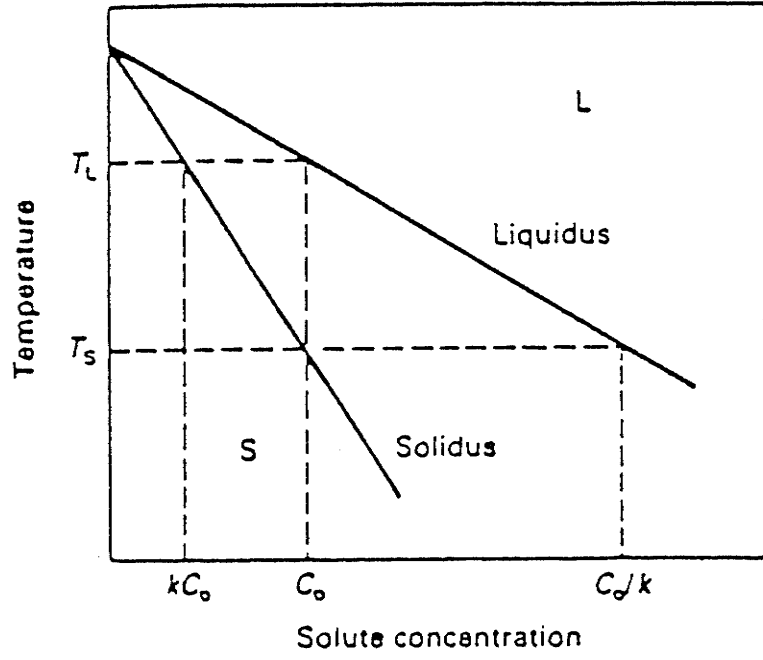


Figure 2.4[6]

- (a) A single-phase region of a phase diagram showing the liquids and the solidus lines.
- (b) Constitutional supercooling diagram for the temperature gradient 2.

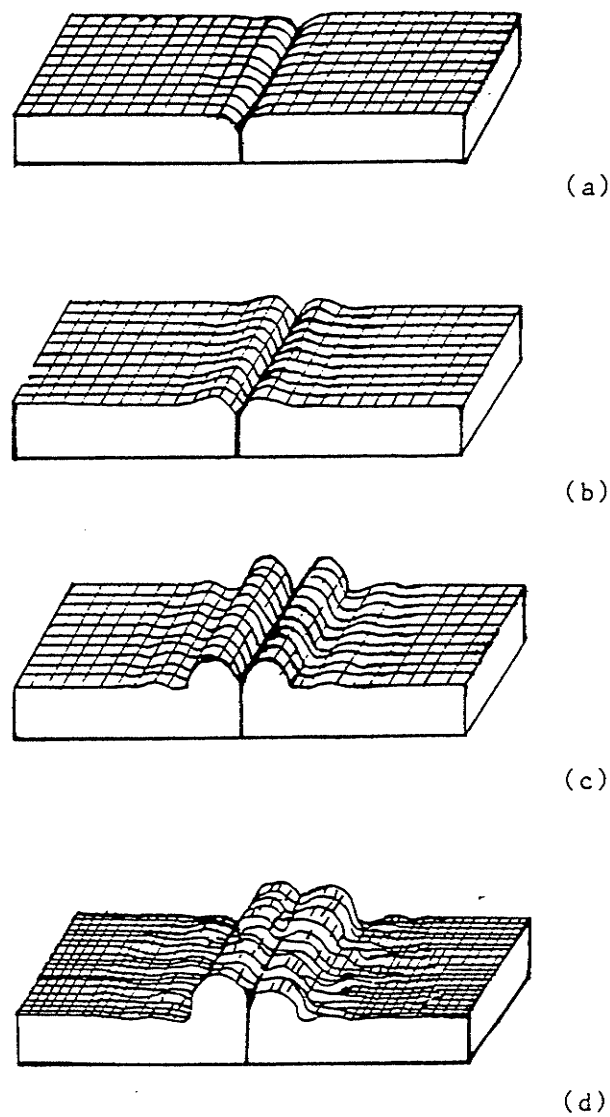


Figure 2.5

The evolution of instabilities due to solute accumulation in a grain boundary groove[7].

2-2-2 FACETED GROWTH

Minkoff[5] indicated that metallic crystals or crystals having low entropy of fusion have rough interfaces and that the rate of growth of the faces is controlled by the diffusion flux. On the other hand, crystals with $\Delta S(\text{fusion}) > 2R$ (or $\alpha > 2$) grow with a faceted interface. In this case, the energies of such sharp and smooth interfaces are orientation dependent. The parameter controlling growth is the rate at which the interface accepts atoms. Therefore, growth may be controlled by the nature of steps on such surfaces, the natural defects ending on step surfaces, or by nucleation of new faces on facets.

The theory for a perfect crystal is concerned with the continuation of growth by two-dimensional nucleation on the low-index (smooth) surfaces. This theory is related to the structure of monomolecular steps on the surfaces. Such surfaces move by atom attachment to kinks(Figure 2.7). Burton et al.[18] showed that steps would not be created by thermodynamic fluctuations. Hence at low supersaturation, growth must be related to imperfections. These defects might have a component normal to the crystal surface, such as screw dislocations or twin plane re-entrant edges (TPRES) because these edges provide low energy sites for the start of a new layer (See Figure (2.8)). Undercooling associated with the movement of an interface may also affect the lateral growth behaviour by favouring the random deposition of liquid atoms onto the solid-liquid interface. The effect of undercooling on the transition from a smooth to a rough interface can be seen in Figure(2.9).

The growth rate of the faceted interface due to step nucleation can be

calculated[7] by assuming that the rate of growth for the step is sufficiently high so that each step nucleated on a surface spreads to form one molecular plane before the formation of a second nucleus on the same surface. If the transformation temperature is close to T_{mp} , the growth rate of the faceted interface $G = A_1 \exp(A_2 \Delta T)$, where changes in terms A_1 and A_2 with undercooling, ΔT , are small.

In the case of faceting crystal growth from its own melt, the liquid is undercooled ΔT degrees below its melting point. The crystal grows by dissipation of heat into the melt[4]. The temperature distributions outward from the centre of a flat face and on the same face near the edge are illustrated in Figures 2.10 (a) and (b), respectively. In these figures, the interface is at temperature T_i , and is undercooled by an amount ΔT_k below the equilibrium melting point. The difference between the centre and the edge of the face is that heat diffuses more readily at the corner because of the corner effect (divergence of heat flux). Hence the kinetic undercooling, ΔT_k , must be larger than that at the centre of a face. The growth rate of the face, which results from the kinetic undercooling, is maximum near the corners. Steps originate near the corners and spread across the face, decreasing as the local undercooling ΔT_k decreases.

For the case of a faceted crystal growing in an alloy melt, the diffusivity of heat is much greater than the diffusivity of solute. Consequently, only the latter is generally considered. The growth morphology is affected by the transport rate of atoms from the solution to the crystal surface. In this case, the mobility of the interface is reduced due to the depleted atom concentration. Furthermore, the concentration of atoms at the corners is higher than at the centre of the face, so that

the driving force to form a new layer is higher at the corners of the crystal. Steps nucleate in these areas and propagate across the interface at a decreasing rate, v , determined by the undercooling available for atomic attachment. This leads to a closer spacing, d , between the steps on the interface towards the centre of the facet.

Eventually, branches develop at the corners of the crystal as seen in Figure(2.11)[7].

Keith and Padden[19] proposed the following relation for the stability of a growing faceted crystal:

$$Rr/D_l \leq -\{\Delta T/m_l C_0(1-k)\} \quad (2-20)$$

Where r is the approximate radius of the faceted crystal and m_l is the solut content in liquid. The directions assumed by the growing dendrite arms in faceted materials are always ones that are "capped" by relatively slow-growing (usually low-index) planes. The effect of these slowly growing planes in the shape of the crystal is seen in Figure (2.6) and Figure (2.12) gives a schematic of a dendrite growing in the $\langle 100 \rangle$ direction with its tip capped by four slow-growing $\{111\}$ planes. The slowly growing planes would be expected to be the closest-packed planes. The major dendrite direction is generally the axis of a pyramid whose sides are the most closely packed planes from which a pyramid can be formed. Normally, the $\langle 100 \rangle$ direction is the major dendrite direction for the body- and face-centred cubic structures.

Apayadin and Smith[7] investigated the growth direction of Al_2Cu primary crystals. A TEM diffraction pattern was obtained in the $[001]$ direction. The Laue back

reflection pattern from a transverse section showed that the preferential growth direction of the primaries was along a [001] axis. It was also demonstrated, by seeding an Al-Cu alloy with a single crystal of Al_2Cu having a predetermined orientation, that the growth direction for the primary Al_2Cu did not occur in the heat extraction direction. Rather, growth happened in [001] or [100] orientations, depending on which of these orientations was closer to the orientation of the seed crystal. These results show the anisotropic growth behaviour of the Al_2Cu compound crystal .

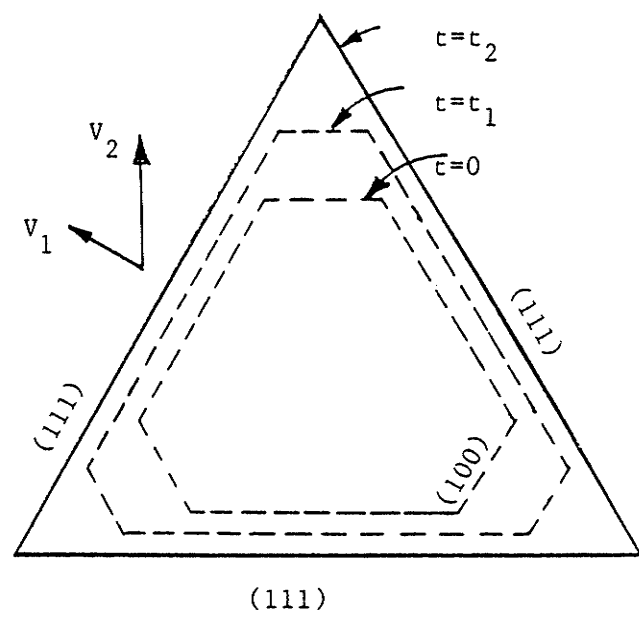


Figure 2.6

The growth anisotropy in a faceted crystal. As the crystal grows, loosely packed {100} planes grow faster, while slowly growing closely packed {111} planes outlines the morphology of the crystal. t is time, and v_1 , v_2 are the growth vectors relative to the planes[7].

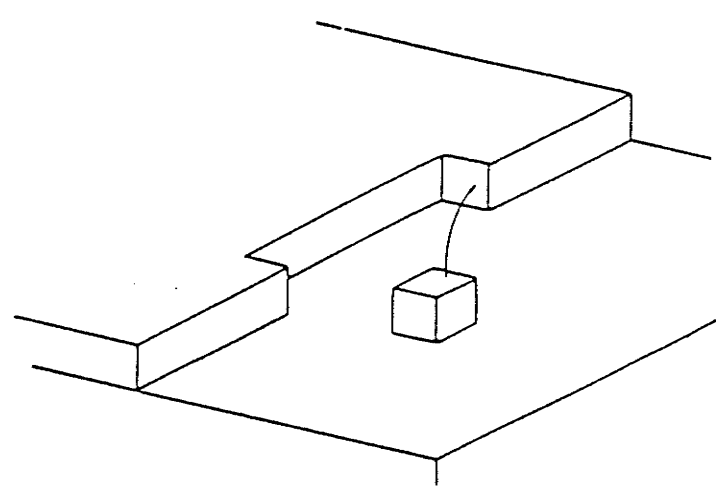


Figure 2.7

Growth of surface by movement of steps related to atom attachment at kinks[7].

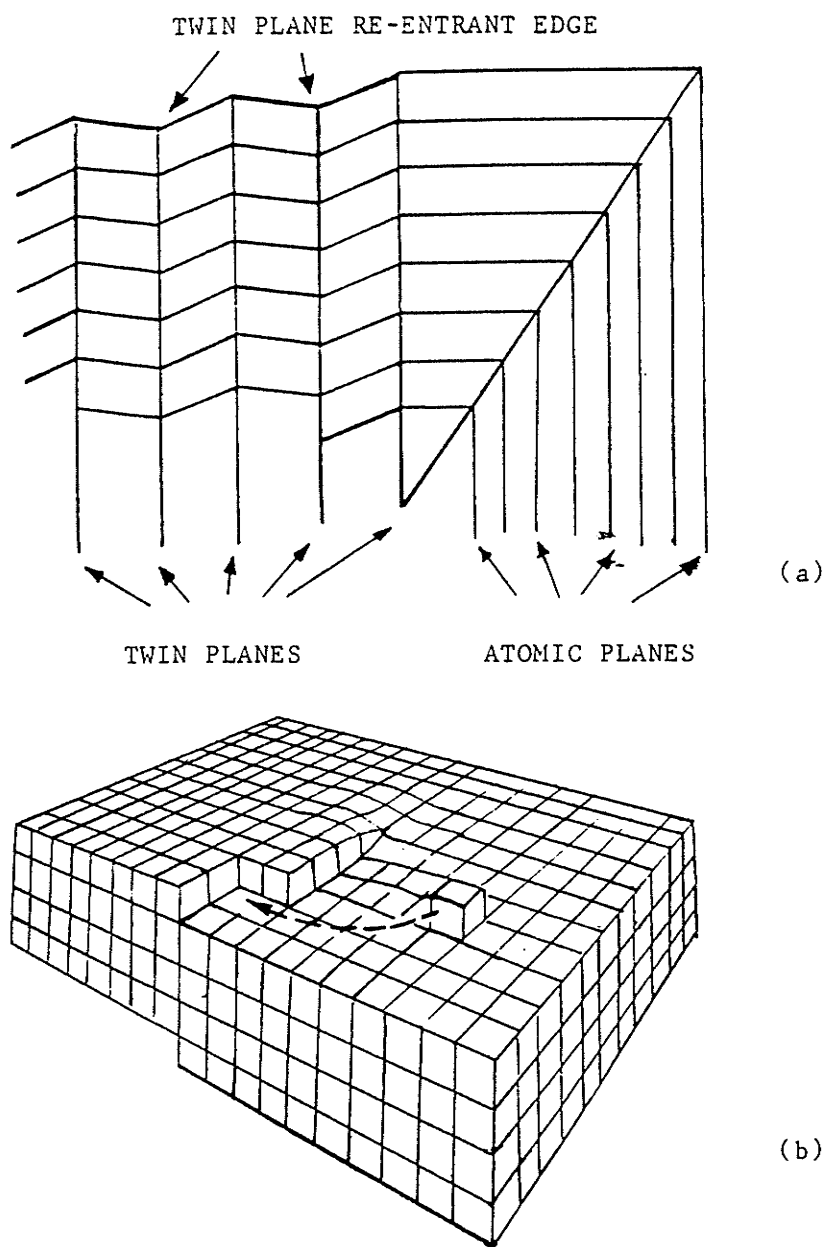


Figure 2.8

The presence of defect structure increases the mobility of a faceted plane by energetically favouring the deposition of atoms at the defect sites[7].

- (a) Twin plane re-entrant edges
- (b) Screw dislocation

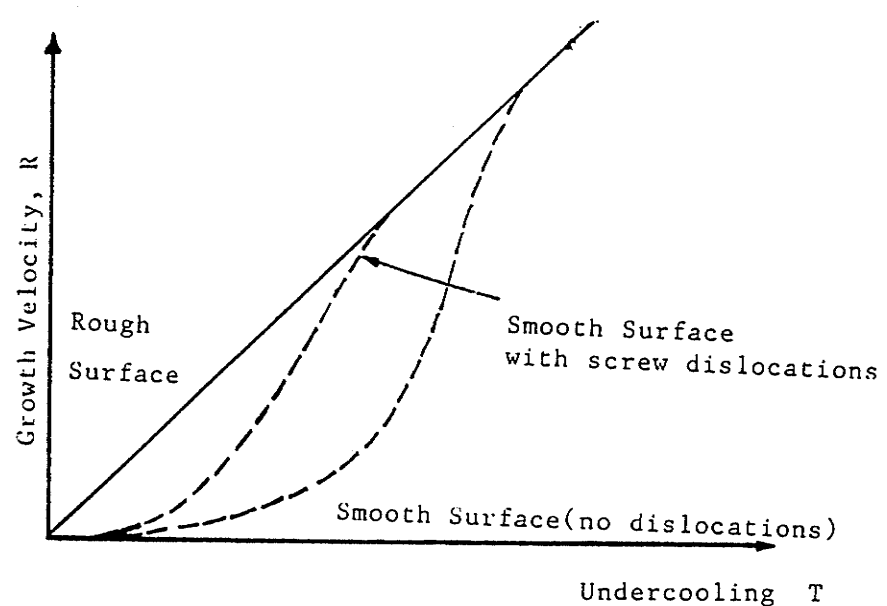


Figure 2.9

The effect of undercooling on the presence of surface defect (screw dislocation) on the growth mode of a smooth interface[7].

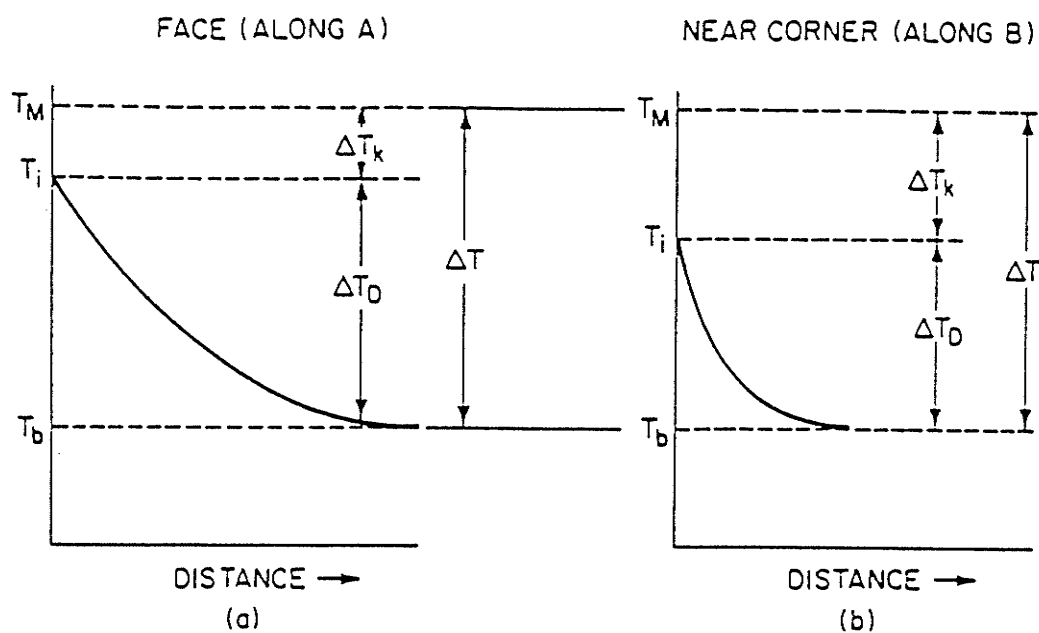
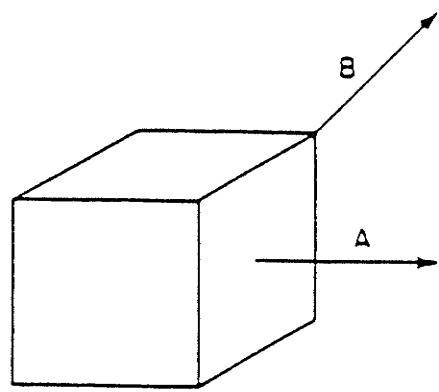


Figure 2.10

Growth of a cubic crystal in a pure melt a undercooling ΔT (or an alloy melt of uniform temperature) at constitutional undercooling $\Delta T[4]$.

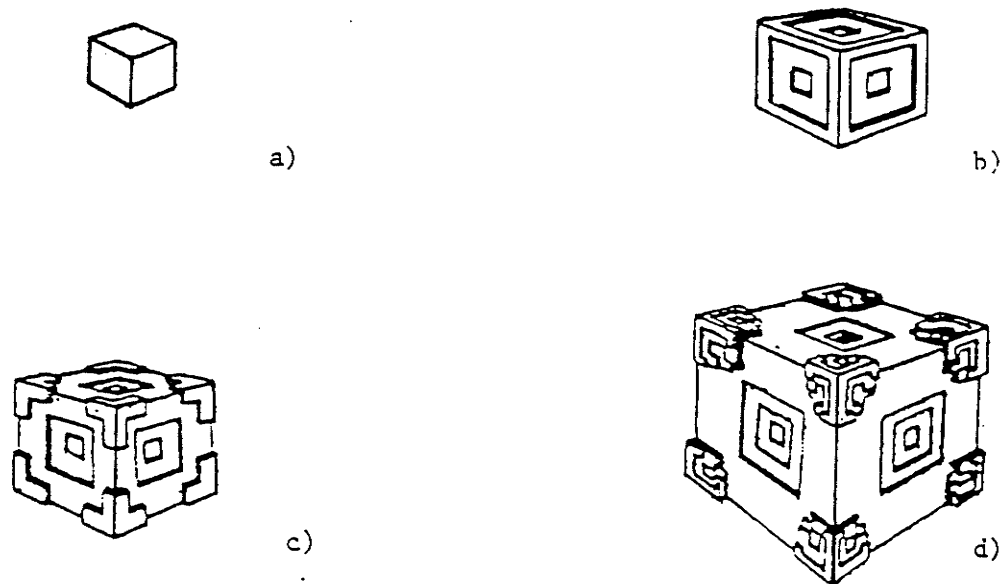
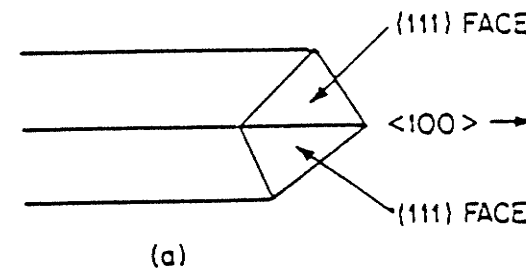


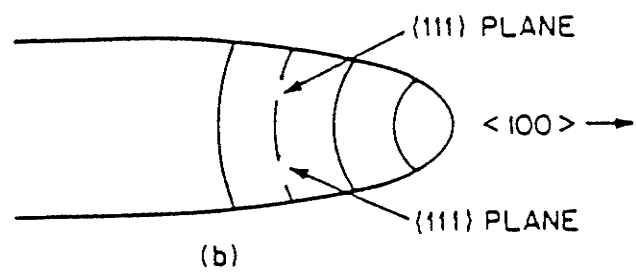
Figure 2.11

The development of branching in faceted growth occurs when the rate of generation for new steps becomes higher than the rate at which steps propagate[7].

- (a) Lateral growth is higher than the frequency of new layer formation, the crystal has an idiomorphic morphology;
- (b) The formation of new layers predominately occurs close to the vertices, and the rate of advance of the steps is faster along the edges than towards the centre of faces, which gives rise to a hopper-like crystal morphology;
- (c) the layer formation rate is faster than the propagation rate of the layers;
- (d) eventually leads to branching of the crystal.



(a)



(b)

Figure 2.12

Schematic diagram of dendritic tip for growth of cubic materials in the $<100>$ direction[19].

(a) faceted

(b) nonfaceted

2-3 EUTECTIC SOLIDIFICATION

2-3-1 REGULAR EUTECTIC GROWTH

Eutectic structures are characterized by the simultaneous growth of two phases from a liquid. If both phases are nonfaceted, usually when both are metallic, the eutectic will exhibit a regular morphology. The microstructure is then composed of lamellae or fibres having a high degree of regularity and periodicity. Chadwick[20] has shown, for example, that in the aluminum copper eutectic the same lamellar structure can persist for several centimetres. On the other hand, Craft[21] has demonstrated that a preferred relationship develops during the growth of a eutectic "single crystal". The relationship is expressed as:

$$(111) \text{ Al} // (211) \text{ CuAl}_2$$

$$[101] \text{ Al} // (120) \text{ CuAl}_2$$

$$(111) \text{ Al} // \text{lamellar interface}$$

During eutectic solidification, the growing α phase rejects B atoms into the liquid because of their lower solubility with respect to the liquid's concentration. Conversely, the β phase rejects A atoms, so that the α and β phases grow side by side in a cooperative manner. The B atoms rejected by the α phase are needed for the growth of the β phase, and conversely. On the other hand, the solute build up in the liquid ahead of the growing solid/liquid interface is lowered considerably by the sideways diffusion. Thus, the growth is thermodynamically favourable. The smaller the lamellar spacing, λ , the smaller the solute build up. On the other hand, the surface tensions at the three-phase junction $\alpha/\beta/l$ must be balanced to ensure mechanical

equilibrium. (see Figure 2.13). This constraint imposes fixed contact angles, leading to a curvature of the solid/liquid interface.

Jackson and Hunt[22] were the first to analyze the problem in detail. They solved the steady-state diffusion equation by using a moving coordinate system and obtained the following equation for an isothermal interface.

$$\Delta T/m = R\lambda K_1 + K_2/\lambda \quad (2-21)$$

Here, ΔT is the total undercooling at the interface, R is the growth rate, λ is the width of the $\alpha+\beta$ lamellae, whereas m, K_1 and K_2 are the system parameters. For dendrite growth, where

$$d\Delta T/d\lambda = 0 \quad (2-22)$$

Equation (2-21) becomes:

$$\lambda^2 R = \Delta T^2 / R = \text{constant} \quad (2-23)$$

The lamellar spacing λ and the growth undercooling, ΔT , are given by[6]:

$$\lambda = (\Phi K_1) / \sqrt{R} \quad (2-24)$$

and

$$\Delta T = (\Phi + 1/\Phi) / 2K_2\sqrt{R} \quad (2-25)$$

Where R is the solidification rate. The K_1 and K_2 are constants related to the material properties and Φ is a regularity constant whose value is close to unity for a regular eutectic. The scale of the eutectic microstructure depends upon the solidification rate. An important characteristic of regular eutectic growth is that the lamellae are parallel to the heat flow direction during solidification and perpendicular to the solid/liquid interface.

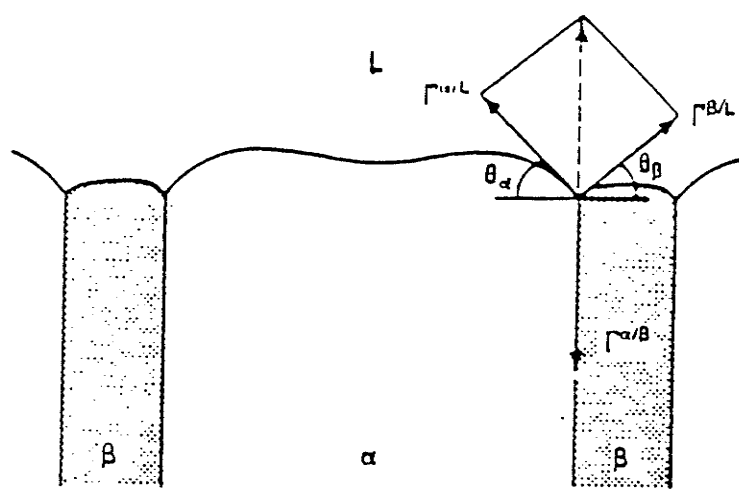


Figure 2.13

Surface tension balance at the three-phase ($\alpha/\beta/\ell$) junction, and the resulting curvature of the solid/liquid interface[21].

2-3-2 IRREGULAR EUTECTIC GROWTH

Irregular eutectics, such as Al-Si and Fe-C, exhibit a variation in the spacing between the phases because the growth direction of the faceted phase is determined by specific atomic orientations. Unlike regular eutectic, the growth direction is not necessarily parallel to the heat flux. This results in a larger average spacing which is accompanied by greater interfacial undercooling. Therefore, the solid/liquid interface is non-isothermal, i.e., its shape is irregular (Fig. 2.14). Sato and Sayama[23] confirmed this hypothesis experimentally, using a faceted organic eutectic.

For irregular eutectic growth, a mean spacing(x) and a mean undercooling(ΔT) can still be defined by Equation (2-24) and (2-25). In this case, Φ is greater than unity.

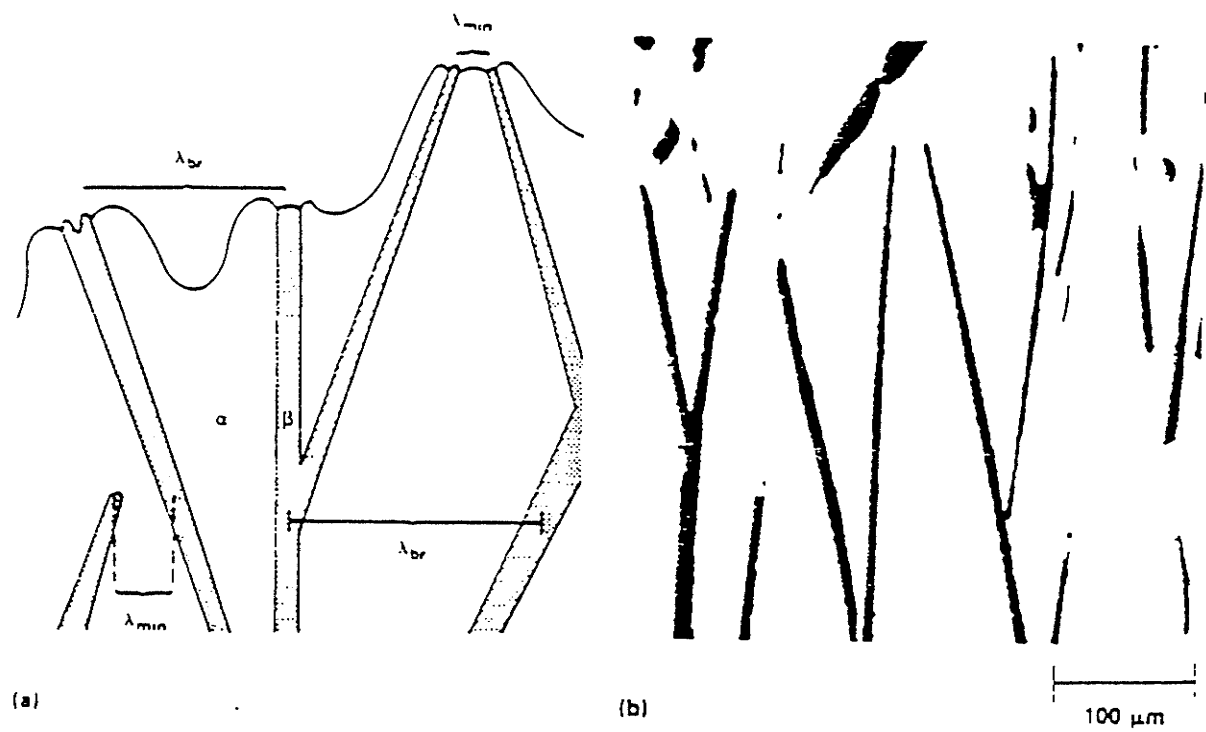


Figure 2.14

Growth of irregular eutectic[6].

- (a) Schematic of branching of the faceted phase at λ_{br} , termination at λ_{min} , and the corresponding shape of the solid/liquid interface.
- (b) Iron-carbon eutectic alloy directionally solidified at $R=0.0017\mu\text{m}/\text{s}$. Branching was induced by a rapid increase in R . Longitudinal section. As-polished.

2-3-3 HYPO- AND HYPER-EUTECTIC Al-Cu ALLOYS

Considerable progress has been made in recent years towards understanding the solidification behaviour of metals. For the Al-Cu system, Cu is mainly added to increase the strength at low temperatures by heat treatment and at higher temperatures through the formation of compounds. There has been appreciable interest in the Al-CuAl₂ eutectic as a composite material because a more or less perfect lamellar structure can be obtained. The mechanical properties of unidirectional solidified Al-Cu castings containing up to 15 wt% solute have been determined with respect to the volume fraction of inter-dendritic eutectic[24,25].

According to the Al-Cu equilibrium diagram, both the liquidus and the solidus at the aluminum end are reasonably straight lines. Thus, the partition coefficient k ranges from 0.14 to 0.17 and applies over the range from zero to 33% Cu. The θ phase, which is usually reported as CuAl₂, freezes directly from the melt at 53.3% copper and 864K. It has a limited range of composition from 52.5 to 53.9% copper. CuAl₂ is tetragonal; space group I4/mcm; 12 atoms in the unit cell: lattice parameters $a = 6.066 \times 10^{-10}$ m, $c = 4.874 \times 10^{-10}$ m; density 4340 Kg/m³. Hypo-eutectic Al-Cu alloys contain less than 33.2 per cent Cu and having a structure of α (Al phase) matrix with eutectic θ phase distributed in it. Hyper-eutectic Al-Cu alloys contain from 33.2 to 52.5 per cent Cu and have a structure of primary θ phase in a eutectic matrix.

Dendritic solidification of Al-Cu alloys has been examined over a range of solidification rates and alloy compositions [7,26-28]. It is found that the Al₂Cu dendritic morphology changes with freezing rate and alloy compositions[7]. The

dendritic spacing has also been analyzed as a function of the solute concentration and the freezing rate[27]. Furthermore, the tip radius of curvature and tip concentration were measured[26]. The results showed that the dendritic arm spacing is controlled by the diffusion of solute in the liquid.

Solidification of metals and alloys is influenced greatly by convective mixing. Macroscopic natural convective effects in directional dendritic solidification of Al-Cu alloys are studied experimentally as a function for density gradient orientation relative to the gravity vector in the inter-dendritic and bulk liquid [29]. The effect of gravity driven convection on macro- and micro-segregation microstructure for Al-Cu alloys has also been studied[54]. The internal and external shrinkages in a unidirectional solidified AL-4.5wt%Cu alloy has been analyzed to determine the inter-dendritic flow[30,31]. It was shown that, when the top of the ingot reached a pasty state in the course of solidification, a capillary pressure appeared at the top and made inter-dendritic liquid flow very difficult.

The macrosegregation behaviour of Al-Cu alloy has been discussed by Flemings and Sharp et al [32,33,49,50]. It was suggested that the interfaces adjust their shape in such a way as to eliminate any constitutional supercooling. Moreover, the micro-segregation behaviour was analyzed as the effect of the solidification rate[33]. It was found that the normalized θ phase content increased with increasing cooling rate at about 180K/S (growth rate of 1cm/s). Beyond this cooling rate, it decreased with increasing cooling rate. Cahoon[48] re-evaluated inverse segregation in an Al(rich)-Cu system. Computer programs have been developed[53] to determine the theoretical

maximum segregation in binary-alloy systems and the segregation distribution in a unidirectional solidified ingot. Theoretically calculated inverse segregation data has been compared with experimental data[54]. Reasonable agreement has been obtained.

For hyper-eutectic Al-Cu alloys, research work has been involved in studying the morphology of primary Al_2Cu phase[7] and the macroscopic natural convective effects in directional solidification[29]. Limited knowledge of hypereutectic Al-Cu alloy system has been gained and future research work is required.

2-4 SEGREGATION

Constitutional undercooling is primarily the result of the difference in composition between the solid and liquid phases during solidification. This difference not only produces undercooling when the temperature conditions are suitable but it is also responsible for the segregation of the solute that exists in the final solid alloy.

Segregation may be categorized into two types: micro-segregation and macrosegregation. Micro-segregation includes short-range differences in concentration such as those found between cells, dendrites and grains. Macrosegregation refers to long-range variations in composition found between the outside and the centre of a casting or ingot.

2-4-1 MICROSEGREGATION

The first and simplest approach to a quantitative description of microsegregation in dendritic solidification was described by Bower, Brody and Flemings[34]. The solute redistribution is shown schematically in Figure (2.15) and the local solute-redistribution equation is given as:

$$C_s^* = k C_0 \left\{ \alpha / (K-1) + [1 - \alpha k / (k-L)] (1-f_s)^{(k-1)} \right\} \quad (2-26)$$

where k is an equilibrium distribution coefficient defined as $k = C_s/C_l$ and $\alpha = D_s t_f / l^2 = 4 D_s t_f / d^2$. Here l denotes one half of the dendrite arm spacing, d , and t_f is the local solidification time. C_s^* is the composition of the iso-concentrate surrounding the

f_s weight fraction of solid both during and after solidification of the volume element.

Figure (2.16) shows microsegregation for an Al-4.5%Cu alloy calculated according to equation (2-26). It is shown that the solute redistribution depends only on the dimensionless ratio α . However, the ratio α is relatively constant over wide ranges of cooling rate, thus leading to the relative constancy of segregation observed at different cooling rates. Experiments conducted on a low-alloy steel substantiate this assertion[38].

Bower, Brody and Flemings [34,35] also simplified this equation by neglecting the parameter α because of the sufficiently low ratio of thermal gradient during solidification. Then the equation reduces to

$$C_s^* = k C_0 (1-f_s)^{k-1} \quad (2-27a)$$

Equation (2-27) is recognized as the non-equilibrium level rule, or Sheil's model. It applies to a region whose size is of the order of that of a dendrite arm. For example, for systems with eutectic phase diagrams, the maximum composition in the single phase corresponds to KC_E , where C_E is the eutectic composition. Once this composition is achieved, the intercellular liquid will freeze with a eutectic structure. Equation (2-27) can be used to predict the volume fraction of the eutectic phase, f_E ,

$$f_E = (C_E/C_0)^{1/k-1} \quad (2-27b)$$

In Al-Cu alloys, a eutectic is found[25] when the initial composition is very low although the limit of solid solubility is in excess of 5% and the eutectic composition is 33%.

In order to account for solid diffusion during and after solidification, equation (2-27a) yields:

$$C_s^* = kC_0 [1 - f_s / (1 + \alpha k)]^{k-1} \quad (2-28)$$

and, for parabolic thickening[27]

$$C_s^* = kC_0 [1 - (1 - 2\alpha k)f_s]^{[(k-1)/(1-2\alpha k)]} \quad (2-29)$$

Samples have been abruptly quenched at various temperature during and after solidification [35,36]. Segregation has been measured to compare with results from equation (2-28).

Equations (2-28) and (2-29) were used to compute the weight fraction for the second phase formed in several Al-Cu alloys [27]. Results are plotted in Figures (2.17) and (2.18). The above equations, however, are not suitable for describing microsegregation having significant "back-diffusion". This deficiency happens because C_s^* approaches kC_0 as α becomes large at any fraction solid, f_s . Figure (2.19) shows the results of one such set of calculations.

Recently, Clyne and Kurz [39] modified equations (2-28) and (2-29). They replaced the term α by α' given in the following expression for the parabolic advance of the dendrite:

$$\alpha' = \alpha\{1-\exp(-1/\alpha)\} - 1/2 \exp(-1/2\alpha) \quad (2-30)$$

This modification is based on the analytical solution of the previous model that involved an assumption which led to the nonconservation of solute. However, this model has been criticized for the lack of a physical basis at intermediate values of α . Sarraeal and Abbaschian[40] proposed a model to calculate the eutectic fraction in rapidly solidified alloys. Kurz et al.[41] used Burden and Hunt's analysis [10] with a model for eutectic growth undercooling. Assuming that the effects of back diffusion and temperature depressions are additive, the eutectic fraction can be derived as:

$$\begin{aligned} f_E^c = & (1-f_E^0) [C_{sm}^{new}/ kC_t]^{1/(k-1)} - 2\alpha'k/(1-2\alpha'k) \\ & + 1/(1-2\alpha'k) [C_s^{max}/kC_0]^{[(1-2\alpha'k)/(k-1)]} \\ & - [C_{sm}/ kC_0]^{1/(k-1)} \end{aligned} \quad (2-31)$$

where f_E^c is the eutectic fraction due to the combined effects. Furthermore, $f_s^0 = (C_t - C_0) / C_t(1-k)$, α' is given by equation (2-30), and $C_{sm}^{new} = (kC_t[f_E^0 / (1-f_s^0)])$.

Giovanola and Kurz[41] considered a large concentration gradient existing in the tip region of the cellular on a dendritic array. They proposed a model consisting of two functions for the concentration versus fraction solid relationship. One function described the transients in the region around the dendrite tips and the other function was used for the region of complete liquid mixing of the interdendritic liquid. According to the resulting model, the concentration of the first solid to form is high, undergoes little change up to high solid fractions, and increases only in the last stages

of solidification. This behaviour is not considered by Scheil's or Brody and Fleming's analysis which leads to very different predictions of the microscopic concentration profile. The model of Giovanola and Kurz seems to give reasonable agreement with experimental results. Furthermore, Skolianos[42] studied the dissolution kinetics of nonequilibrium ternary eutectic (Al-4.5wt%Cu-2.0wt%Mn) by using a cylindrical diffusion model. Their model described the dissolution of the nonequilibrium ternary eutectic rather well for short times but not for longer periods.

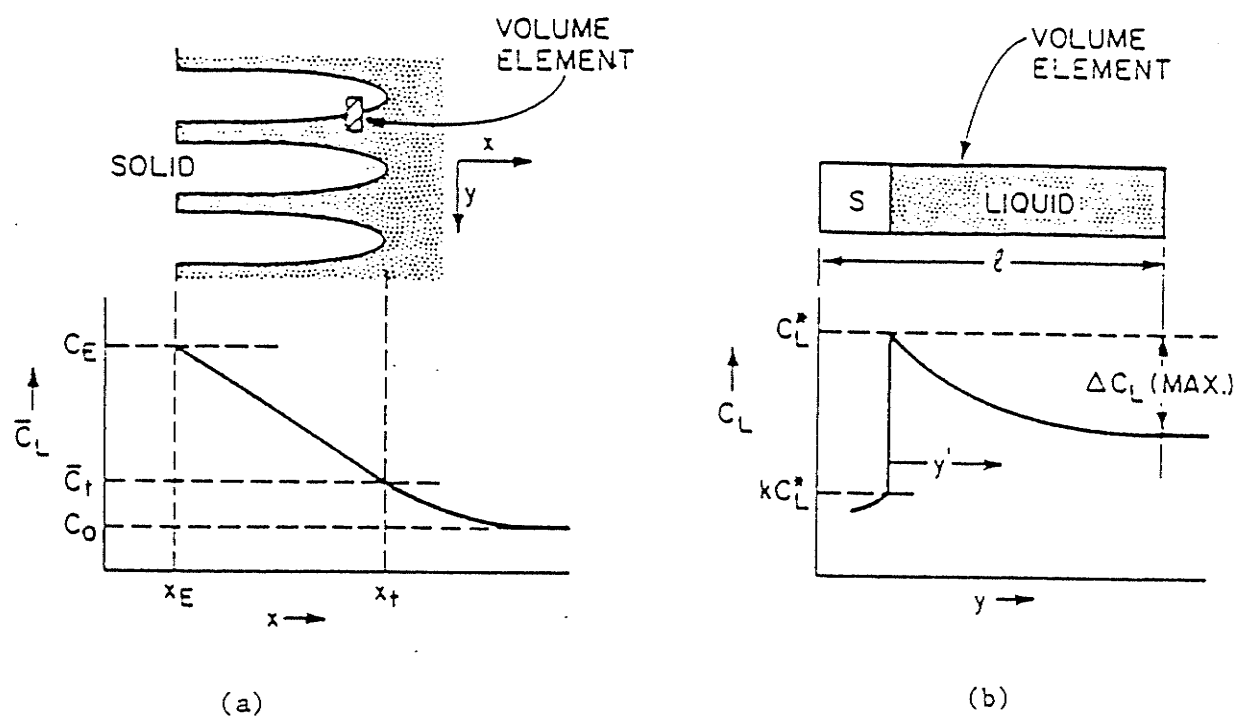


Figure 2.15

Solute redistribution in cellular growth[4].

- (a) Cellular growth and solute distribution in the growth direction
- (b) An enlarged "volume element" and solute distribution transverse to the growth direction

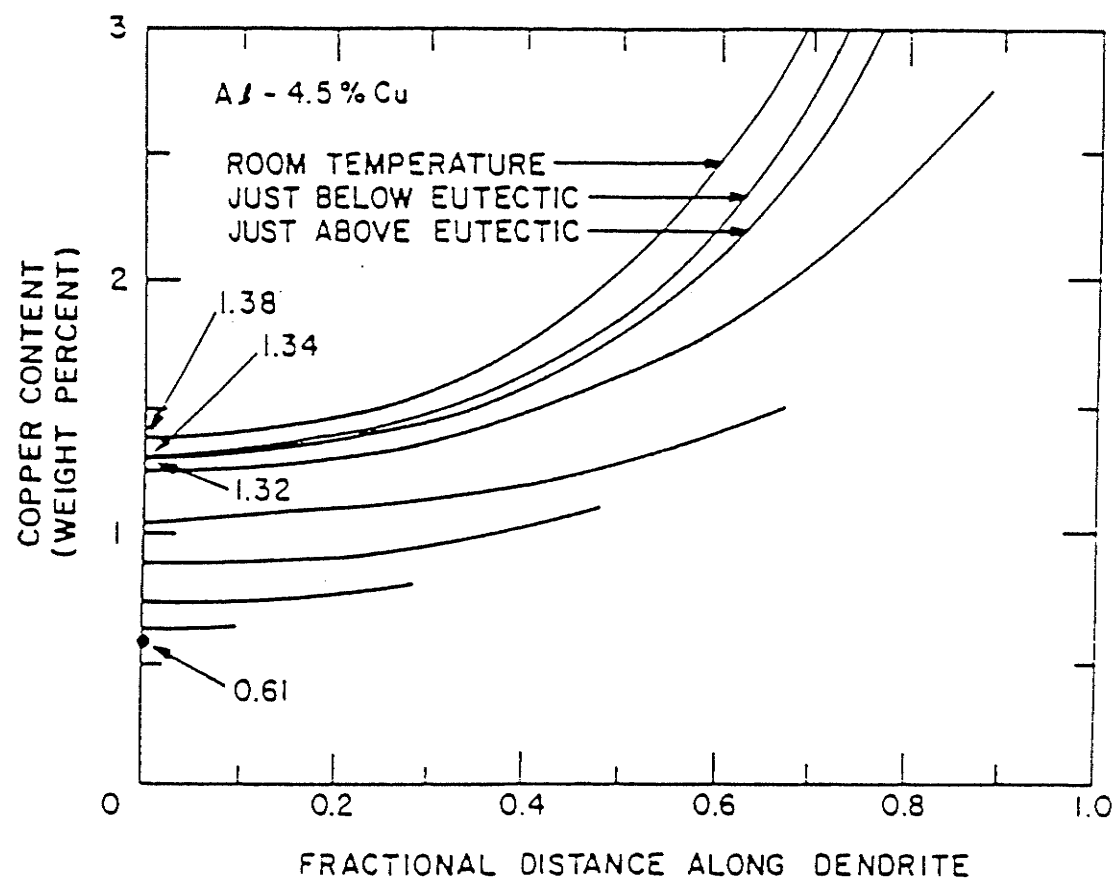


Figure 2.16

Effect of solid diffusion during solidification on the composition distribution across dendrite arms calculated for $t_r/d^2 = 3.3 \times 10^8$ [4].

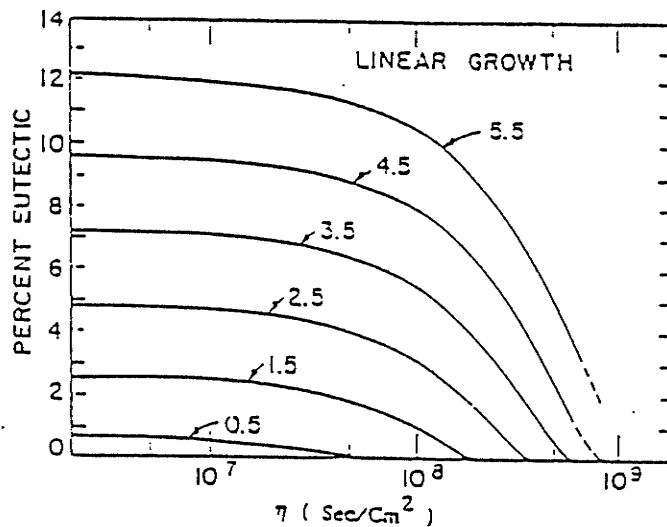


Figure 2.17

Weight percent nonequilibrium eutectic formed as a function of η for several Al-Cu alloys with less copper than the solubility limit.(linear growth) [54]

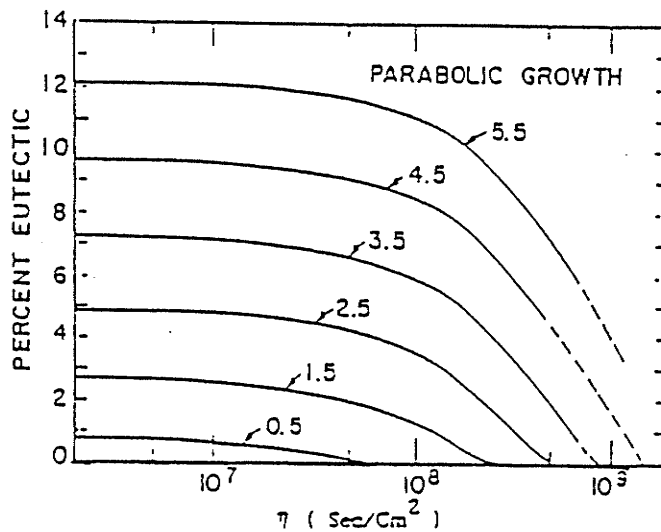


Figure 2.18

Weight percent nonequilibrium eutectic formed as a function of η for several Al-Cu alloys with less copper than the solubility limit.(parabolic growth) [54]

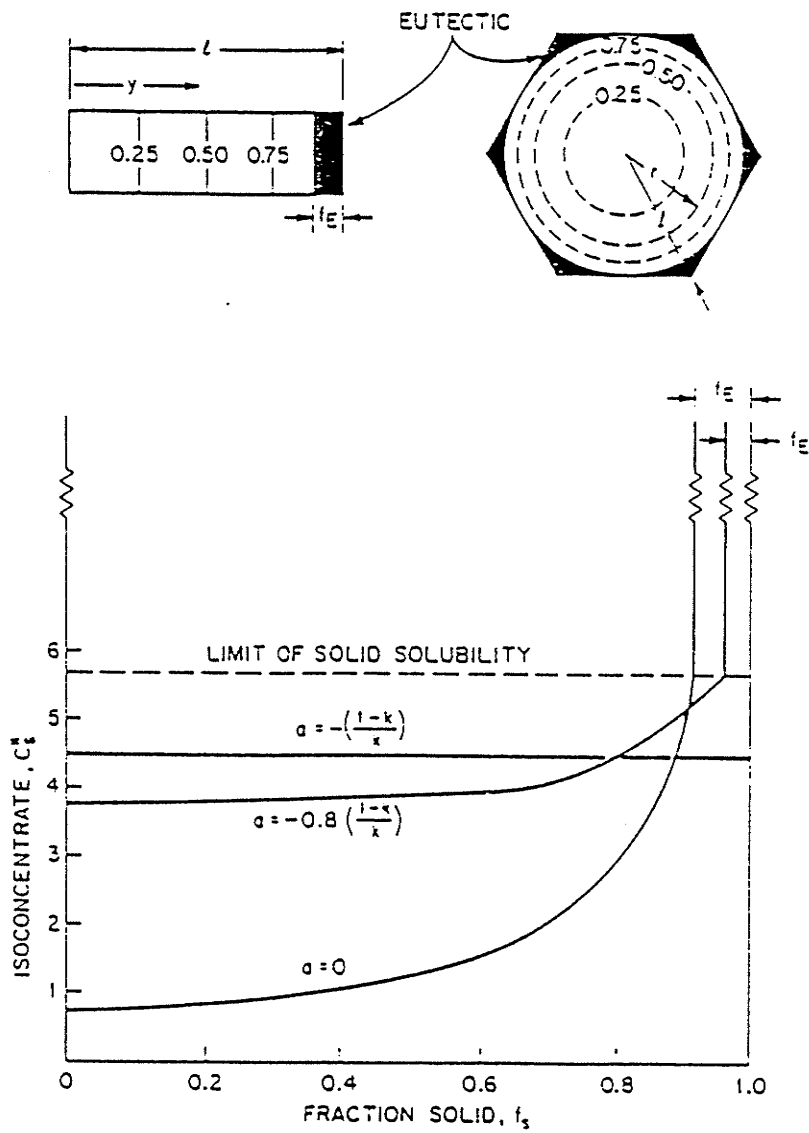


Figure 2.19

Microsegregation in cellular solidification. At the top are shown two idealized volume elements, the one on the left for elongated (two-dimensional) cells and the one on the right for regular cells. Dotted lines show isoconcentrates at the values of f_s noted. The graph plots microsegregation for an Al-4.5Cu alloy [4].

2-4-2 MACROSEGREGATION

Macrosegregation is the phenomenon of solute variation taken over large distances of a cast structure. Flemings and Nereo[32] considered that the mechanism of all types of macro-segregation was the same. It was one of interdendritic flow of solute-rich liquid. The solute is transferred to the liquid as part of the solidification process. The driven forces of the movement has been summarized as:

- .Solidification Contraction
- .Effect of Gravity on Density Differences Caused by Phase or Compositional Variations
- .External Centrifugal or Electromagnetic Forces
- .Formation of Gas Bubbles
- .Deformation of the Solid Phase due to Thermal Stress and Static Pressure
- .Capillary Force

2-4-2-1 NORMAL SEGREGATION

When plane front solidification occurs, the solid composition of the initially solidified portion is low, having an approximate value of kC_0 , which gradually increases with time. This behaviour occurs as a result of diffusion pushes the solute ahead, leading in turn, to a higher concentration at the finally solidified portion or the ingot centre.

Allen and Hunt[43] calculated the solute distribution at low velocity(R) as:

$$C_s = k_e C_0 (1-f_s)^{k_e-1} \quad (2-32)$$

where f_s is the fraction of volume solidified and C_s is the solute concentration in the solid attached solid/liquid interface. k_e is the effective distribution coefficient given by:

$$k_e = k_0 / [k_0 + (1-k_0)e^{-\Delta}] \quad (2-33)$$

where $\Delta = R\delta/D$ is the thickness of the stagnant layer, and D is the diffusion coefficient in the liquid. Chalmers[2] represented this type of segregation by a single curve, relating the concentration of a solute to the distance from the start of solidification. The form of this curve depends upon the equilibrium distribution coefficient k_0 , the rate of solidification, R , and the amount of mixing by fluid motion. The actual segregation resulting from a solidification process depends very much on the geometry of the sample, as this influences both the rate of solidification and the amount of convection.

2-4-2-2 INVERSE SEGREGATION

Inverse segregation occurs when solute is rejected during solidification. A higher concentration is present in regions that solidified earlier. This type of segregation occurs only in alloys that contract during solidification, and it happens progressively as freezing proceeds. This contention is supported by the observation of Adams[44]. The shrinkage may cause motion of the most "solute enriched" liquid in a

direction opposite to that of the general solidification front. Kirkaldy and Youdelis[45] further developed the quantitative approach proposed originally by Scheil[46]. For a typical binary eutectic alloy system, the solute concentration C is given by:

$$C = (m_{lE}C_{lE}/a_E + m_{sE}C_{sE})/(m_{lE}/a_E + m_{sE}) \quad (2-34-1)$$

where m_{lE} and m_{sE} are the liquid and solid masses in a representative volume just at the eutectic temperature. On the other hand, the C_{lE} and C_{sE} are the mean solute concentration in the liquid and cored crystals, respectively. a_E is the eutectic contraction coefficient, defined as the specific volume ratio of the eutectic solid to eutectic liquid, viz. $a_E = V_{sE}/V_{lE}$. At a concentration other than that of the eutectic, a is defined by:

$$a = V_s/V_l + (C_l - C_s)/V_l (dV_l/dC_l) \quad (2-34-2)$$

where C_s refers to the solute's equilibrium concentration in the solid. The terms in equation 2-34-1 are calculated from the stepwise integration of the following equation. m_{le} is calculated from

$$\int_L^{m_{l,E}} \frac{dm_L}{m_L} = \int_{C_0}^{C_{l,E}} -\frac{K}{A} \frac{dC_L}{C_L} \quad (2-34-3)$$

where $A = C_s/(C_l - C_s)$, or $A=1-K_0$, where K_0 is the equilibrium distribution coefficient. The value of K is given by

$$K = \alpha [1 - \frac{1}{V_L m_L} \int_{m_L}^{m_L^*} V_L' (\frac{1-\alpha'}{\alpha'}) \frac{dm_L''}{dm_L'} dm_L'] \quad (2-34-4)$$

where m_L^* is the liquid composition at the base of the dendrites ($m_L - m_L^*$ is the mass fraction of liquid available for further dendritic growth), and dm_L''/dm_L' is a contraction factor calculated from solidification parameters as illustrated in Figure (2.20). m_{SE} is calculated from

$$\int_0^{m_{SE}} \frac{dm_S}{m_S} = \int_L^{m_L^*} \frac{dm_L}{\alpha} \quad (2-34-5)$$

and the solut in the cored dendrites, $C_{SE}m_{SE}$ is calculated

$$\int_L^{m_{SE}} C_S dm_S = \frac{K}{\alpha} \frac{(1-A)}{A} \int_{C_0}^{C_L^*} m_L C_L \quad (2-34-6)$$

The agreement between the segregation, calculated as a function of the alloy compositions of different alloys, also shows good agreement with experiments[45,47]. Fig.(2.21) shows the resulting experimental and theoretical curves for the maximum segregation of a Al-Cu system. However, Cahoon[48] has re-evaluated inverse

segregation in the Al-Cu system and has shown that previous agreement between the theoretical and experimental values may be somewhat fortuitous.

Fleming et al[49,50] developed equations to predict the effects of the solidification variables on macrosegregation. They calculated the solute distributions for unidirectional solidified Al-4.5% Cu ingots cast under various thermal conditions[51]. Cahoon and Youdelis[52] have compared the equations derived by Flemings and Nereo with that formulated by Kirkaldy and Youdelis[45]. In the treatment of Kirkaldy and Youdelis, the mass distributions are simply assumed or measured without prior and explicit association of the mass distributions to a velocity parameter. The treatment of Flemings and Nereo permits solidification conditions more complicated than the simple unidirectional case to be considered. Both the Kirkaldy-Youdelis and Flemings-Nereo treatments consider a zone of dendrite "expansion" followed by a "steady-state" zone. However, Flemings and Nereo failed to consider a zone of "collapse" which begins at the base of the first dendrites to reach the top of the ingot.

Computer programs have been developed by Cahoon and Youdelis[53] to provide quick and accurate methods for determine the theoretical maximum segregation in binary-alloy systems and segregation distribution in a unidirectional solidified ingot. Figure (2.22) shows the calculated maximum segregation in a hyper-eutectic Al-Cu system.

Inverse segregation of Al-4.5%Cu and Sn-15%Pb alloys have also been calculated theoretically by using this computer program and equations (2-34-1 to 2-34-

5)[54]. The observed experimental segregation data agree well with the theoretically calculated data for a Al-4%Cu ingot. However, a similar comparison for Sn-15%Pb sample does not conform to the experimental values of inverse segregation.

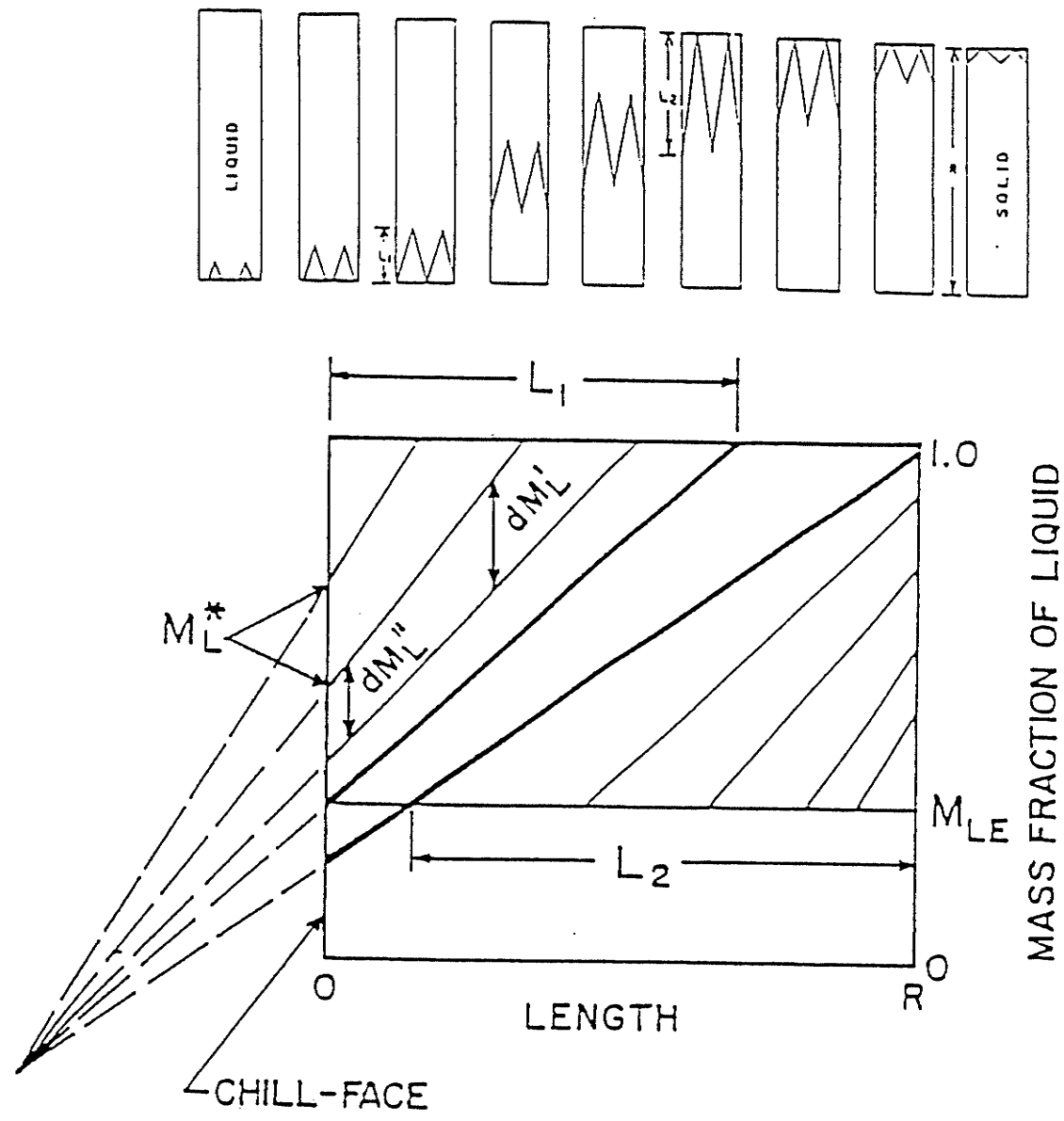


Figure 2.20

Parameters for calculating inverse segregation[54].

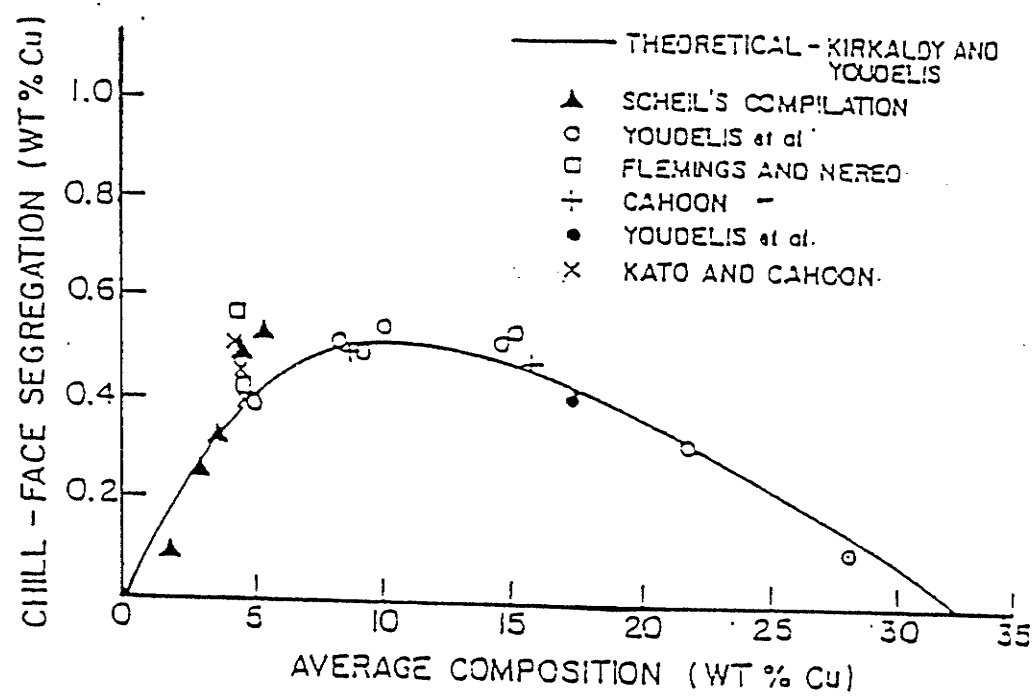


Figure 2.21

Experimental values for chill-face segregation in Al(rich)-Cu system[54].

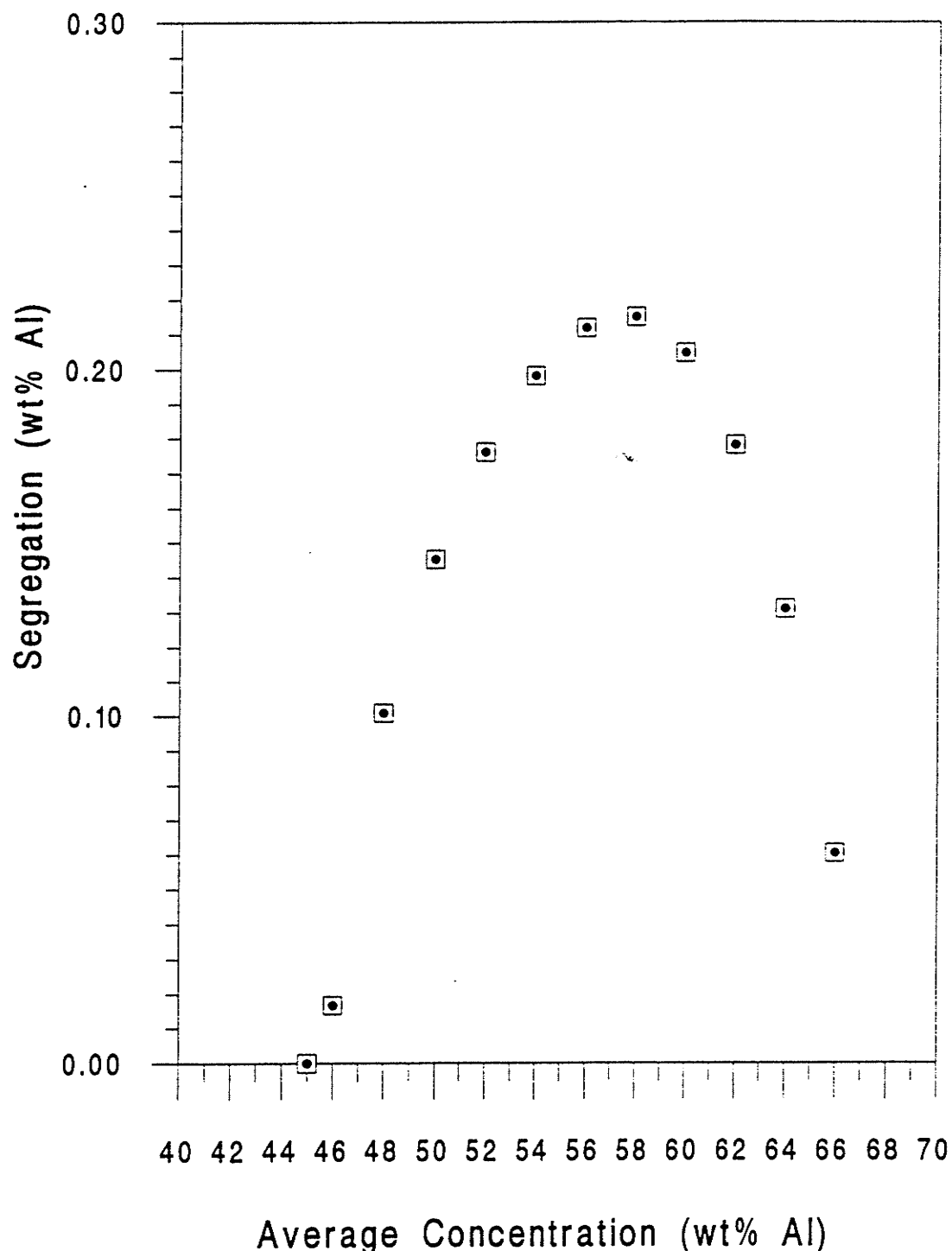


Figure 2.22

Maximum segregation in $\text{Al}_2\text{Cu}-\text{Al}$

2-4-2-3 GRAVITY SEGREGATION

When liquid or solid constituents separate because of a difference in density, gravity segregation is said to occur. As solute is rejected during solidification, density gradients established in the liquid, which sets up convection currents that carry the solute toward the top or the bottom of the space in which the liquid moves.

Flemings, Nereo and Mehrabian [49-51] have published a general solution for macrosegregation which considers the dynamics through a volume element where the forces acting correspond to a solid contraction, liquid contraction and gravity. In addition, Mehrabian et al[50] have discussed the mechanism whereby, under critical conditions, an upward flowing liquid becomes superheated and can dissolve dendrite branches in its path to form visible trails or "pipes" of high solute content. These trails have been observed in experiments on Al-Cu alloys. They propose that the critical condition for the formation of channel-type defects is when the direction of the interdendritic fluid flow vector goes from the colder to the hotter regions of the casting. A number of experiments have been done on lead-tin alloys[49,55] to determine the extent of macrosegregation and freckle formation resulting from density differences in the liquid. Wang et al[56] have shown that in Pb-15%Sn alloys, macrosegregation increased with increasing thermal gradients, and also decreased with increasing cooling rates because the local solidification time increases. This results in coarse dendrites with higher permeability, so that gravity induced convection takes place more easily and increases the macrosegregation.

2-5 EFFECT OF CONVECTION

Solidification process is frequently dominated by natural convection in the fluid phase which thus controls the properties of the materials grown. The growth of the liquid/solid interface, ie. the atom attachment with the metallic crystal, is related to solute diffusion and convection. The solute and latent heat have to be transferred away from the advancing interface. This characteristic determines the boundary layer, a stagnant zone whose thickness is controlled by solute diffusivity and convection. The stronger the convection is, the smaller the thickness of the boundary layer. The effect of convection on the interface is shown by the effective distribution coefficient k_{eff} given by equation(2-33). This expression can be used to describe solute redistribution in crucibles of finite extent provided only that the thickness, Δ , of the boundary layer is small compared with the length of the crucible. In this case, a dynamic equilibrium is attained between the bulk melt and growing solid and equations identical to equation(2-27), except that the equilibrium partition ration k_0 is replaced by the effective partition ratio k_{eff} .

Themo-solutal convection is well known to be the source of various segregation phenomena observed in castings. Experimental evidence has been obtained on lead-30wt% thallium alloys on the convective patterns ie the melt adjacent to the solidification front[59]. During solidification, thermal gradients in the melt cause density gradients that, under a gravitational field, result in a buoyancy driven convective flow. Heat and fluid flow phenomena associated with laminar buoyancy-induced natural convection relevant to material processing have been extensively

studied based on the fundamental conservation laws of mass continuity, momentum, energy, and species convection[60-63]. The influence of Pr number on the buoyancy-induced, transport phenomena has been investigated through two-dimensional, steady-state computations for flow in a square enclosure at two different vertical wall temperatures, and both with as well as without solidification [64]. It is shown that, with solidification, more vigorous convection induced by higher Rayleigh number (Ra), results in a stronger Pr influence on the maximum stream function and Nusselt number, but not on the global enthalpy patterns. It is also found that features such as morphology of the phase boundaries may be more sensitive to Pr variations than momentum and heat transport.

Gravity dependent, interdendritic fluid flow has been modelled analytically and numerically by Mehrabian et al[65]. Simpson and Flemings[66] used this analysis to illustrate the gravitational influence on interdendritic flow for the simple case shown in Figure (2-23). They indicated that there are two ways to reduce the flow parallel to isotherms and, hence, reduce segregation. First, if the isotherms are more nearly horizontal, g_{\parallel} and, in turn, v_{\parallel} will be reduced. Second, if the cooling rate on the thermal gradient in the mushy zone increases, the total flux of the solute will decrease. Now v_{\parallel} is independent of the thermal gradient so that increasing the thermal gradient will reduce the width of the mushy zone and, thus, the total flow parallel to the isotherms. Increasing the cooling rate will reduce the time available for solute flow to occur and, hence, reduce the segregation. Maples and Poivier[67] described a model of a binary alloy solidifying horizontally by analyzing the transients of the solid/liquid

zone. The effect of the gravity force on the solid/liquid zone of an Al-4.5wt%Cu alloy is given in Figures(2-24) and (2-25). With zero gravity, the flow of the interdendritic liquid was due solely to solidification shrinkage and the flow was normal to the isotherms. Solidification shrinkage and macrosegregation were investigated in Al-4.5wt%Cu alloy ingots solidified unidirectional upwards from the bottom [30,31]. It was shown that, when the top of the ingot reached a pasty state in the course of the solidification, a capillary pressure appeared at the top and made the interdendritic liquid flow very difficult. The macrosegregation in the ingots was insignificant because the solidification shrinkage was compensated mostly by the deformation of the ingots rather than by the interdendritic liquid flow.

Macroscopic natural convective effects in directional dendritic solidification of Al-Cu alloys were studied experimentally as a function of density gradient orientation relative to the gravity vector in an interdendritic and bulk liquid[48]. It was found that the structure of the natural convective flow and its coupling with the bulk liquid essentially depended on the orientation of the density gradient in the interdendritic liquid. Different types of macrosegregation correspond to different convective modes. A scaling analysis was also performed to give a general criterion of the transition from diffusive to convective transport conditions. A dimensionless parameter Γ was defined by $\Gamma=V^*/R$, in which V^* is the interdendritic flow velocity and R is the solidification rate. Parameter, Γ , gives a measure of the first order effect of interdendritic flow on segregation. In a vertical configuration, however, only second order effects can occur. Such effects would be associated with a deformation of the dendritic front. Scale

analyses have been used to establish the order-of-magnitude of force arising from natural convection[84]. The result showed that shear forces were too small to dislodge molecules from the crystal surface or alter the structure by unfolding.

Further research has been concerned with the effect of natural convective patterns in the dendritic primary spacings. Primary spacing in a normal gravity environment have been found to be much smaller than those measured in a microgravity environment[68]. This difference demonstrates that natural convection reduces (by a factor of about four) the primary spacings of the Al(Cu) system at the low growth rate studied. The coarsening of directionally solidified α -phase/liquid mixtures was also investigated in Al-4,10 and 20 wt% Cu alloys, as a function of temperature, composition and presence or absence of forced convection[69]. Isothermal dendritic coarsening in the absence of convection operated in two stages. I: the dendritic structure broke down through remelting into fragments which spheroidized quickly; II: the spherical particles coarsened slowly. The coarsening rate of the dendritic or particulate solid increased with temperature and copper dilution. Alloy inoculation with titanium slowed coarsening, yielding finer dendritic microstructure. A coarsening model was introduced which showed that coarsening is faster in the presence of forced convection, because of the resulting decrease in the solute diffusion-boundary layer thickness.

The influence of convection on the coarsening of secondary dendrite arm spacing in an AlSi alloy has been studied[76]. Under 1g and μ g, there are different kinds of convection, which all intensify the natural transport in the melt and which

were subsumed under the rules of material transport by diffusion. Only under 1g conditions did the axial and radial temperature cause thermal convection in the melt. Moreover, the axial composition gradient also caused gravity driven convection. It has been assumed that these kinds of convection also had an effect in the space between the dendrites. Figure(2-26) shows this schematically. In both 1g and μ g conditions, there must also be microconvection in the area between the first solidification front (I.SF) and second solidification front (II.SF). This microconvection was caused by the jumps, ΔV , in the volume during the transition from the liquid to the solid phase. Figure(2-27) illustrates this effect schematically for different crystallization velocities V_{SF} . It is apparent that a higher velocity of the solidification front caused an increase in the convection. The difference in the coarsening of dendrite arms in μ g can be traced to the different convection values caused by the volume jump.

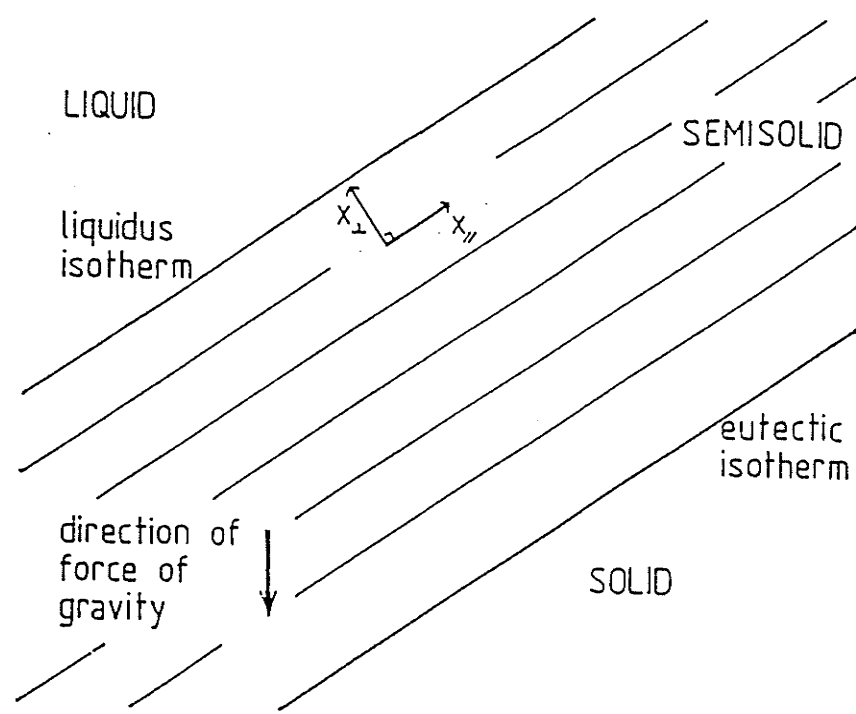


Figure 2.23

Situation analyzed: flat, parallel isotherms at an angle to the vertical[66].

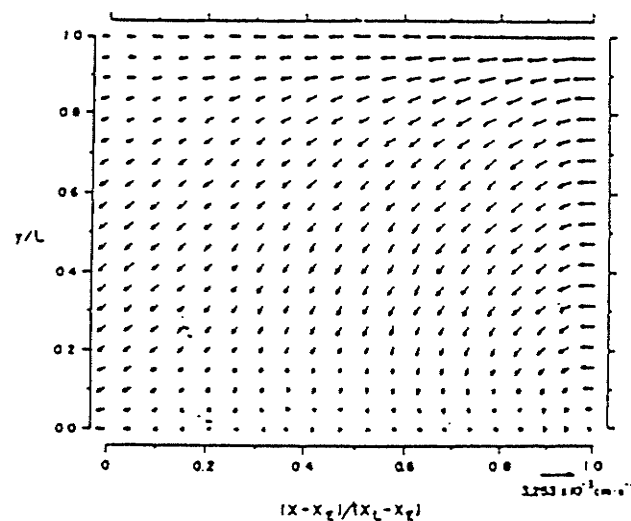


Figure 2.24

The effect of gravity on the velocity of inter-dendritic liquid in AL-4.5wt% Cu alloy[67].

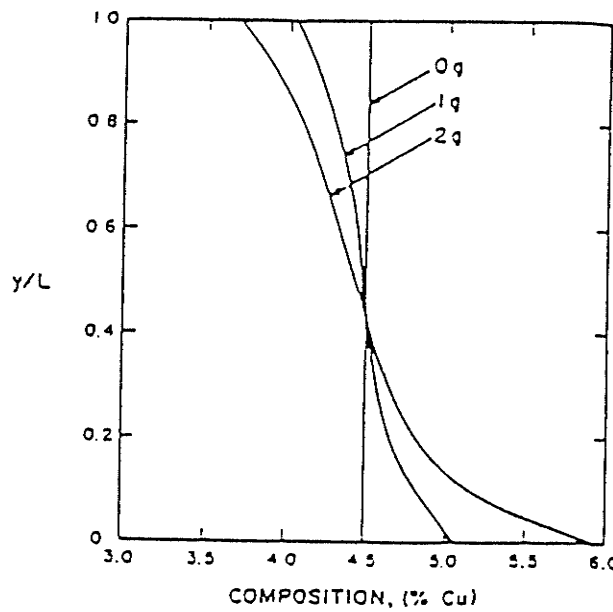


Figure 2.25

The effect of gravity force on macrosegregation in AL-4.5wt% Cu alloy[67].

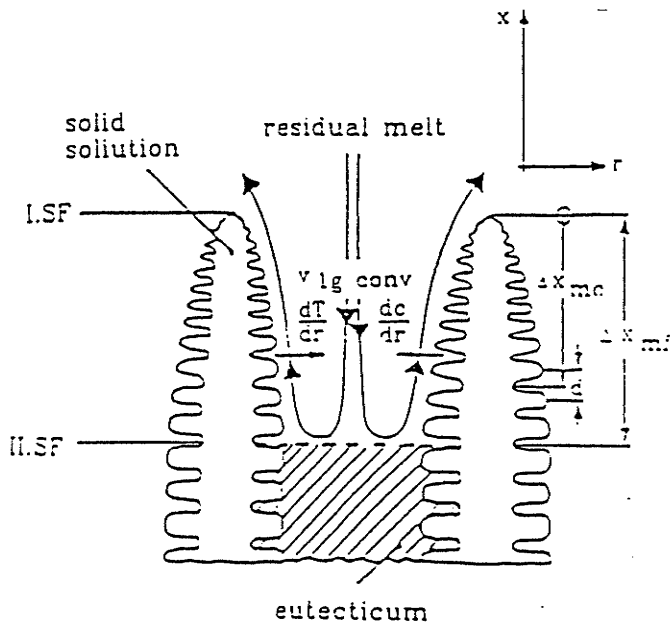


Figure 2.26

Thermal and concentration convection in the space between the dendrites urged by gravity(schematically)[76].

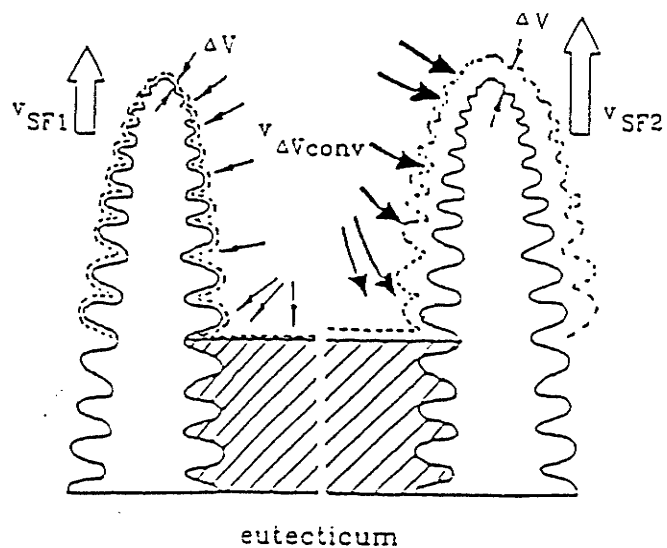


Figure 2.27

Situations of microconvection $v_{\Delta V \text{conv}}$ urged by the jump of changing the volume during phase transition liquid-solid having different velocity of crystallization(schematically)[76].

2-6 MICROGRAVITY EXPERIMENTS

The most important effect of the elimination of gravity during alloy solidification is the disappearance of buoyancy-driven convection and sedimentation. Under microgravity conditions, the gravity induced thermal and compositional convection are negligible. However, some convection may still result from the surface tension-driven flow and from the pushing of the liquid by the solidifying phases at the interface. A microgravity environment, therefore, can be a helpful tool for an experimental investigation of the effect of a single transport mechanism on the role of fluid mechanics in the solidification processes. Table 2.1 shows the major effect of microgravity on material processing[70].

Table 2.1 The relationship between solidification mechanism and gravity

GRAVITY RELATED TRANSPORTATION MECHANISM	
1) DENSITY DIFFERENCE $\Delta\rho(T;C)$ INDUCED BUOYANCY AND SEDIMENTATION	
2) $\Delta\rho(T)$ AND $\Delta\rho(C)$ INDUCED NATURAL CONVECTION	
GRAVITY INDEPENDENT TRANSPORTATION MECHANISM	
1) $\Delta\rho_{l-s} - 1/\Delta V_{ml-s}$ INDUCED CONVECTION	
2) $\Delta\sigma(T)$ AND $\Delta\sigma(C)$ INDUCED MARANGONI CONVECTION	

Here, $\Delta\rho$ is the density difference, $\Delta\sigma$ is the surface energy change, T is the temperature, C is the concentration. The $\Delta\rho(T,C)$ is the density difference resulting

from temperature and solute concentration changes and ΔV_m is the volume expansion at the melting temperature.

Some of the liquid properties also seem to be affected by a low-g environment. It has been suggested that the wetting properties of the substrate are modified which, in turn, will change the interface curvature. Also, the value of the liquid diffusion coefficient (D_L) is greatly reduced in a low-g environment[71].

Material processing in a microgravity environment is aimed at developing commercial materials as well as investigating basic phenomena to improve earth-based processing. Materials research in space has dealt with glasses and ceramics, crystal growth, electronic materials, metals and alloys, polymers, composites and biological materials[87]. Several microgravity studies on immiscible alloy systems such as Au-Ge, Pb-Zn, Al-Pb, Al-Bi, Pb-Sn-In and Pb-Zn-Sd have shown nearly complete phase separation. On the other hand, fine uniform dispersions have also been produced in microgravity in other immiscible systems such as Ga-Bi, Sb-Ag, Al-Sn-In, Cu-Pb-Al and Cd-Ga-Al. Materials processing in space may be disturbed in space by residual accelerations, or g-jitters, which act on the space carrier: atmospheric drag, the gravity gradient effect, vibrations, crew activities, etc. Because of the presence of thermal gradients (and, thus, density gradients) in the liquid phase, these residual accelerations may give rise to convective motions. In turn, the convective flows may act on the solute field and lead to heterogenieties of the dopant in the grown crystal. Thevenard and Hadid[72] predicted the possible influence of g-jitters convection in an ideal crystal growth configuration. The maximum velocity, the velocity profiles and phase

shifts have been analyzed. Better understanding on fluid motion has been obtained to explain the observed results.

Directional solidification under microgravity has been used to study various basic phenomena and processing methods in a number of different systems. Macro-and micro-segregation during solidification of binary alloys (Pb-Sn) and cast irons have been studied to verify dendritic models and the role of gravity-driven phenomena such as convection and sedimentation. The behaviour of dispersions and bubbles interacting with solidification fronts has also been investigated in model systems such as naphthalene with nitrogen or argon, little or no bubble movement has been observed. Several isothermal processing experiments have also been performed to study crystal growth and morphology during solidification, diffusion in liquids, and wetting behaviour [68,73,76,77,79]. However, current theories of fluid motion are inadequate to explain the observed results.

2-7 Proposed Research

Dendritic growth in metals and alloys is a common mechanism of crystallization from the melt. The review presented here shows that macro and micro-segregation is a result of dendritic solidification. Solutal convection is well known to be the source of various segregation phenomena observed in castings. Analytical and experimental work has been done on the effect of low gravity on macrosegregation as well as on dendrite arm spacings for hypoeutectic Al-Cu alloys. Not much work, however, has involved the hypereutectic Al-Cu region.

In this work, two apparatusae (see Figure 3.1 and 3.4) were designed and built in order to accormodate the microgravity experiment. The apparatus used in series A was able to solidify the sample in a few seconds to minimize diffusion in the solid and to accomodate the undirectional solidification in KC-135 flight. The apparatus used in series C, the three zone gradient-freeze QUESTS furnace, provide slower cooling rates in three zones. Solidification experiments in series C were conducted on the ground as well as in space shuttle. A slow solidification rate results in reasonably flat solid/liquid interface where steady state solidification can be achieved.

The morphology, micro- and macro-structure, as well as macrosegregation phenomenon were studied for the case of solidification parallel or perpendicular to the direction of gravity on ground. Comparisons are made with the samples solidified in microgravity environment. An attempt has been made to review the mechanism of the phenomenas. Such research can lead to a better understanding of the effect of gravity-induced convection and sedimentation on solidification of hyper-eutectic Al-Cu alloys

can be achieved.

CHAPTER III

EXPERIMENTAL TECHNIQUES & PROCEDURE

3-1 PREPARATION OF THE ALLOYS

Experimental alloys were prepared from a master alloy Cu-47%Al by adding the appropriate amount of Al or Cu. The purity of the alloying elements was Al-99.99% and Cu-99.99%. All the alloys were prepared by melting the alloy in an induction furnace and casting the alloy in a metallic mould. The high frequency induction process used to make the alloys ensured chemical homogeneity of the alloys. However, a small loss of Al occurred due to oxidation. An addition of Al was needed in order to get the right composition. The alloys prepared for present study are listed in Table 3-1.

Table 3-1 The composition of alloys used in present study.

Series	Composition	Size(mm)	Method
A (1g)	Al-38Cu,Al-50Cu	28 hei.;15.9dia.	chill
B (1g)	Al-41Cu,Al-47Cu	28 hei.; 15.9dia.	chill
C (1g)	Al-36Cu,Al-38Cu,Al-40Cu	80hei.; 6dia.	gradient
KC-135 (0g)	Al-36Cu, Al-47Cu	5hei.;6dia.	chill

3-2 TEST SPECIMENS AND APPARATUS USED

Unidirectional solidification experiments were carried out in vertical furnaces. In order to separate the effects of diffusion and gravity in molten alloys, three sets of experiments were performed.

In the first series of experiments(series A), unidirectional ingots were solidified on ground in the apparatus designed for microgravity experiments aboard the KC-135. Cylindrical specimens of 28 mm height and 15.9 mm diameter were prepared from the three compositions Al-35%Cu, Al-38% Cu and Al-50%Cu ingots. The apparatus' assembly was designed for both ground-based as well as microgravity-based experimental work[54]. The system essentially consists of a crucible assembly enclosed in a stainless steel housing as indicated in Figure (3-1). The housing is suspended in a furnace and a chill block is located 2.5 cm from the end of the furnace. The melt is enclosed completely in a graphite crucible as seen in Figure (3-2). The crucible has a very thin 0.5 mm bottom. One end is in contact with the thin graphite base whereas the other end of the melt is in contact with the moving graphite plug which applies a slight pressure from the graphite wool (due to its spring action). Two thermocouples are inserted at various heights in the graphite crucible to record the temperature of the melt. The graphite crucible is held in place against the bottom of the stainless steel housing by using a ceramic cap and a rod under the spring load mechanism located on top of the cap. The aluminium chill block assembly was mounted with the furnace (standard resistance wire with a temperature controller) which has sealing caps at the bottom opening. A thin, 0.35 mm layer of solder sheet

(Pb-50Sn) was fastened on top of the chill block. The solder sheet essentially provides chilling as well as an excellent contact between the crucible assembly and the aluminium block. Consequently a solidification front will move against gravity[44].

In order to decrease the cooling rate, Al-41.0%Cu samples were also melted in the same furnace but solidified by means of air cooling as well as furnace cooling without direct chill from the bottom chill block. The temperature gradients in the liquid were measured during the growth by using three thermocouple located at different heights.

Similar tests were done on special flights (KC-135) at Houston by using very small sample of 6mm diameter and 5mm length[54]. The top and front view of the test equipment and the crucible assembly are shown in Figure (3-3) and (3-4). The samples were placed inside a graphite crucible in the stainless steel container. The same system of carbon block and graphite wool was used to prevent the melt from floating away from the crucible during zero gravity and also to apply pressure to the fluid melt and attain a good contact with the chill block during solidification. Approximately 20 seconds of zero gravity following by 20 seconds of 1.8 gravity were available during each cycle of KC-135 flight. Two set of samples were directionally solidified in low and high gravity periods.

In the second series of experiments(series B), two compositions, Al-41.0%Cu and Al-46.5%Cu ingots, were remelted in crucibles. The molten alloy was mixed mechanically by pouring the melt back and forth between the crucibles a total of six times. Immediately prior to pouring, the alloy melts were degassed by bubbling a dry

argon through them for one minute. After degassing, the melt (at 700°C) was poured into a preheated graphite crucible (also at 700°C) situated on a steel baseplate. Unidirectional solidification was accomplished by impinging water on the base-plate. A typical mould and chilling arrangement used for unidirectional solidification (series B) is shown in Figure (3-5). Before casting, the furnace was turned on and heated between 680°C to 700°C with the graphite crucible inside. When the crucible reached the desired temperature, it was filled with the alloy melt. Water coolant was turned on and the ingot solidified. With the top of the furnace insulated, heat removal (for solidification) happened through the bottom surface which results in a fully columnar structure.

In the third series of experiments (series C), the (28VDC) three zone gradient-freeze QUESTS furnace was used. The integrated GAS payload was designed by Queen's University and Bristol Aerospace to accommodate the gradient-freeze furnace and to carry out microgravity materials processing experiments[88]. This furnace can provide various cooling rates in different zones. A cross sectional view of the gradient furnace is shown in Figure (3-6). The gradient furnace has three individual Ni-Chrome windings along a ceramic winding former. To allow control of each of the windings, a thermocouple is located next to each winding on the inside of the former. To maximize the temperature gradients, the sample housings can be screwed directly into the heat sink as shown in Figure (3-7). The three-zone furnace was wired to three Omega programmable temperature controllers: Cn-2010 series. The purpose of these controllers is to raise, hold and lower the temperature in each of the zones. Each

controller runs on 120 VAC. The total amperage of the current drawn by the furnace is displayed in the ampere meter. In order to conduct ground based experiments with proper temperature recordings from the sample, a data acquisition system has been acquired and is being set up. The system includes a multifunction I/O board, analog input module and a type K, linealized thermocouple module. A Powerland 386 DX-40 computer, with monitor and printer, has also been acquired to store and display the data. Preliminary experiments were performed to optimize the system.

Alloys at compositions of 36, 38 and 40 wt% Cu were prepared and been charged into the graphite ampoule in the QUESTS sample housing of 6mm diameter and 89mm length. Unidirectional solidification of hyper-eutectic Al-Cu alloys was carried out on the ground both vertically and horizontally. The microgravity experiment was performed aboard the space shuttle Endeavour under controlled cooling rates and temperature gradients on Al-36Cu alloy. The cooling data was recorded automatically by the payload and displayed on the computer.

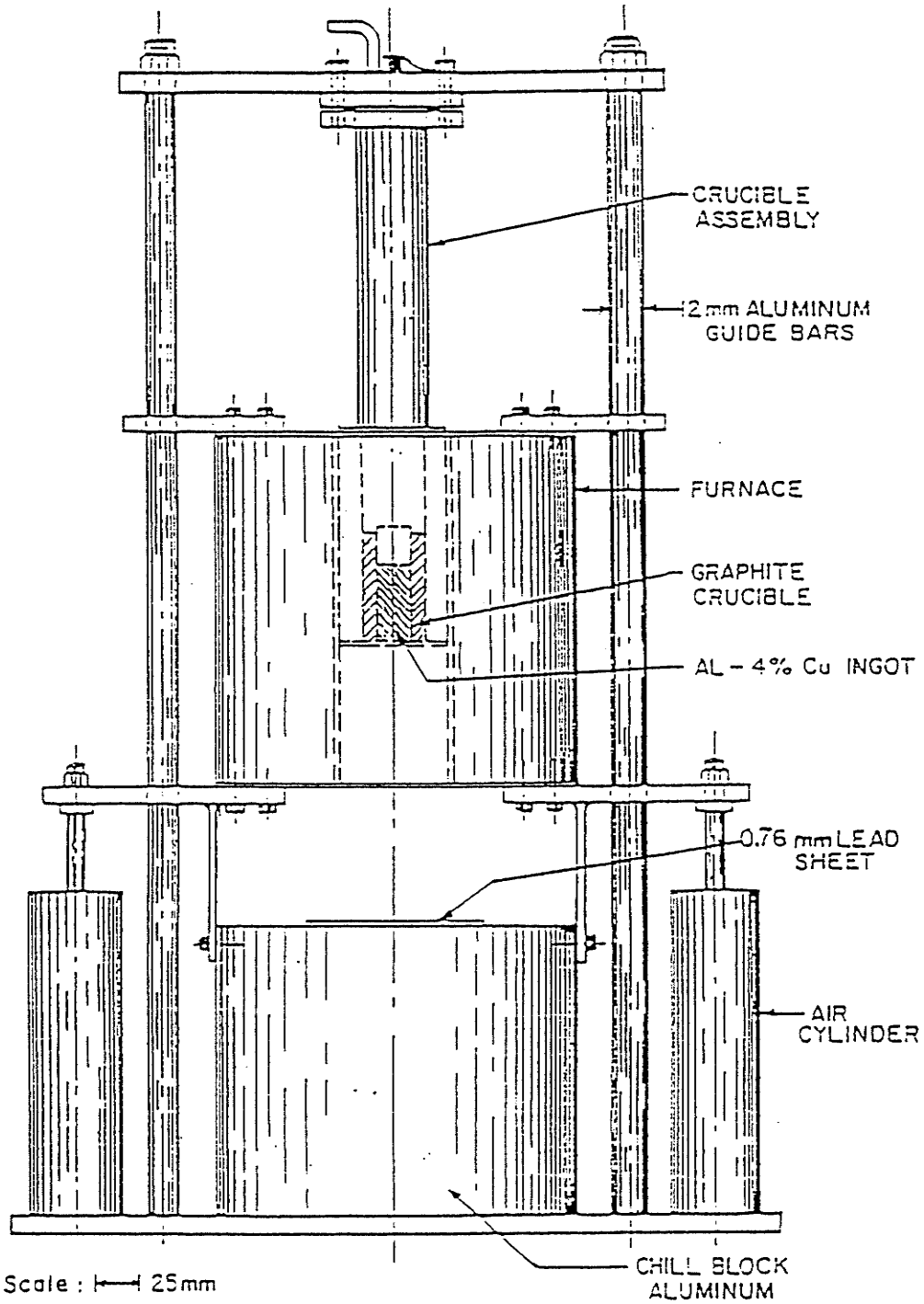


Figure 3.1

Schematic of the apparatus used in series A experiment[54].

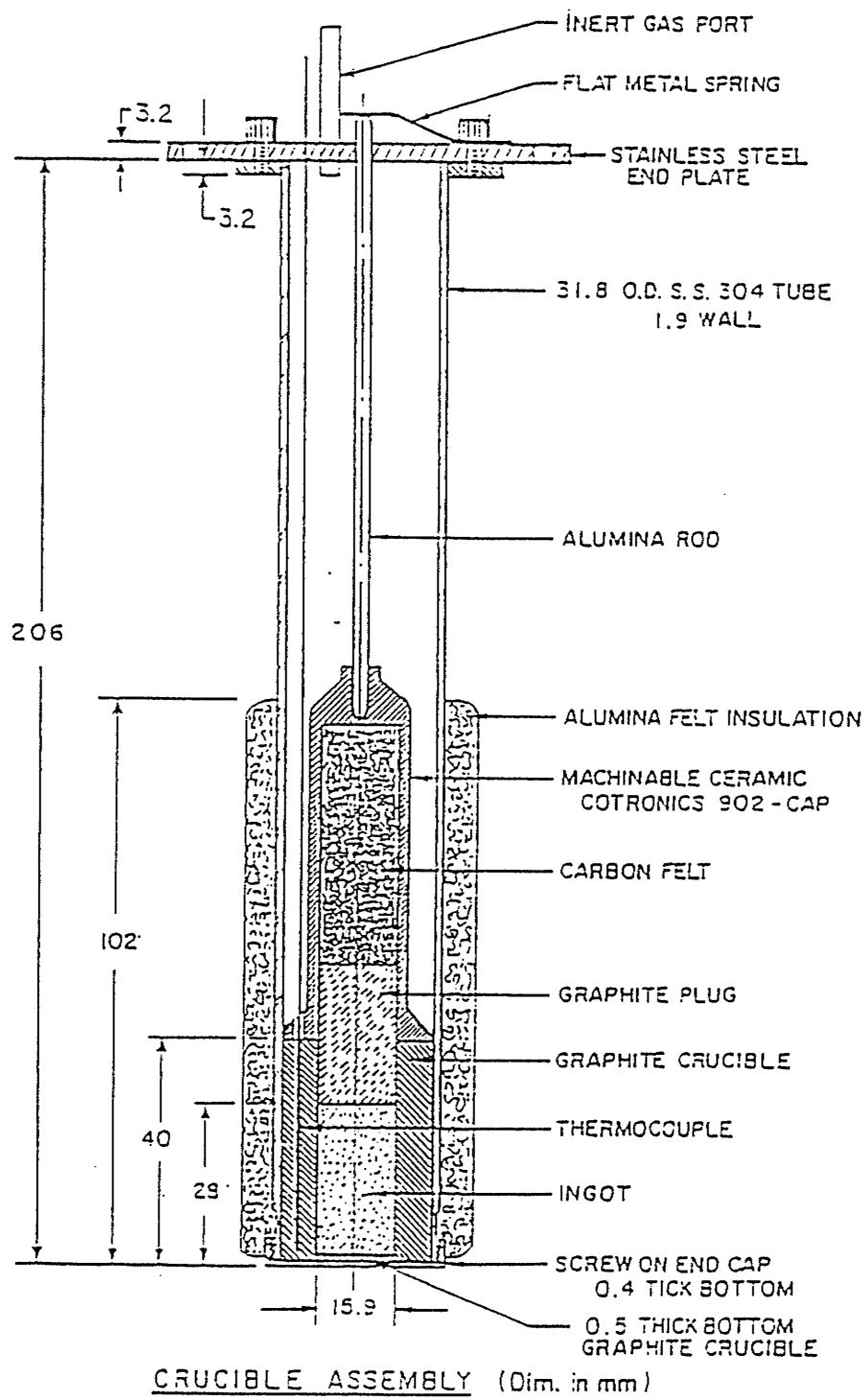


Figure 3.2

Crucible assembly in series A furnace[54].

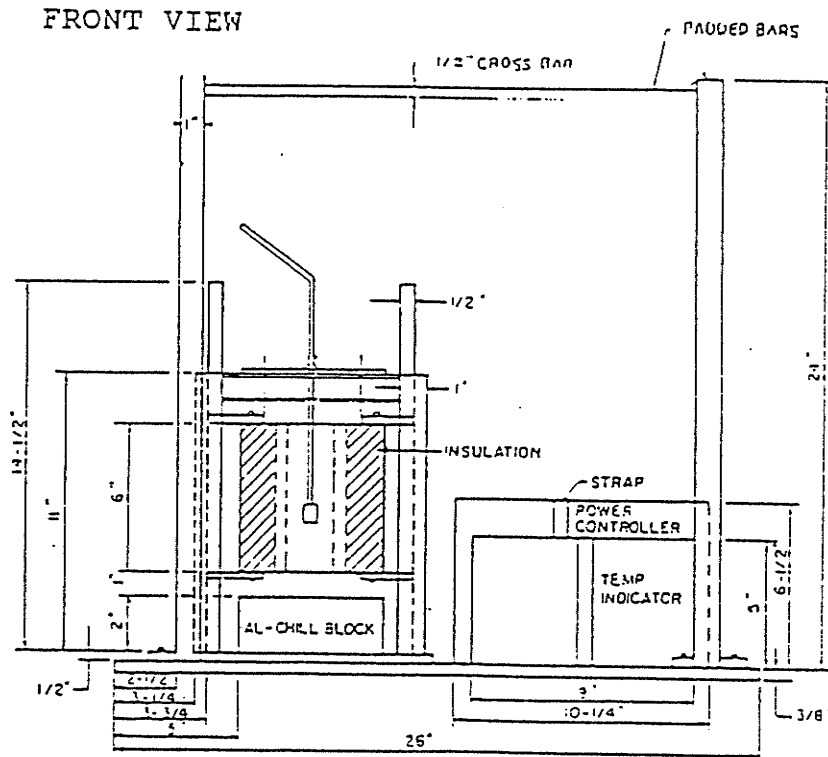
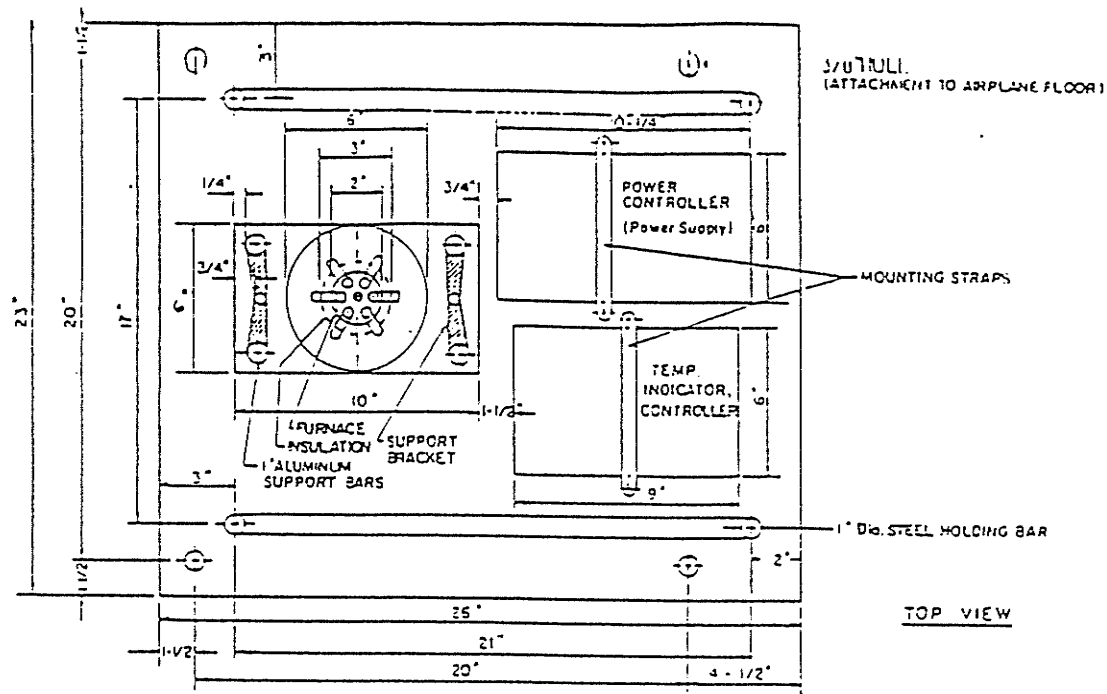


Figure 3.3

Front and top view of the test equipment used in KC-135 flight[54].

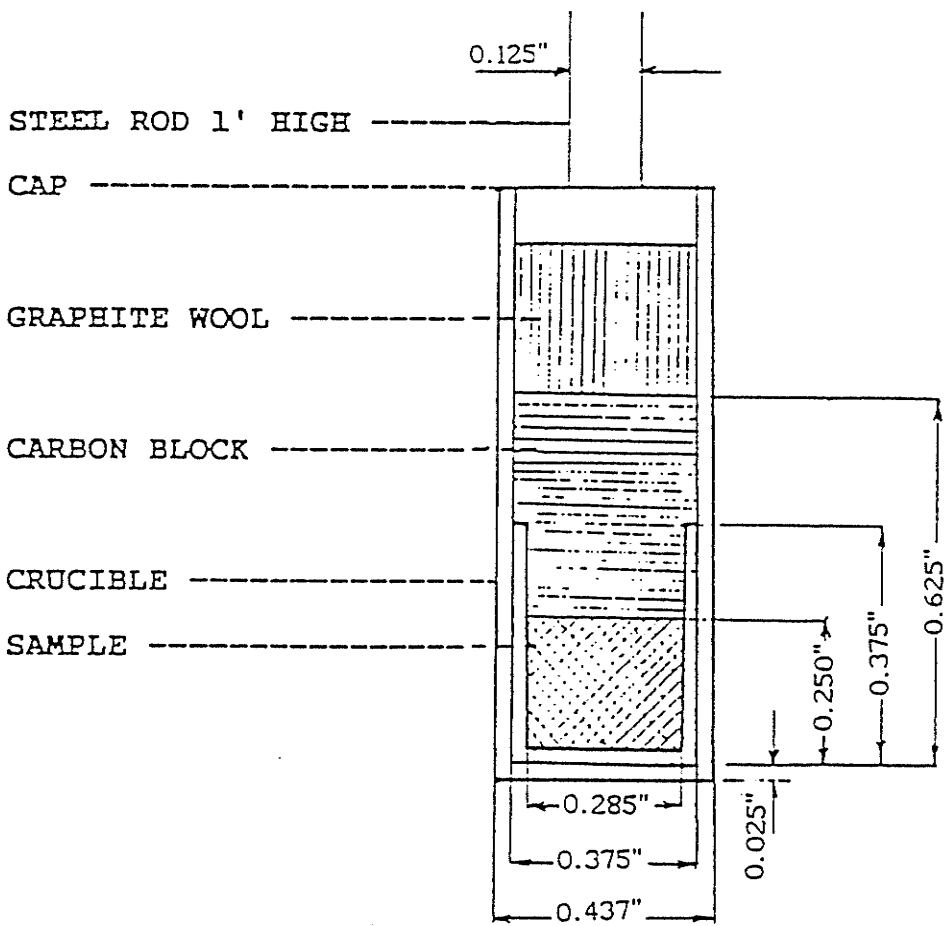
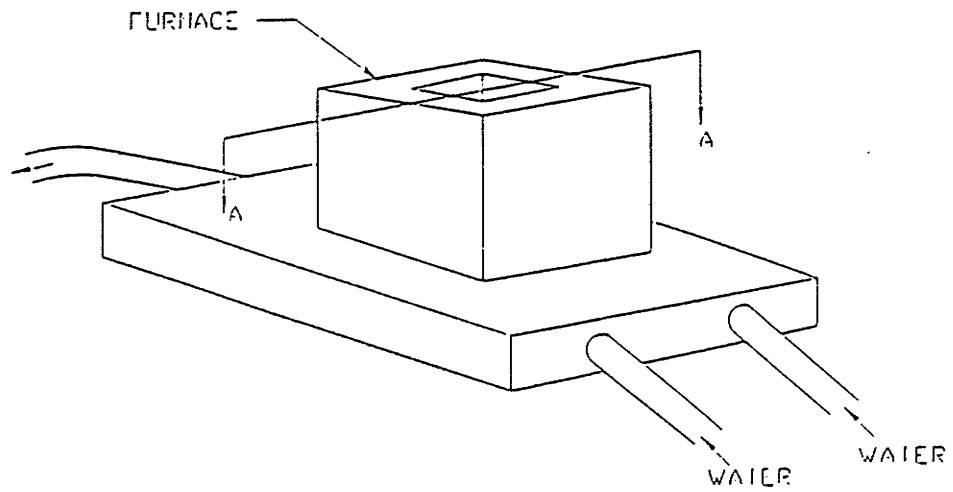


Figure 3.4

Crucible assembly for KC-135 samples[54].



SECTION A-A

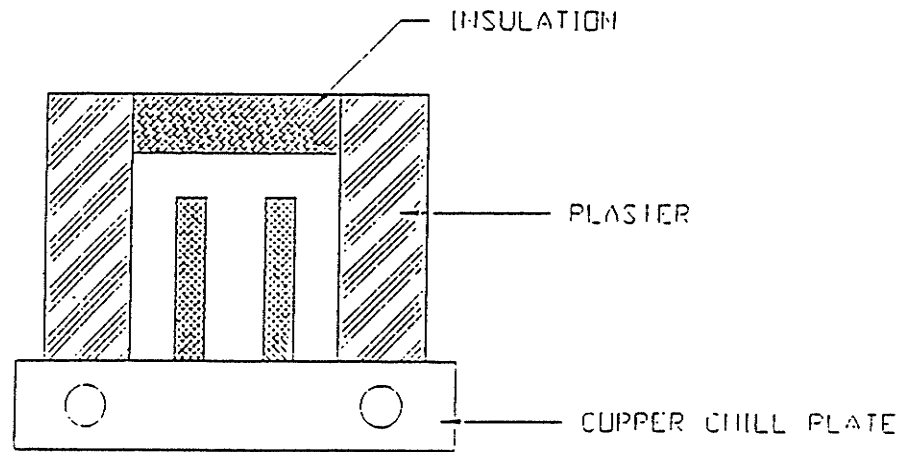


Figure 3.5

Typical mould and chill arrangement for unidirectional solidification(series B).

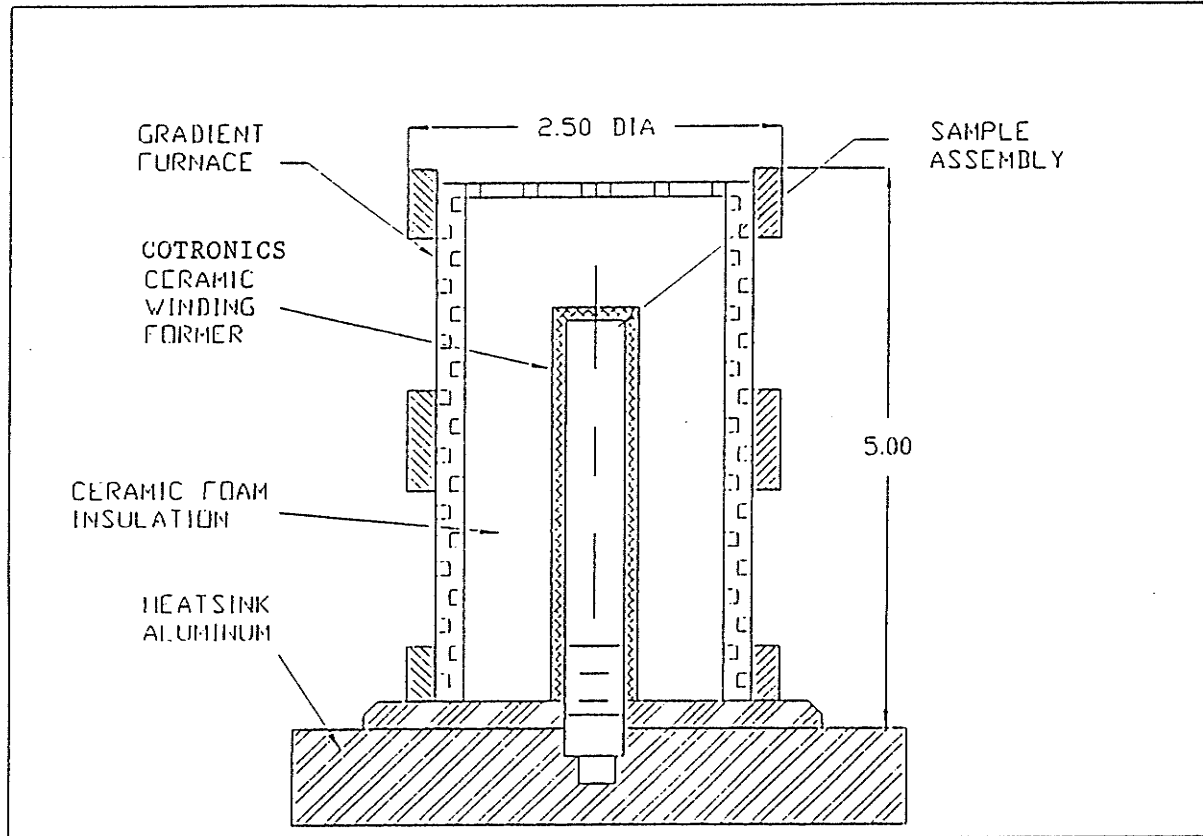


Figure 3.6

Cross section view of gradient QUESTS furnace[88].

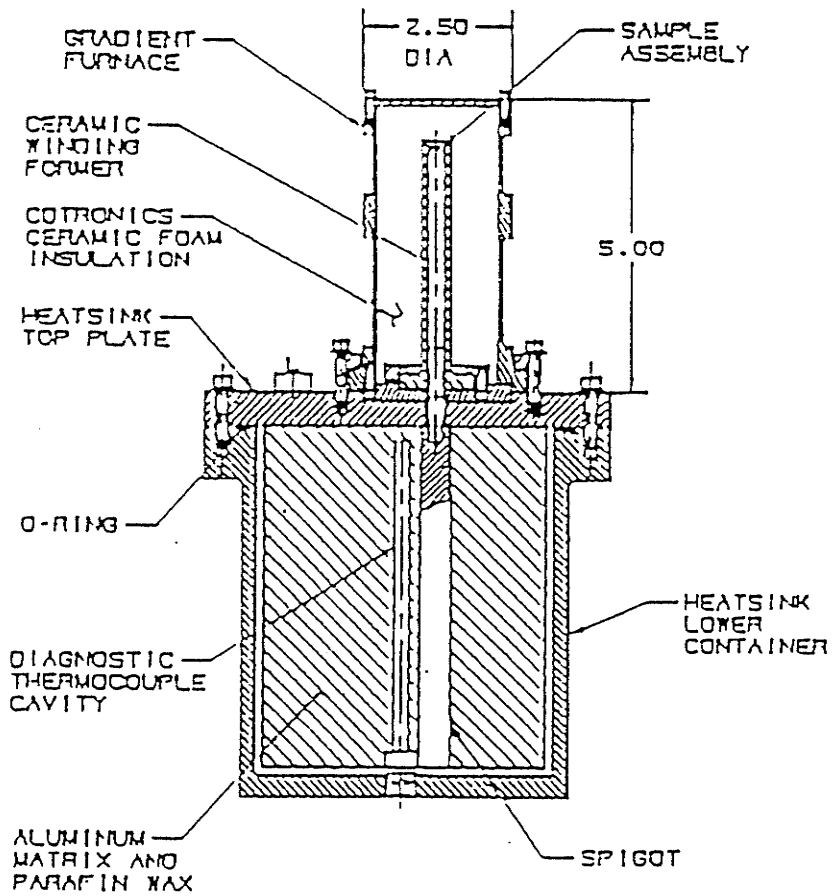


Figure 3.7

Cross section of gradient assembly[88].

Gradient assembly specifications: sample housing size(0.635cm dia, 8.90cm length); # of furnace heating zones (3); furnace max. sample temp.(1000°C); furnace max. case temp.(180°C)

3-3 MACRO- AND MICROSTRUCTURAL EXAMINATIONS

The specimens were sectioned longitudinally and transversely to provide examinations of the structure. All the samples were mounted in a resin, ground on 600 grade SiC paper, followed by an intermediate polishing with a diamond pasta of 6 μm , 1 μm and a final polishing with a slurry of water and colloidal silica of less than 0.05 μm . Samples were etched finally by immersing them for 10 to 15 seconds in a diluted (1 to 1) Keller's reagent (950 ml H₂O + 35 ml HCl + 15 ml HF), and dried by rinsing with ethanol.

The macrostructure was examined directly by eye as well as under a NIKON optical microscope. The microstructural examinations of the samples were performed under a NIKON optical microscope as well as in a JEOL JXA-840 scanning electron microscope.

3-4 MACROSEGREGATION ANALYSIS

Macrosegregation of a solute element (Cu weight percentage) was determined as a function of the distance from the chill face or solidification bottom by using the EDS technique in a JEOL JXA-840 scanning microanalysis. Longitudinal cross sections of all of the samples were polished (without etching) and subjected to an EDS analysis by exposing an appropriate area according to the sample size on the disc. All the analyses were performed at 15KV with a constant probe current of 600PA. A machine dead time of approximately 25% and the acquisition time was 120 seconds were maintained. Each area was analyzed three times and the results were averaged.

The accuracy of the measurement is given by the difference between the largest and the lowest value for a given area.

3-5 MEASUREMENT OF SPACINGS

In the case of the solidification of a dendritic array, the main geometrical characteristic is the primary interdendritic spacing λ . For series A and B samples, the primary spacings were measured directly from the longitudinal sections of the samples by using a JEOL JXA-840, scanning electron microscope. Measurements were obtained by counting the number of the aligned primary θ phase intersected with the perpendicular 10mm line at locations 4mm, 12mm, 14mm from the chill. For each sample, the primary spacings are measured in the central part of the dendritic portion, all the aligned primary θ phases were included in the counting and the results were averaged.

For series C sample, the primary spacings have been measured by hand as well as on an Image Analyzer, by determining the number of primary dendritic arms N within a surface A of a transverse section. Four transverse sections at locations 23mm, 26mm, 47mm and 50mm from the solidification beginning have been prepared. The primary spacing λ_i is defined by

$$\lambda_i = B (A/N)^{1/2} \quad (3-1)$$

where B is a constant which depends on the geometry of the network (B equals 1,

1.075 and 0.5 for a square, hexagonal and random array, respectively). For hypereutectic Al-Cu samples, square network is generally observed, B is taken as 1. Only grains where the axis of primary arms are near to the solidification direction are considered.

The accuracy of the measurement is given by reporting the lowest and the largest λ_1 value for a given micrography, which depends on the particular morphology encountered. The more uniform size and distribution of the primary dendrite trunks are, the more accurate the result will be.

Image analysis is used in order to identify and reconstruct convex elements corresponding to primary dendritic trunks. Figure (4-10) shows the microstructure of the transverse section of the sample. Little dendrites nucleated during the solidification can be noticed. The true primary dendrite trunks are those with perimeters larger than 0.15mm. Automatic cutting by morphological openings is needed to reconstitute separated primary trunks. The primary trunks at the edge of the mask have to be counted as a partially primary whose size depends on the ratio of the area inside the mask to the total size of the trunk. Primary spacings measured in this way at the locations lower than 48mm from the solidification bottom are in good agreement with those measured from the longitudinal section of the sample. For the top part of the sample, the primary trunks are much smaller than the one close to the bottom. The true primary trunks are those with perimeters larger than 0.10mm. Automatic cutting has also been performed to reconstitute separate primary trunks.

The lamellar spacing of eutectic Al-Al₂Cu is also measured by Image Analyzer.

The measurement was carried out by use 50 lines cut through the sample horizontally, vertically as well as at 45° and at 135° across the section. The intersect spacings have been measured by thinning of grain boundaries. The lamellar spacing is taken as the sum of the intersect spacings for two phases. The accuracy of the measurement is given by the lowest and the largest λ_{eu} value for a given section of the sample.

Measurement for volume fraction of θ phase has also been carried out on Image Analyzer. The area of the θ phase as well as the total mask area were measured and the ratio of which has been taken as volume fraction of θ phase. The accuracy of the measurement is given by reporting the lowest and the largest V_{θ} value for a given section of the sample.

3-6 MICROGRAVITY SAMPLES

In this research, the same equipment as series A has been carried on the NASA KC-135 flight. Each low-g manoeuvre gives from 20 to 30 seconds of $10^{-2}g$, and up to 1.5 minutes of pullout and climb up to 1.8g. The very small sample with 6 mm diameter and 5 mm length of Al-38%Cu, Al-43%Cu and Al-48.0%Cu has been used.

The top and front view of the test equipment and the crucible assembly are shown in Figures (3-6) and (3-7). The samples were placed inside a graphite crucible in the stainless steel container. The same system of carbon block and graphite wool was used to prevent the melt from floating away from the crucible during zone gravity and also to apply pressure to the fluid melt and attain a good contact with the chill block during solidification.

Approximately 20 seconds of zero gravity followed by 40 seconds of 1.8 gravity were available during each cycle of a KC-135 flight. Two sets of samples were solidified directionally in zero and two gravity periods.

Longitudinal and transverse sections of ingots were cut out and prepared for microstructure examination as well as macrosegregation analyses. Starting from the chill face and proceeding to the other end, an area of 5 mm X 0.5 mm was exposed on a disc using a EDS technique. The other conditions for the analysis were the same as the ones used for the large ground-based samples. Primary θ phase spacings were also counted from the longitudinal sections of the sample.

Inorder to perform slow solidification in microgravity environment, the QUESTS gradient freeze furnace has been carried on flight shuttle STS-47 Endeavor to perform the unidirectional solidification in microgravity environment. Alloy of Al-38%Cu was used. The experimental set up is the same as the one used on ground in series C experiment. Longitudinal sections of the samples were sectioned and polished for microstructure and macrosegregation analyses. Primary arm spacing were measured from the transverse sections of the sample.

CHAPTER IV

EXPERIMENTAL RESULTS AND DISCUSSION

4-1 COOLING CHARACTERISTIC

The temperatures of the melt in series A of experiments were measured during solidification by using two thermocouples located at heights of 7 mm and 13 mm from the chill face in the graphite crucible. Cooling curves of the ingots are shown in Figures(4-1) (a) and (4-2) (b) for the Al-38%Cu and Al-50%Cu samples. All the ingots were superheated to 700°C and cooling occurred with a nearly steady state in the melt. The cooling rate near the chill face was found to be higher than that near the top. Table(4-1) lists the average cooling rates, temperature gradients and growth velocities which were calculated from the cooling curves for the two samples. The total solidification time was around 60 seconds.

The thermal data for series B was obtained by using the experimental procedure of Kato and Cahoon[47]. It is shown in Table(4-2).

The temperature recording from series C, which employed the three zone gradient-freeze QUESTS furnace, is shown in Figure(4-2). The average cooling rates, temperature gradients and growth velocities, which were calculated from the recorded cooling curve, are listed in Table(4-3). The total solidification time was 72 minutes for faster solidification($R \sim 1.5 \times 10^{-2}$ mm/s) and 110 minutes for the rest samples($R \sim 7.4 \times 10^{-3}$ mm/s).

Table 4-1 Cooling Characteristics of Series A Samples

Sample	Average Cooling Rate K/s ($\delta T/\delta t$)	Average Temp. Gradient G, K/mm($\delta T/\delta X$)	Average Grow. Velocity R, mm/s
Al-50%Cu	0.50	3.6	0.14
Al-38%Cu	0.98	2.2	0.33

Table 4-2 Cooling Characteristics of Series B Samples [47]

Distance from Chill	Cool. Rate at Liqui. Temp. (K/s)	Tem. Grad. at Liqui. (K/mm)	Solid. Rate (mm/s)	Local Solid.Time (s)
10	8.35	3.75	1.00	53
35	1.42	1.40	0.59	144

Table 4-3 Cooling Characteristics of Series C Samples

Sample	Average Cooling	Average Temp.	Average Growth
	Rate K /s($\delta T/\delta t$)	Gradient G,K/mm ($\delta T/\delta X$)	Velocity R, mm/s
Al-38Cu V	Top: 0.061	3.1	0.019
	Middle: 0.053	3.2	0.013
	Bottom: 0.044		
Al-36Cu V	Top: 0.037	5.1	0.0077
Al-40Cu H	Middle: 0.038	5.0	0.0075
Al-38Cu S	Bottom: 0.037		

(The average data was taken as an average over the 4 points on the cooling curve as seen in Figure 4-2. H and V indicate horizontal and vertical solidification, respectively. S represent space sample.)

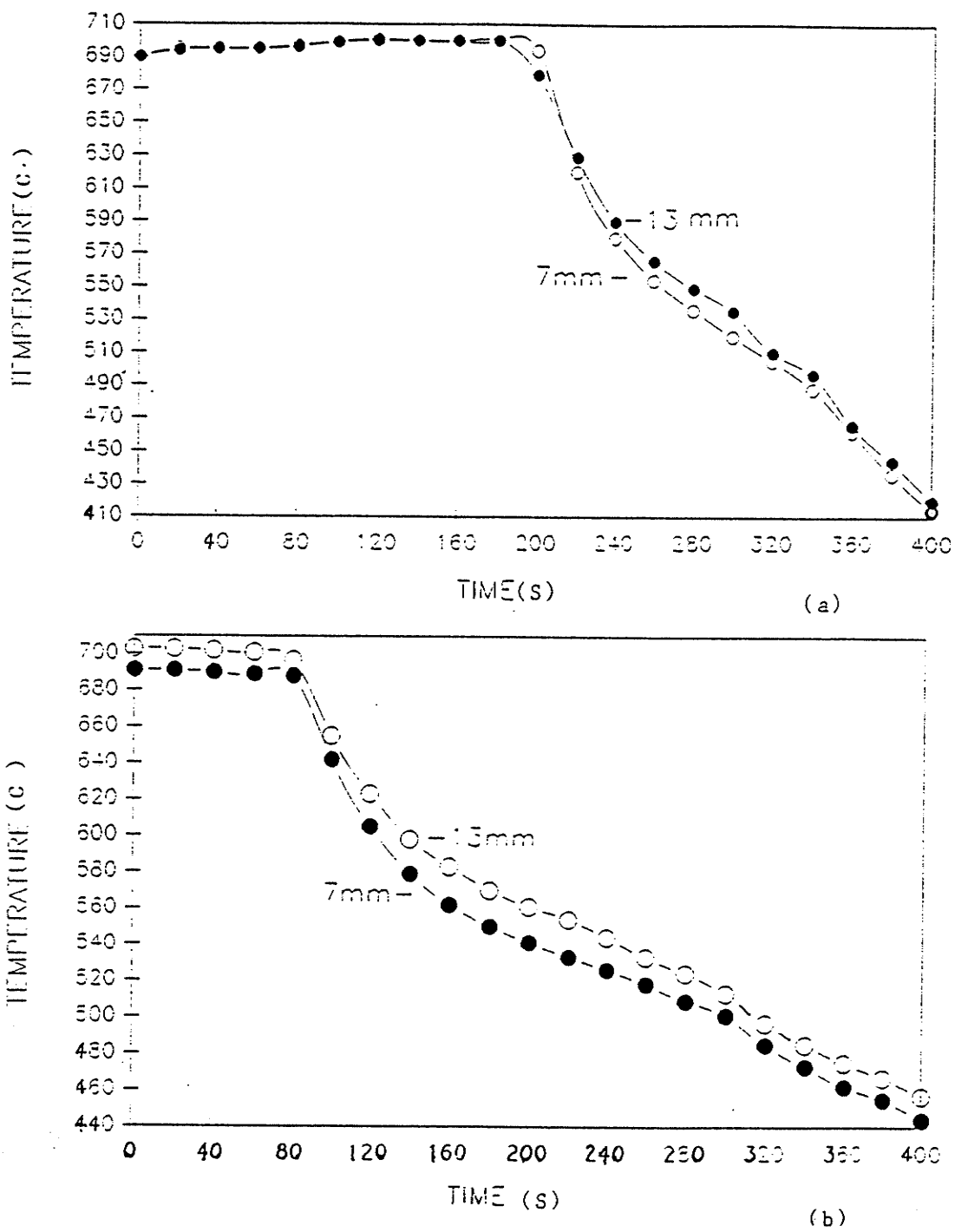
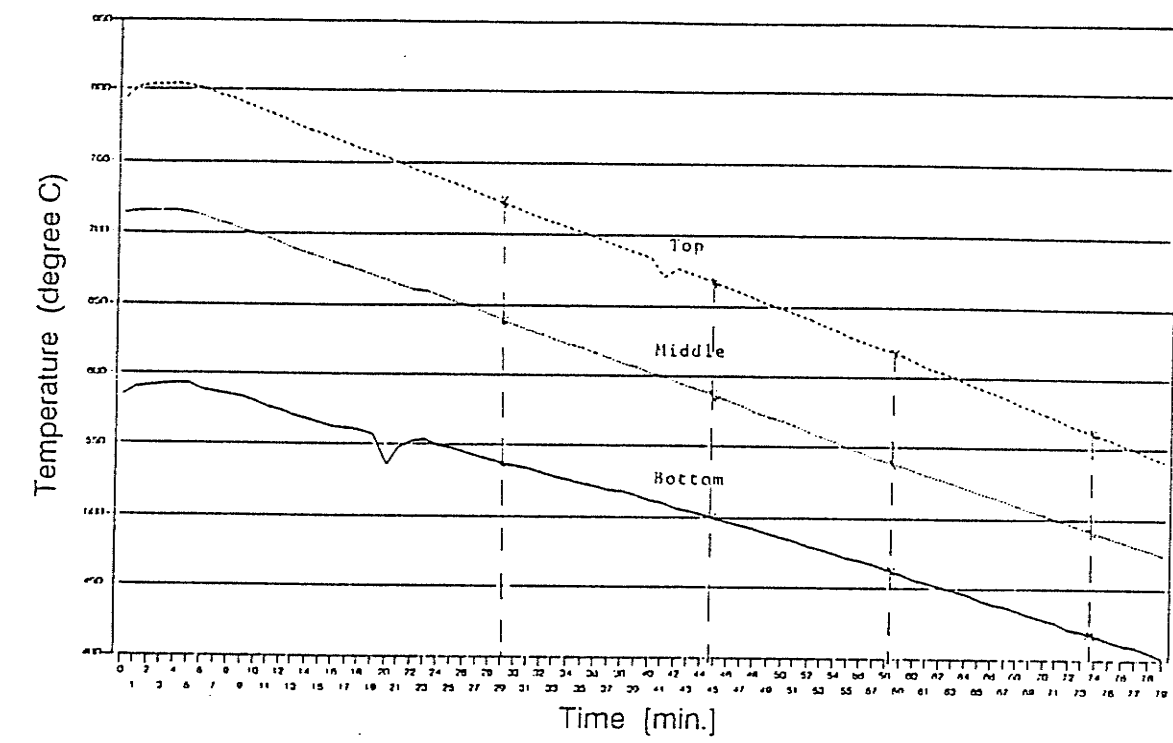


Figure 4.1

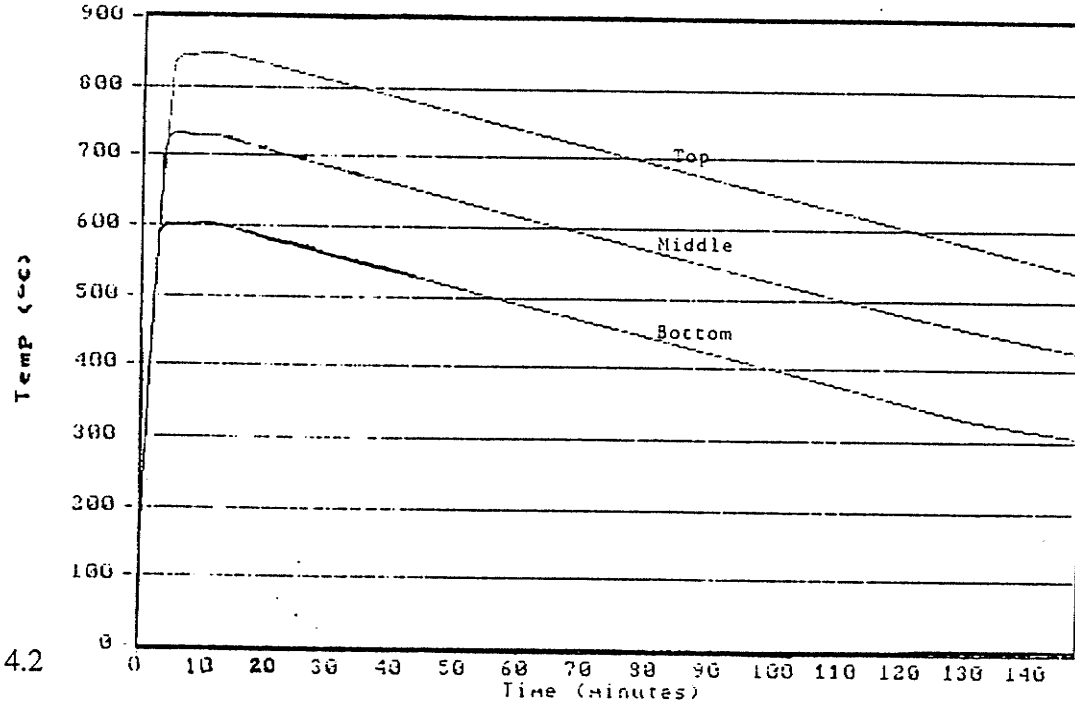
Cooling curves for series A samples.

(a) Al-38Cu

(b) Al-50Cu



(a)



(b)

Figure 4.2

Cooling curves for QUESTS samples.

(a) Al-38Cu on ground(↑)

(b) Al-35Cu on ground(↑)

* ↑ indicates the solidification direction.

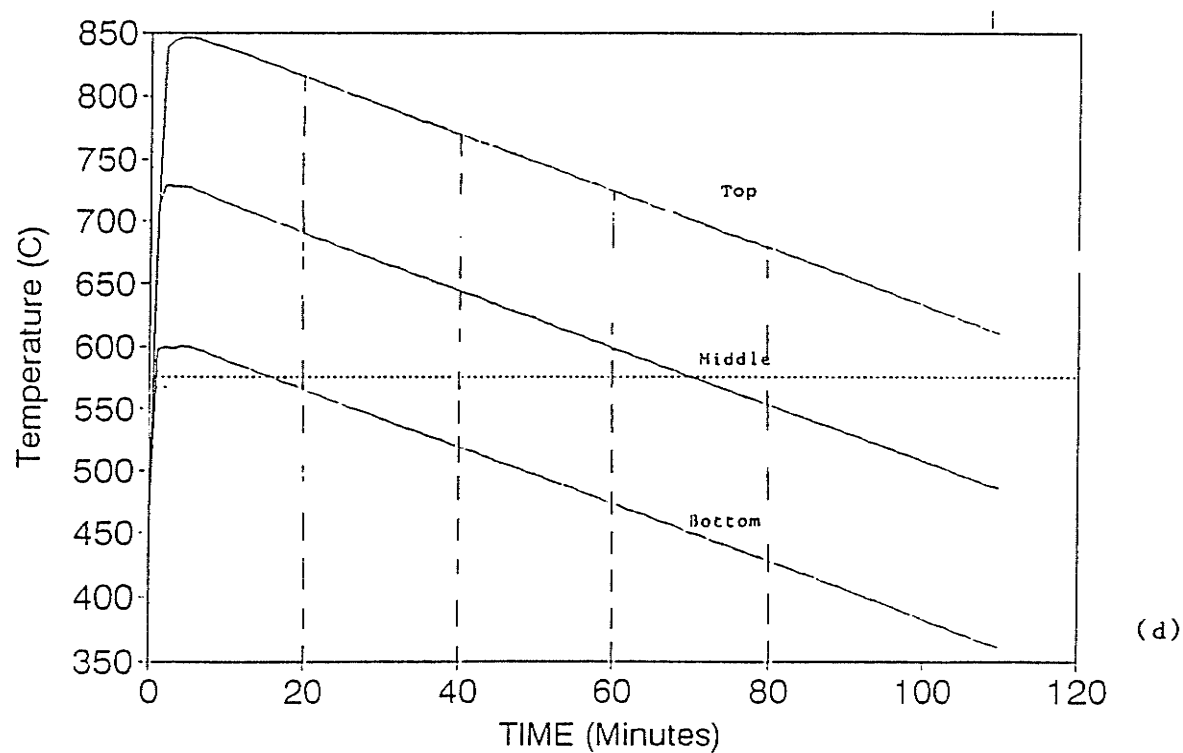
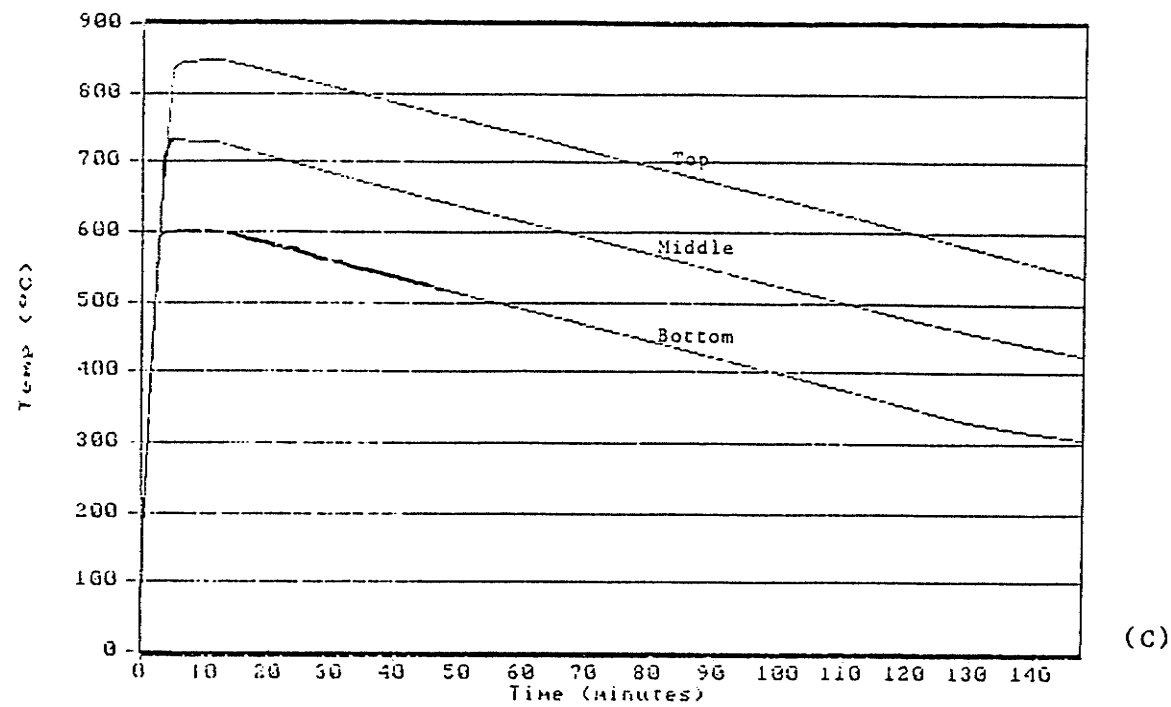


Figure 4.2 continued

(c) Al-40Cu on ground(←)

(d) Al-38Cu microgravity

4-2 MACROSTRUCTURE OF THE SPECIMENS

Longitudinal sections of the samples were examined to review the unidirectional solidification. The development of the Al_2Cu primaries was observed from the very beginning of solidification along the growth direction in the longitudinal section. Figure (4-3) illustrates the longitudinal section of eight alloys from three series of experiments. The microstructure examination of hypereutectic Al-Cu alloys showed primary particles of θ phase in a eutectic matrix. Most of the θ phase has been aligned in a certain direction caused by the unidirectional solidification process, in which the direction of the thermal gradient is controlled and normally parallel to the growth direction of the growing phase.

It is obvious that the primary θ phase is bigger and better aligned in the ingot from the three zone gradient-freeze QUESTS furnace (series C). Because both the cooling rate and thermal gradient can be controlled closely, the QUESTS three zone furnace also produced a planar isotherm at the position of the interface. Therefore, the QUESTS furnace provides a better potential for a unidirectional solidification experiment.

Compare Figure(4-3) (e) with (f), significant difference has been observed at the top of the samples. In the space sample primary θ phase present along the whole length of the ingot. However, in the ground based sample, only eutectic occurs at the top. No θ phase has been observed at the solidification top. This phenomenon is due to gravity caused sedimentation, as we will discuss later[4-3].

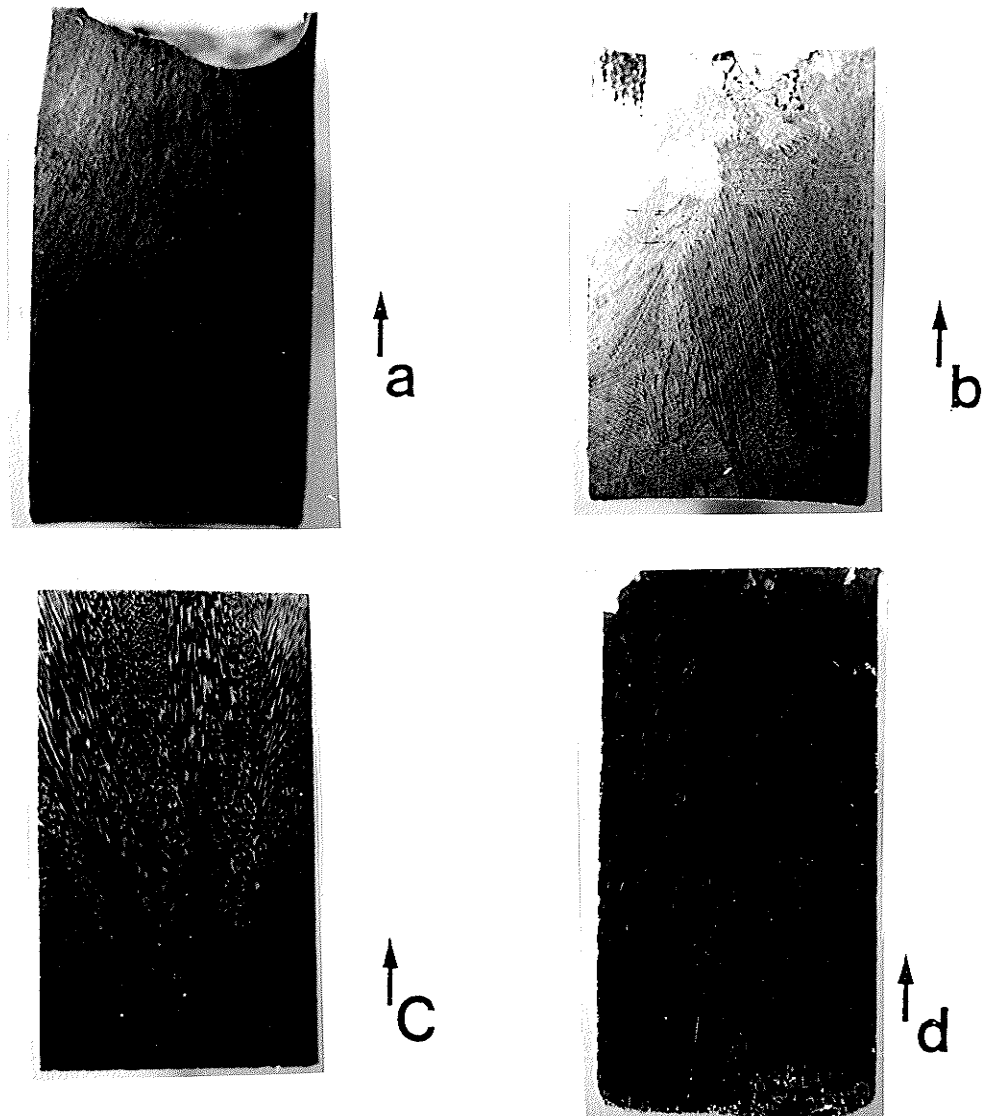


Figure 4.3

Longitudinal cross section of ingots.

- (a) AL-38Cu (series A ↑)
- (b) Al-50Cu (series A ↑)
- (c) Al-41Cu (series B ↑)
- (d) Al-47Cu (series B ↑)

* ↑ indicates the solidification direction.

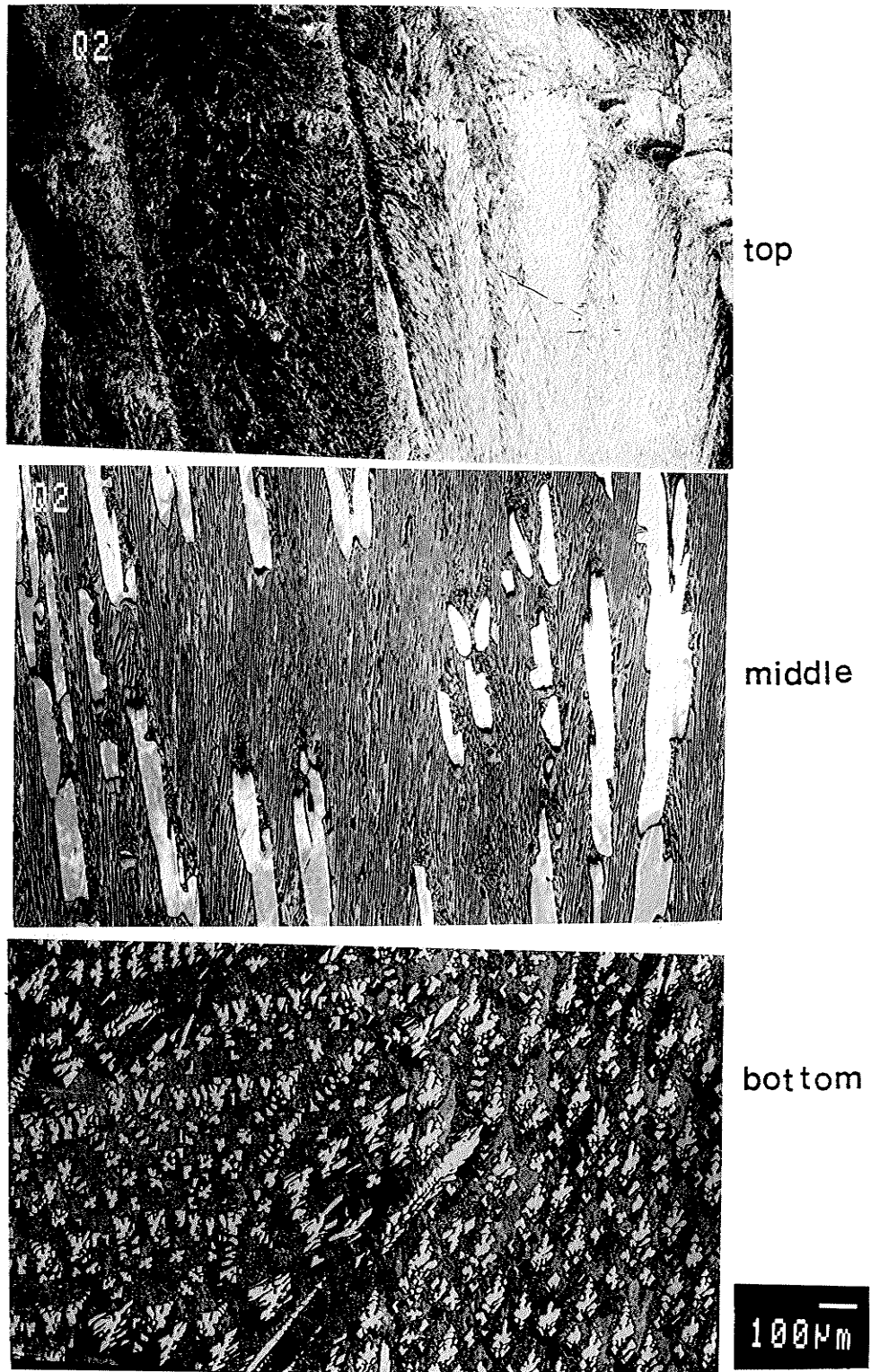


Figure 4.3 continued

(e) Al-38Cu QUESTS on ground (\uparrow) sample(52X).

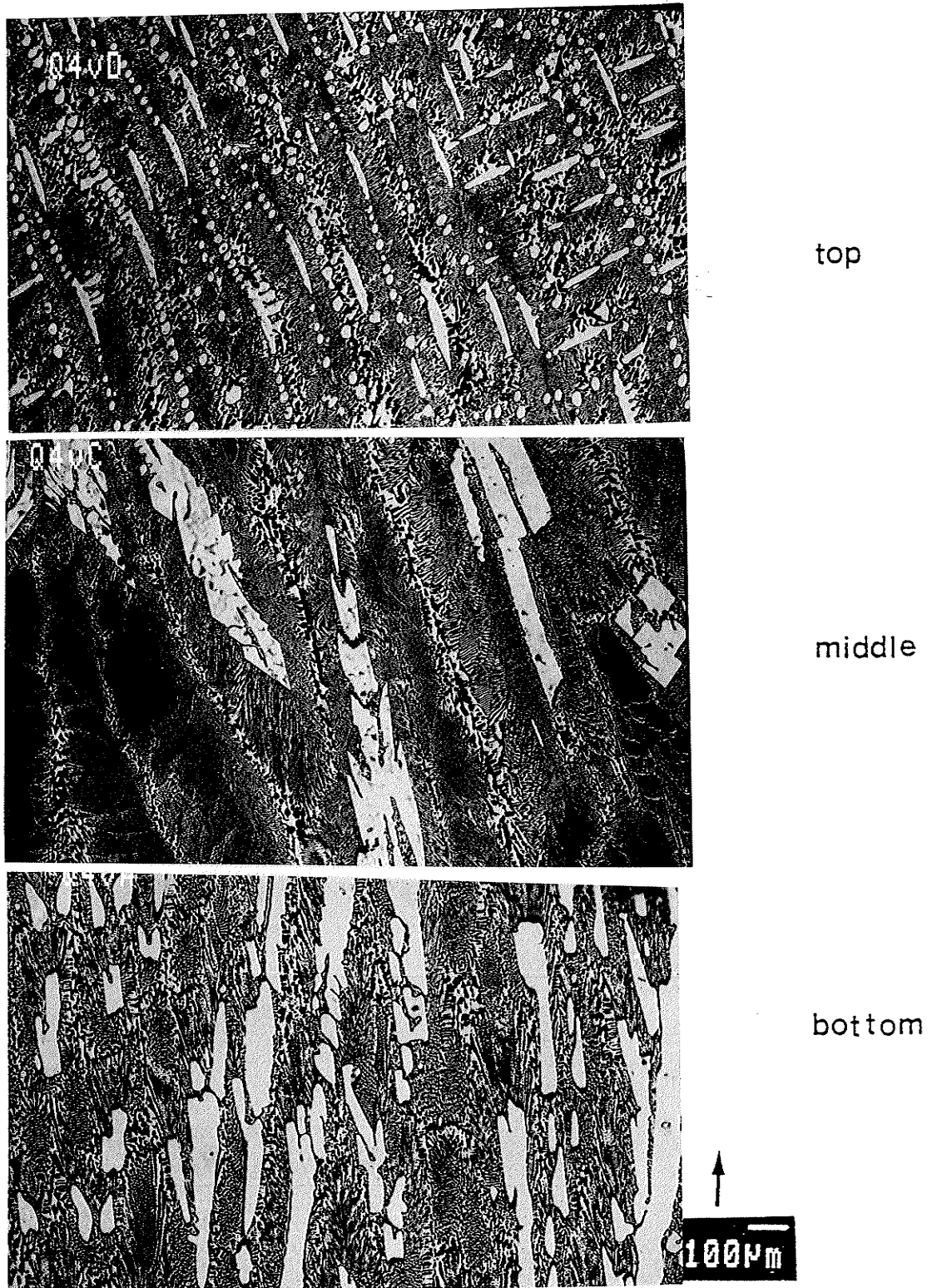


Figure 4.3 continued

(f) AL-36Cu QUESTS on ground (\uparrow) sample(52X).

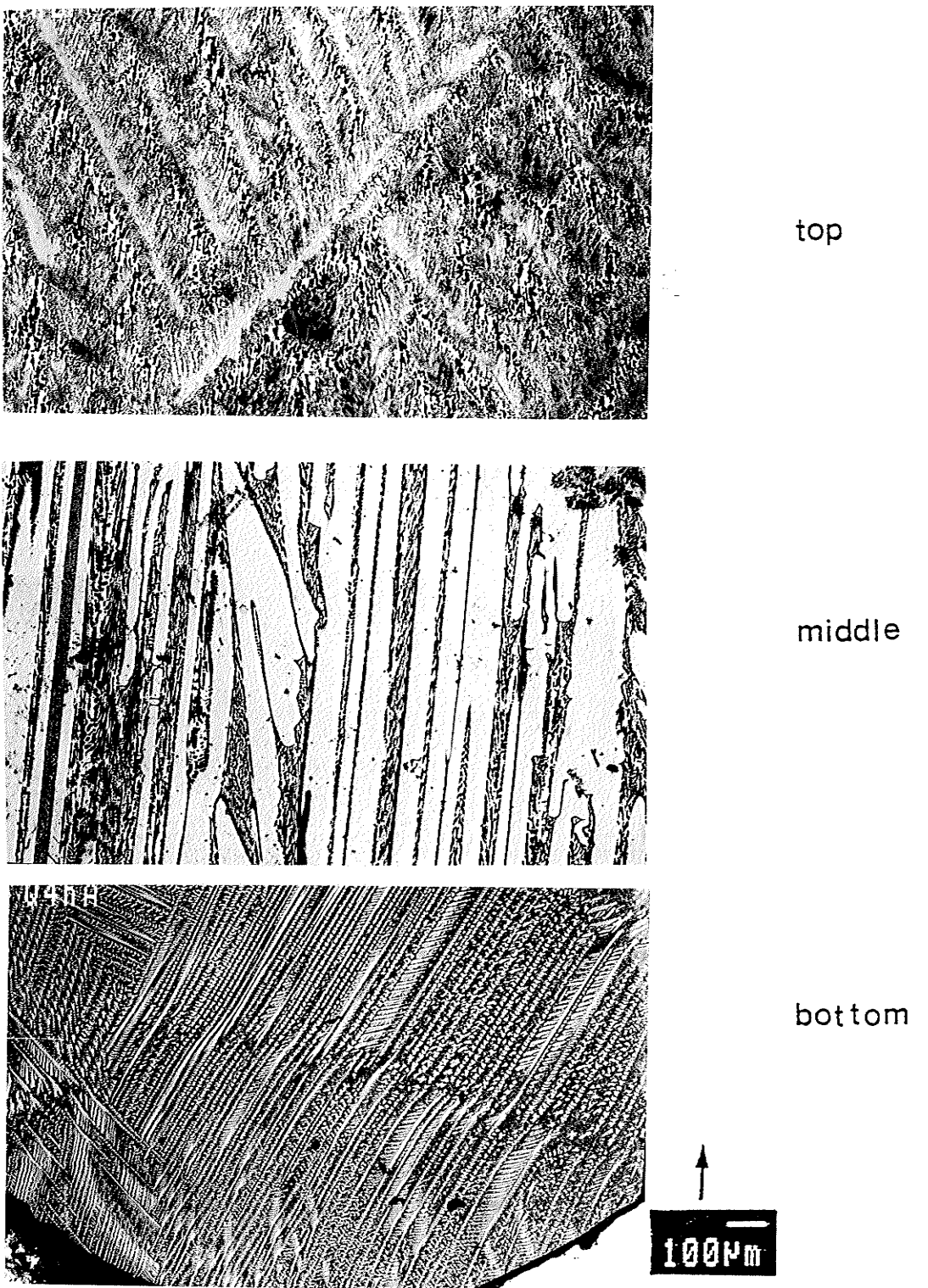
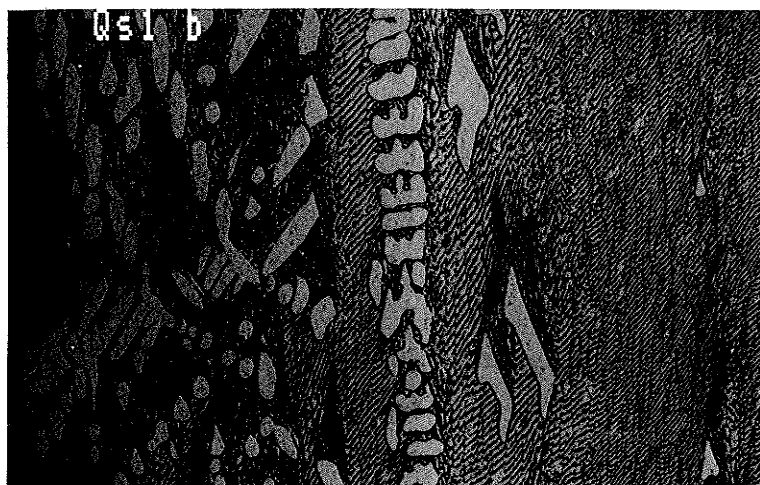


Figure 4.3 continued

(g) Al-40Cu QUESTS on ground (↔) sample(52X).



top



middle



bottom

Figure 4.3 continued

(h) Al-38Cu QUESTS space sample(52X).

4-3 MICROSTRUCTURE OF HYPEREUTECTIC AL-CU ALLOYS

Over the composition range studied, the microstructure of the hypereutectic Al-Cu alloys consisted of primary θ phase (Al_2Cu) and a lamellar eutectic of Al-Al₂Cu as shown in Figure (4-4). All the pictures were taken in a scanning electron microscope by using backscattered electron signals. An irregular eutectic growth has been noticed because the growth direction of the faceted phase is determined by specific atomic orientations and is not necessarily parallel to the heat flux. It was clear, from Figures(4-5) through (4-9), that, as the solidification progressed along the length of the samples, the primaries gradually developed directionality. The preferential growth direction of the Al_2Cu crystal was determined by growing a single crystal of Al_2Cu from its own melt, without using a seed[7]. The single crystal grew in the [001] crystallographic orientation.

The morphology of the Al_2Cu primaries showed a gradual transition from non-faceted to faceted crystals with increasing Cu concentrate in the melt. From the samples of series A, at 35% Cu composition, solidification started with the formation of Al_2Cu dendrites. Some of the Al_2Cu phase was disconnected from each other and became round or slightly faceted particles aligned along the growth direction. As the solidification progressed further, the primaries became coarser but still grew in a dendritic manner. Figure(4-5) shows the dendritic growth morphology of the primaries along the solidification direction in an alloy of 35%Cu.

In the alloy of 38%Cu grown from a fully liquid state, solidification began with

the Al_2Cu dendrites, as shown in Figure(4-6). The appearance of Al_2Cu at the chill has no side branches. As the solidification progressed further, the rounded Al_2Cu trunk gradually developed discrete facets as indicated in Figure(4-6) (a).

As the Cu concentration of the melt approached 50% Cu, the tendency of the primaries to form facets increased too. Solidification started with heavily faceted primaries which adopted a rectangular prismatic shape as seen in Figure(4-7) (b). The tendency for faceting was found to decrease as the solidification progressed further. An elongated chunky primary Al_2Cu phase was noticed without dendritic arms .

From the above discussion, it can be concluded that the faceting tendency of Al_2Cu primaries increases with increasing Cu content of the initial alloy composition. The effect of the solute concentration in the variation of atomic roughness and solid/liquid interfacial energy was studied by Camel[80]. Camel suggested that the faceting tendency increased if the A-B interaction is repulsive and reduced for an attractive interaction in systems with negative or zero adsorption of the B component. Since Al_2Cu forms an intermetallic compound, the interaction between Al and Cu atoms is attractive and yet faceting occurs.

For a 38% Cu composition alloy (series A), the initially solidified part of a sample consisted of rounded primaries which gradually became fully faceted further along the sample as freezing progressed. (see Figure 4-6). Moreover, the size of the primaries was much smaller at the chill. The relatively fine microstructure of the primaries, which was formed at the very beginning, was due to nucleation from an undercooled melt. Undercooling caused the primaries to nucleate with a random

orientation.

In terms of the effect of the cooling rate, the 38%Cu sample was solidified at 1.00mm/s in the series B experiment. The Al_2Cu primaries developed a fully dendritic structure at the beginning of solidification and became partially faceted at the top (Figure 4-8). It is clear from Figure(4-6), that the same alloy becomes partially rounded at the bottom and fully faceted at the top when solidified at 0.33mm/s. The 40% Cu samples were also solidified by air cooling and furnace cooling, respectively. A greater tendency of faceting Al_2Cu primaries was observed with an decreasing cooling rate. Figure(4-9) shows that in an air cooled sample, faceted Al_2Cu primary with developed side branches at the corners are observed. While in the furnace cooled sample, the θ phase is fully faceted with elongated chunky structure .

Faceted morphologies occurred in high-entropy phases and they were a consequence of anisotropic growth. The solid/liquid interface of a high-entropy phase was smooth at the atomic scale. In dendritic growth, both the interface kinetics and surface tension were assumed to be isotropic and their contribution to shape stability was considered insignificant[7]. While dendrite growth was mainly a diffusion-controlled process, in which heat and solute diffusion were predominant, a large kinetic barrier was associated with the attachment of atoms from the liquid to the solid growth. As result, the growth became restricted to lateral movement steps. A faceted morphology was a manifestation, therefore, of slowly growing planes. Undercooling associated with the movement of the interface might affect the lateral growth behaviour, by favouring the random deposition of atoms on the transition from a

smooth to a rough interface. As in the case of series B experiments where the growth rate was increased deliberately, side branches developed readily as shown in Figure (4-8). The difference between the morphology of the primaries, observed in the two different solidification modes, indicated that the growth rate associated with large undercooling decreased the shape stability of the Al_2Cu primaries. The growth of Al_2Cu primaries is diffusion-controlled and, therefore, the instability of the interface is promoted by the dilution of the melt.

The solidification of hypereutectic Al-Cu alloys were also carried out under microgravity, where the gravity induced convection is eliminated. Figure(4-17) (a) and (b) shows the microstructure of Al-36Cu samples aboard KC-135 flight and solidified under 0G and 1.8G respectively. The dendritic structure with developed side arms of primary θ phase was observed in microgravity sample(Fig. 4-17a), whereas the rounded primary particles with smoother surface were observed in 1.8G sample(Fig. 4-17b).

In series C experiment, hypereutectic Al-Cu alloys were slowly solidified under controlled cooling conditions. Diffusion and convection played an important role in the solidification process. Compare the space sample with those obtained under terrestrial conditions, it is observed that the morphology of the primary θ phase was strongly influenced by lack of convection. Larger, tree-like primary dendrites of θ phase were present in the space sample, whereas smaller particles with discrete facets were observed in the ground based sample (Figure 4-10). Also, the θ phase particles in the ground based sample have smoother surfaces compare with the dendrite arms in space

sample. It is concluded[5-2] that the presence of convective mixing in the ground based sample promoted the faceted θ phase morphology and retarded the dendritic growth. The physically moving of the nucleation sites due to the natural convection may provide more nuclei for the growth of more θ phase. Therefore, the ground based sample will exhibit more but smaller and smoother θ phase particles than the space sample.

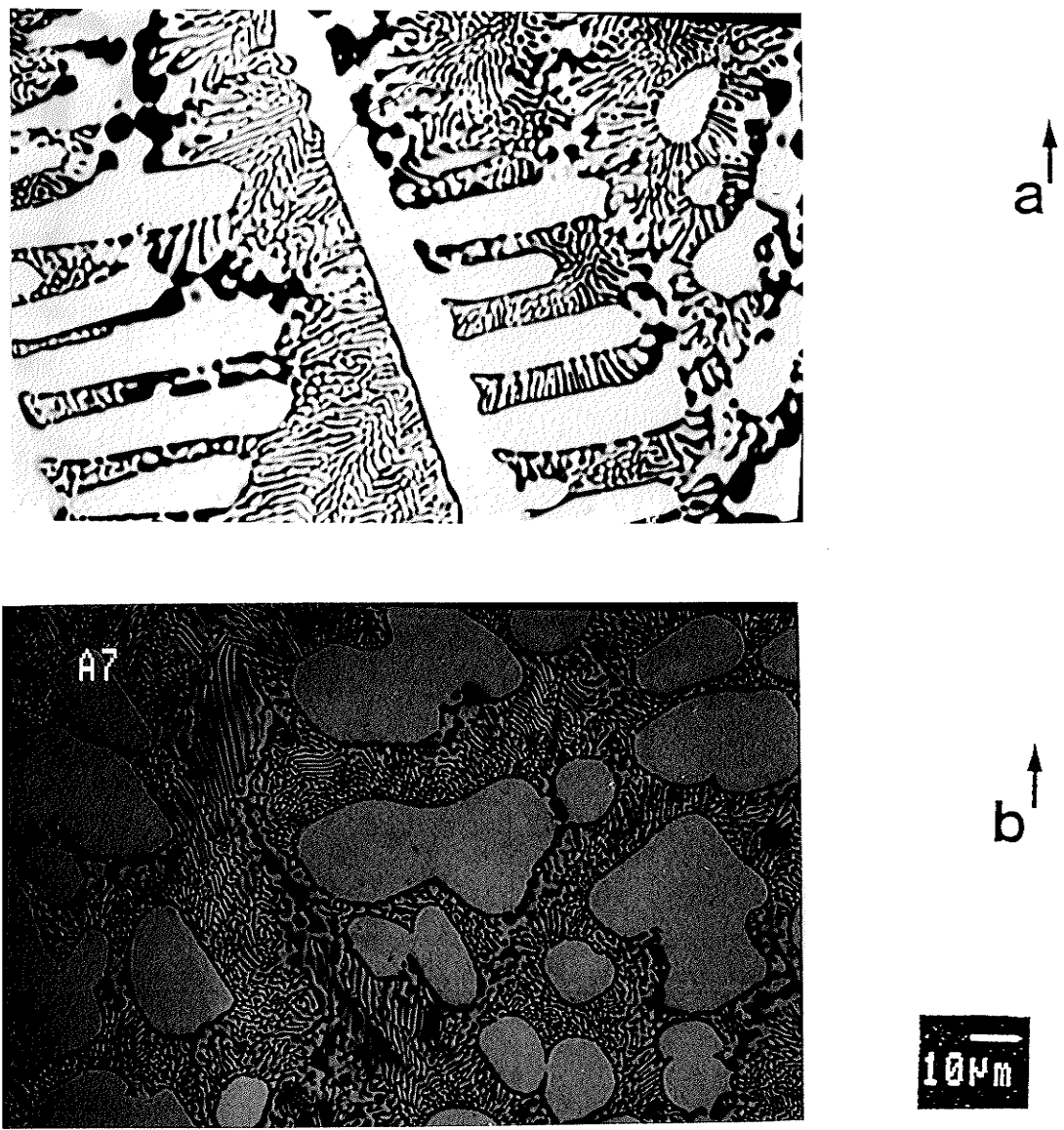


Figure 4.4

Microstructure of hypereutectic Al-Cu alloys at different compositions (Longitudinal sections 600X).

- (a) Al-35Cu(series A)
- (b) Al-38Cu(series A)

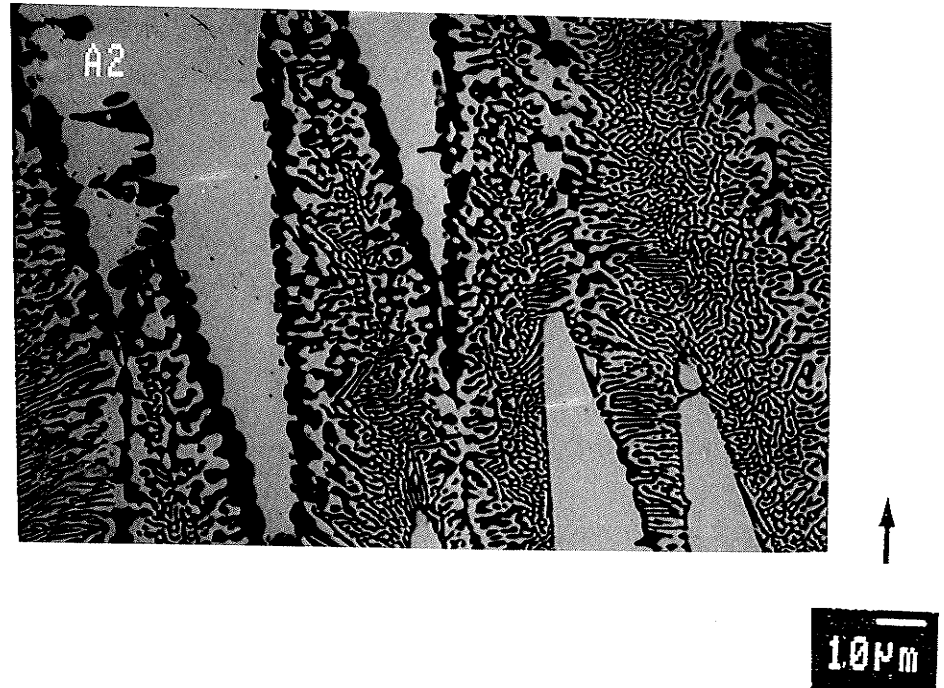


Figure 4.4 continued

(c) AL-50Cu(series A)

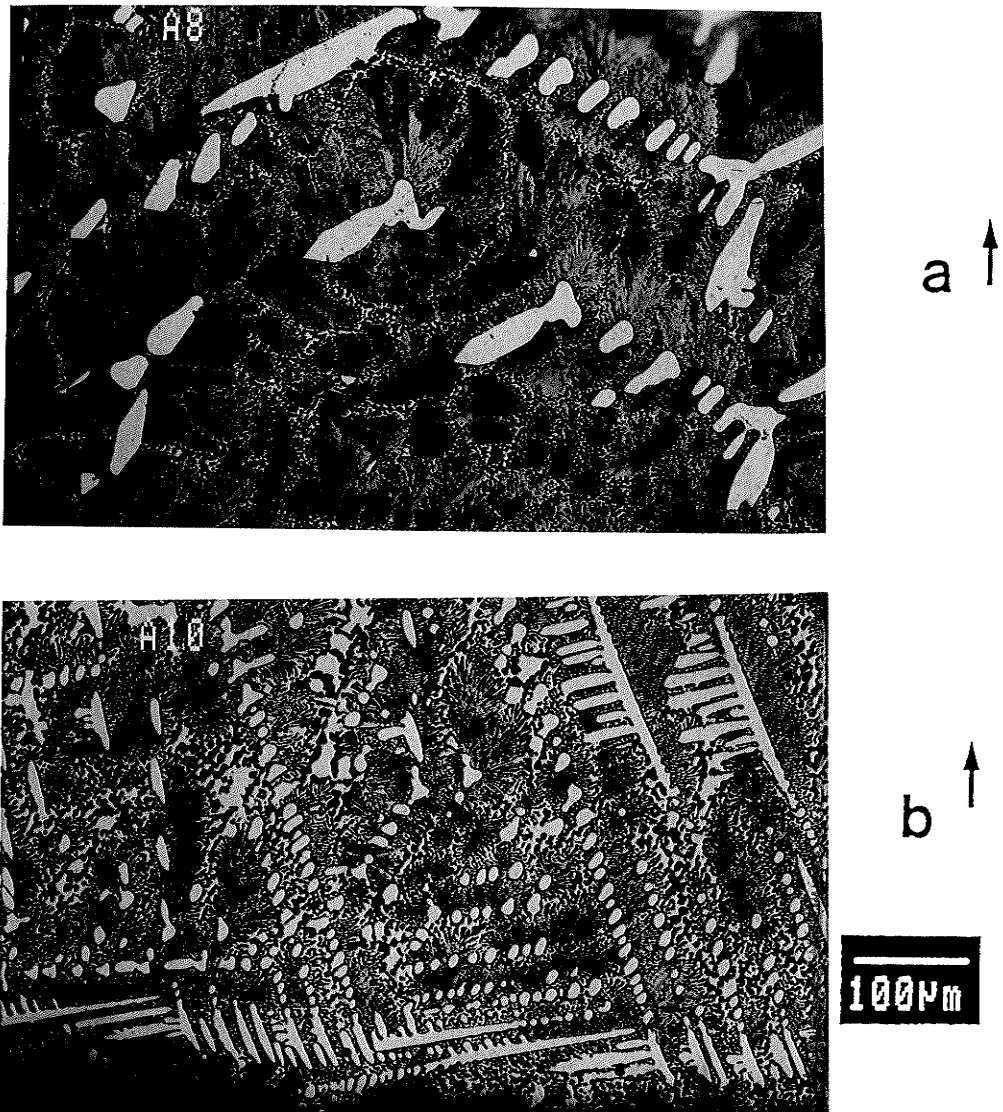


Figure 4.5

Longitudinal pictures showing the dendritic growth morphology of the Al_2Cu primary phase along the solidification direction in an alloy of 35% Cu (series A).

(a) at the top

(b) at the chill

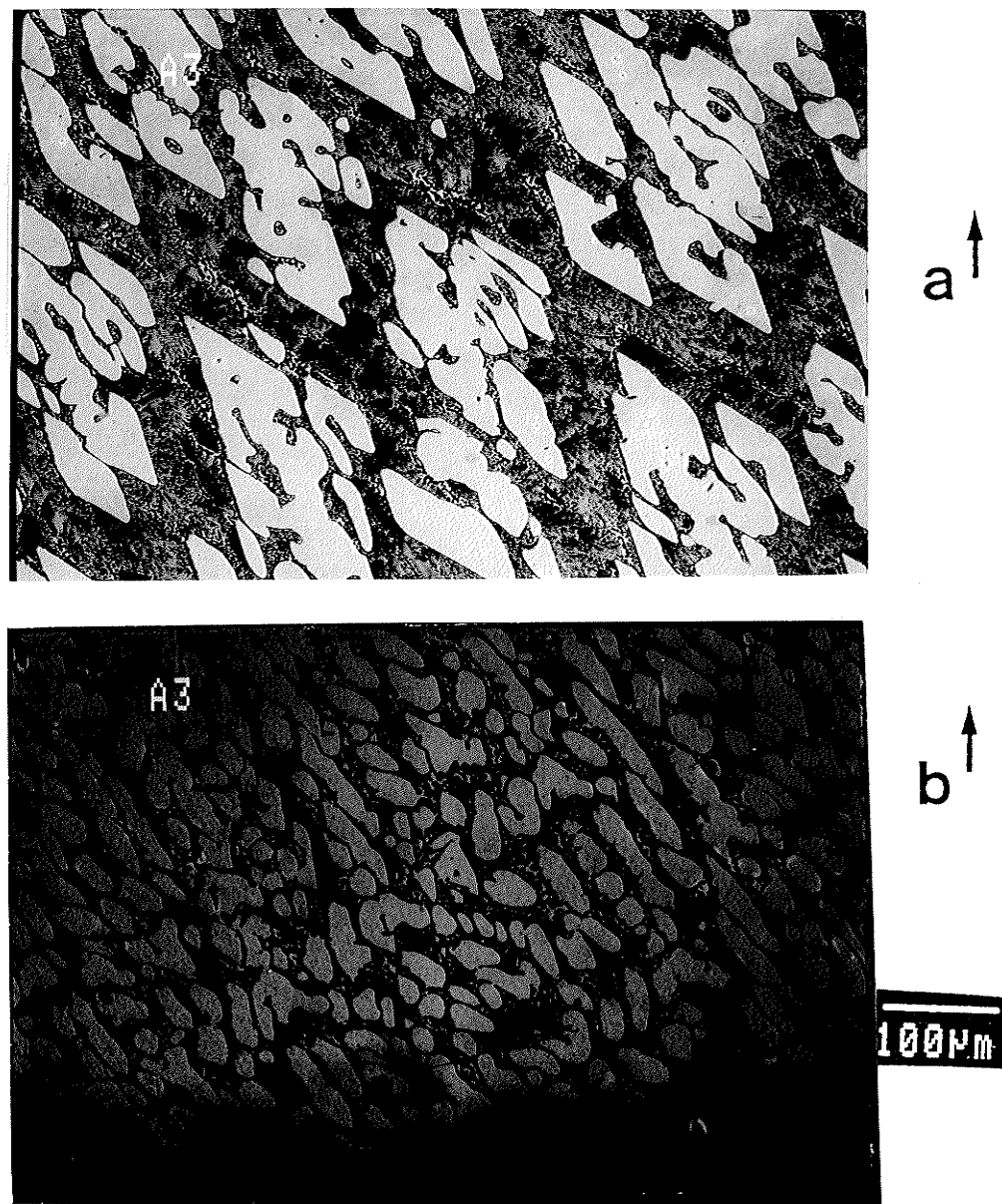


Figure 4.6

Longitudinal pictures showing the rounded primaries and less developed primary dendrites at the chill becoming fully faceted at the top of Al-38Cu (series A).

(a) at the top

(b) at the chill

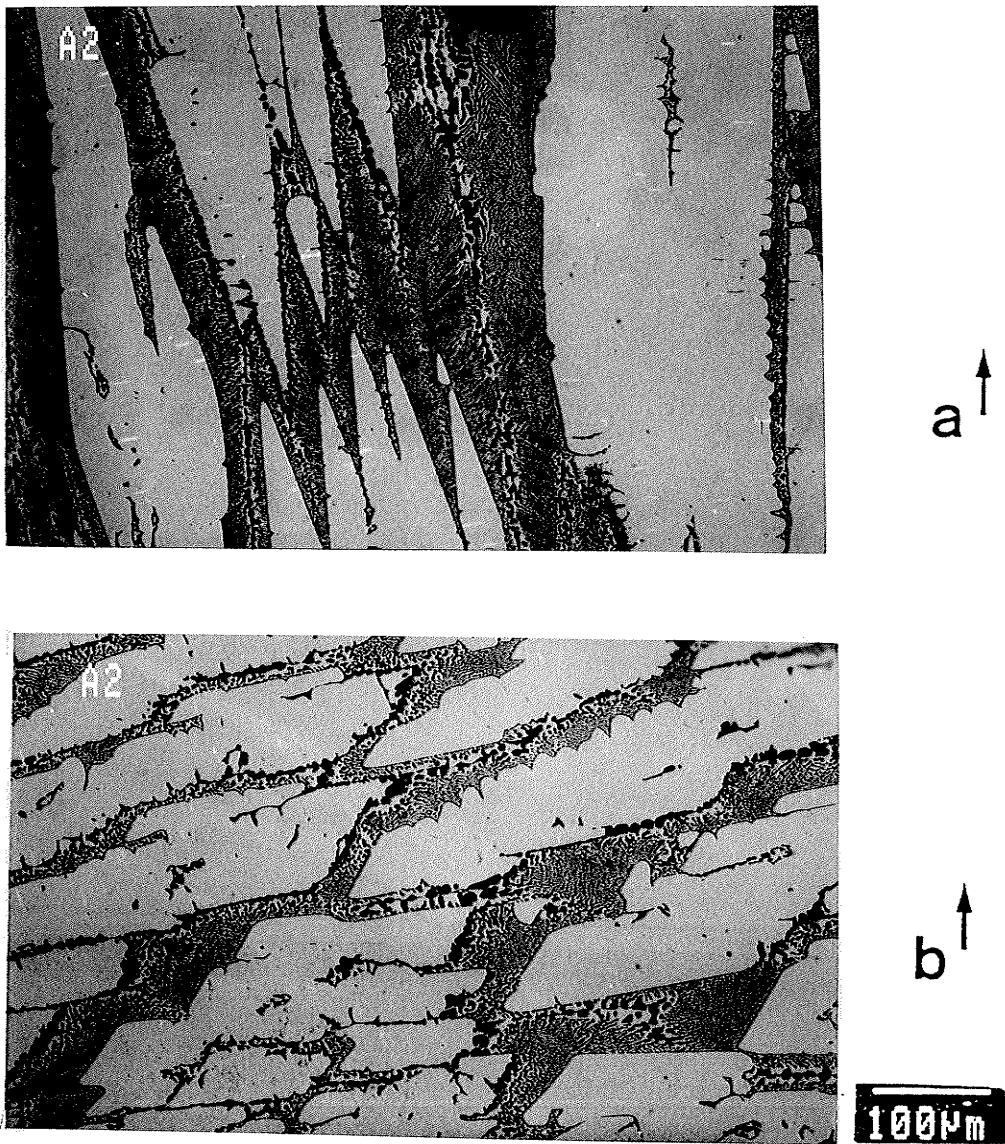


Figure 4.7

longitudinal pictures of Al-50Cu showing the faceted morphology of Al₂Cu phase in the beginning of solidification and elongated grain structure as solidification progressed further (series A).

- (a) at the top
- (b) at the chill

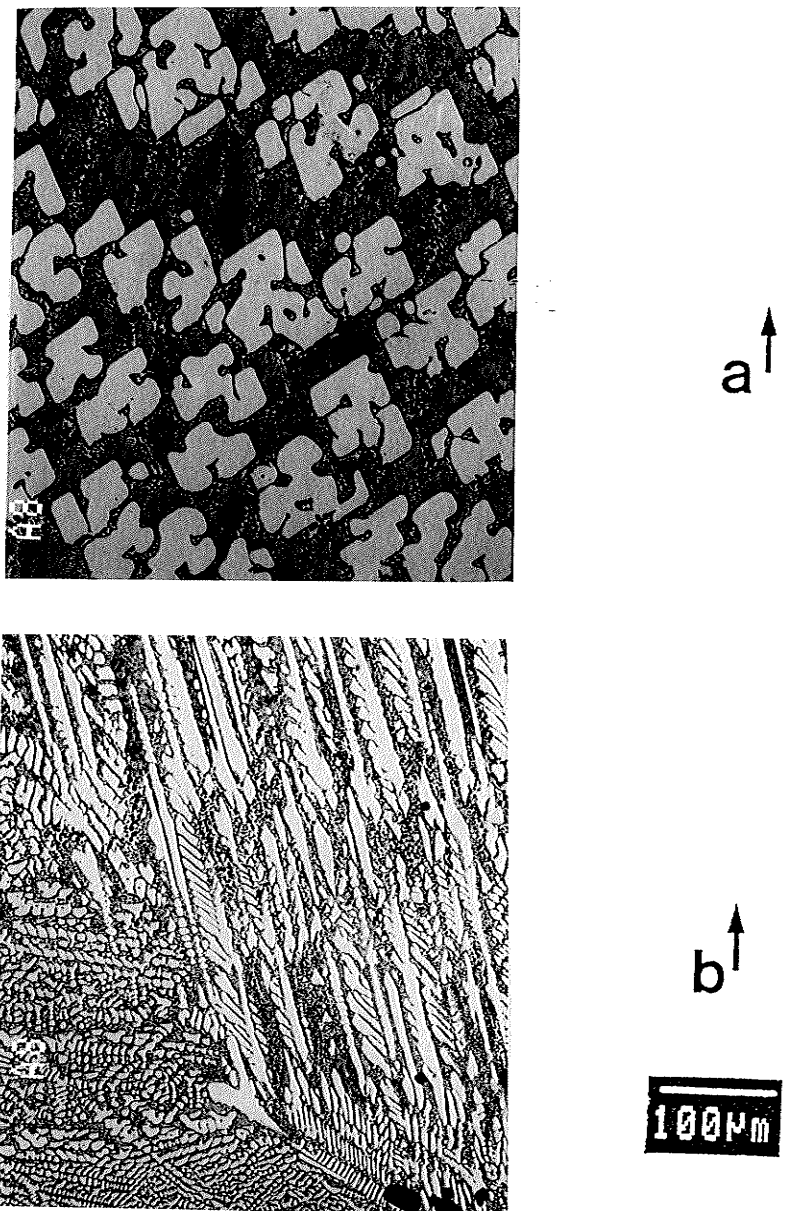
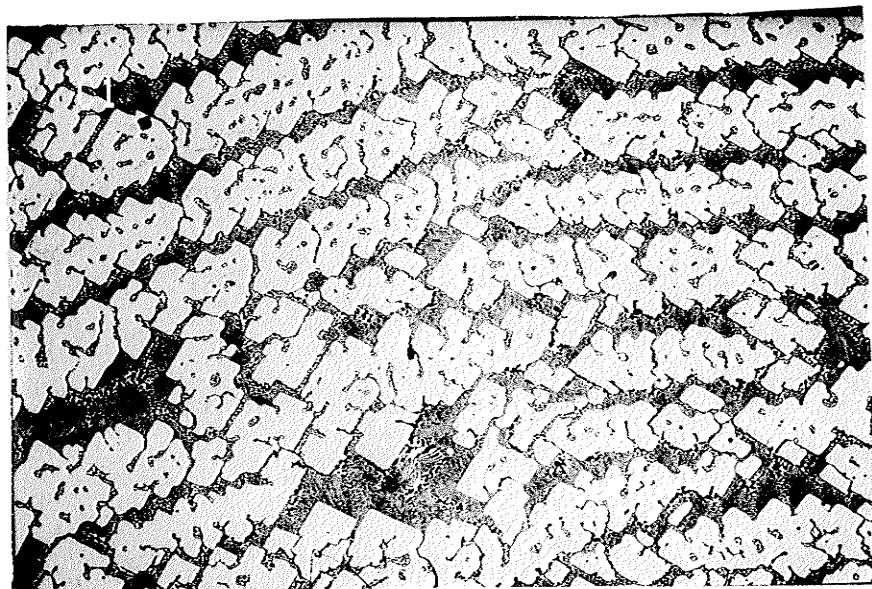


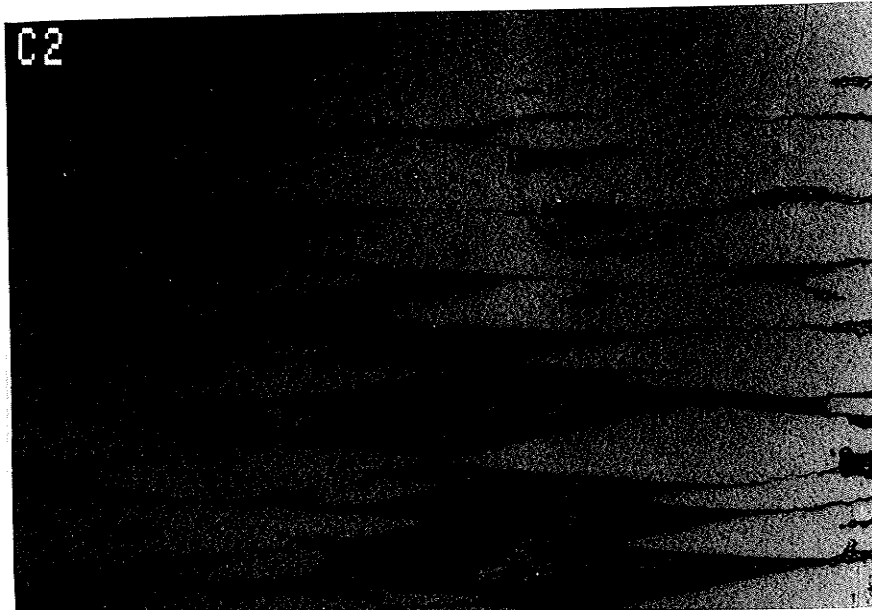
Figure 4.8

Longitudinal pictures showing Al₂Cu primary phase undergoing a transition from a dendritic to a faceted growth morphology along the length of the Al-38Cu sample (series B).

- (a) at the top
- (b) at the chill



a



b



Figure 4.9

Transverse sections at the centre of samples show faceted morphology of Al_2Cu phase in the air cooled sample and in the furnace cooled sample of Al-40Cu(series A).

(a) air-cooled sample

(b) furnace-cooled sample

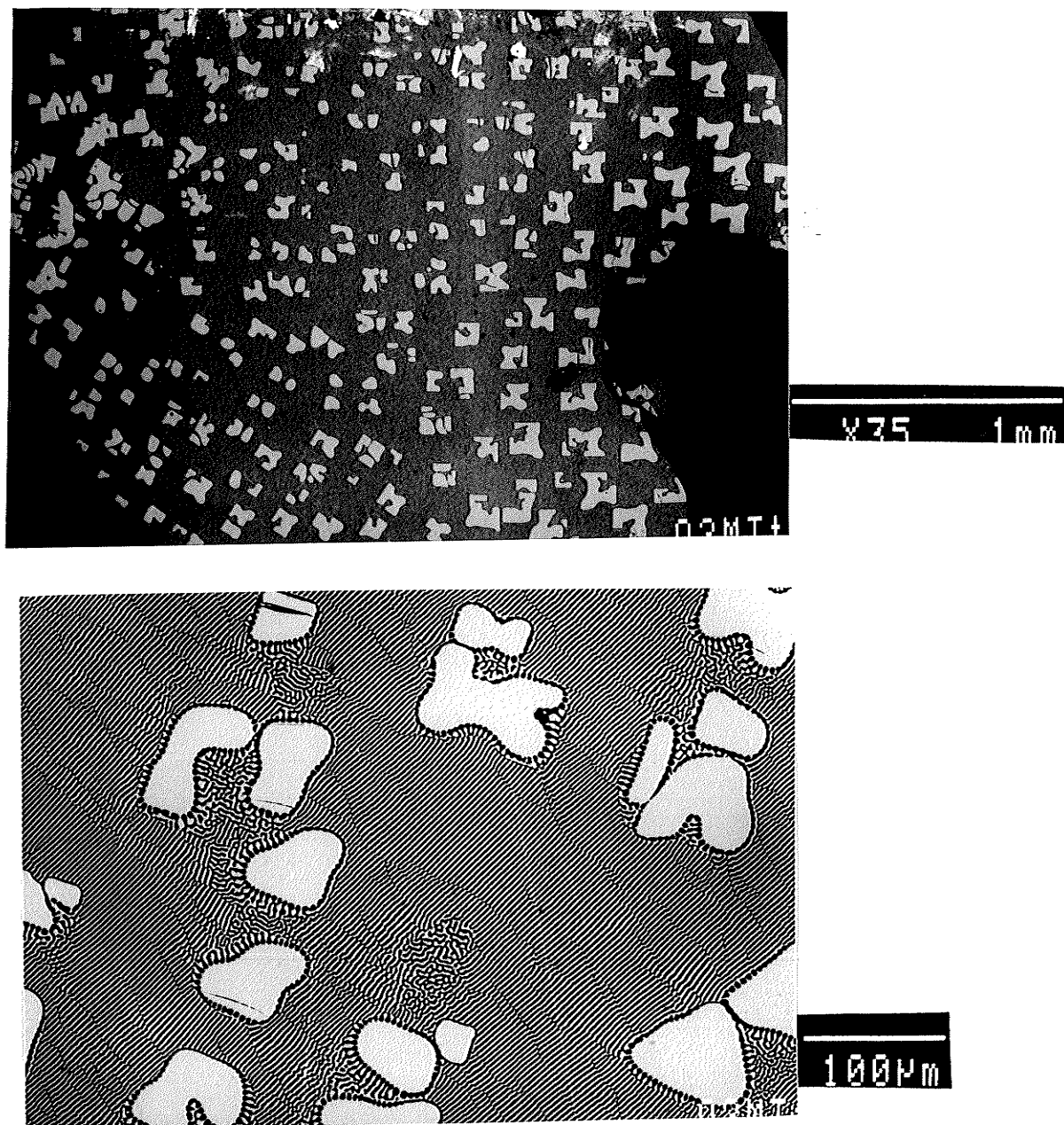


Figure 4.10

Transverse sections of QUESTS samples(series C).

(a) Al-37Cu on ground(↑)

* ↑ indicates the solidification direction.

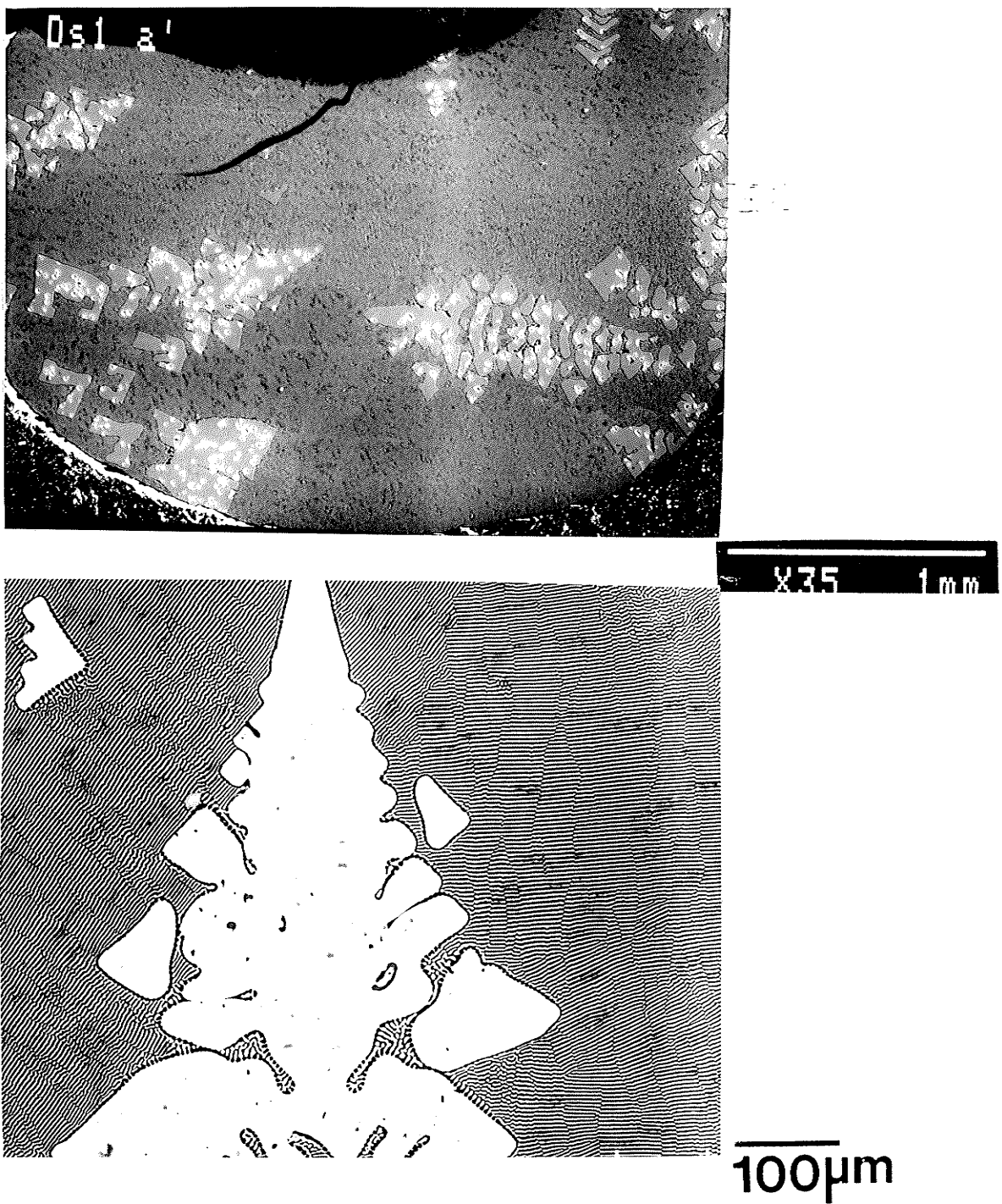


Figure 4.10 continued

(b) Al-38Cu space sample

4-4 INTER-PARTICLE AND DENDRITIC SPACINGS

The average primary arm spacings between growing θ phases, measured from the longitudinal sections of two series (A and B) samples, are summarized in Table (4-4 a). A comparison between the two (Al-50%Cu and Al-38%Cu, series A) samples as well as the two (Al-46%Cu and Al-41%Cu, series B) samples showed that the primary θ phase spacings decreased as the Cu content increased. Again, by comparing the Al-41%Cu chilled sample (series B) with the Al-41%Cu aircooled sample and the furnace cooled sample, it is concluded that the primary θ phase spacings decreased as the cooling rate increased.

The primary spacings of the (QUESTS, series C) ground based sample, were measured using an Image Analyzer from the micrograph of transverse sections. The result of primary spacings measured at the different locations of the transverse sections of the samples are summarized in Table(4-4 b). It is clear that for each sample the primary spacings remain almost constant along the length of the samples. Comparison between the ground based samples(1, 2) and space sample(3), it has shown that the primary θ phase spacing in space is 4 times that of the θ phase particles spacing on ground. However, that the secondary arm spacing in space sample has comparable size as the primary θ phase particles spacing in ground sample.

The lamellar spacings of the Al-Al₂Cu eutectic was also measured from the Image Analyzer. The spacings between the eutectic fault lines were measured from the transverse sections by counting the number of fault lines intersected with the 200 μ m line parallel to the eutectic lamellar. The result is summarized in Table(4-4 b). It is

clear from the measurements that the lamellar spacings of eutectic and the spacings between fault lines also remain constant along the length of the solidified samples and they are in the same range of order between the space sample and ground based samples.

The inter θ -phase eutectic had similar lamellar spacings for both the ground based and space samples, since both the θ phase and α phase lamellae of the eutectic solidify simultaneously.

The primary arm spacing, λ_1 , is described by the empirical relation:

$$\lambda_1 = K G^a R^{-b} \quad (4-1)$$

where G is the temperature gradient, R is the growth rate and K is a constant. Both a and b in relation(4-1) are close to 1/2.

In the series C experiment, the cooling rate was closely controlled by the three zone gradient furnace. After solidification was initiated, both G and R should be fairly constant along the ingot. Primary spacings, which are determined by G and R , should also remain constant. On the other hand, the difference in spacings between the space and the ground based samples clearly demonstrates that natural convection reduces λ . Camel et al[68] concluded that the departure of λ from theoretical diffusive laws is correlated to the convective parameter Γ (ratio of the interdendritic flow rate to solidification rate). This departure was found to occur when Γ becomes of order 1. In convective transport conditions, the primary spacing adjusts itself, so that the

interdendritic flow rate, driven by the solutal convection, remains of order of the solidification rate. In the convective regime the primary spacing increases as $R^{1/2}$ and thus goes through a maximum vs R at the convecto-diffusive transition. They observed a factor of 5 between the θ phase particle spacings in space and ground based specimens.

From this experiment, it is observed from Figure(4-10) that the microstructure of primary θ phase is strongly influenced by convection. The viscous stress due to natural convection disturb the atoms incorporate into the crystals and retarded the θ phase growth. Furthermore, the physically moving of the nucleation sites due to the natural convection provide more nuclei for the growth of more θ phase particles. Therefore, it is reasonable that the ground based sample will exhibit more but smaller θ phase particles than the space sample and thus have a smaller inter-particle spacing.

The lamellar spacing of the eutectic, λ_{eu} , is determined by a compromise between two opposing factors:

- . solute diffusion, which tends to reduce the spacing
- . surface energy (interface curvature), which tends to increase the spacing.

The λ_{eu} and the growth undercooling, ΔT , are given by[6]

$$\lambda_{eu} = \Phi K_l / R^{1/2} \quad (4-2)$$

and

$$\Delta T = [(\Phi + 1/\Phi) K_2 R^{1/2}] / 2 \quad (4-3)$$

where K_1 and K_2 are constants related to the material properties. The Φ is a regularity constant whose value is close to unity for a regular eutectic. Now λ_{eu} depends on the solidification rate and not directly on the cooling rate. The cooling rate is the product of the solidification rate and the thermal gradient. In the series C experiment, as described earlier, the cooling rate remained constant. After the initiation of solidification, a steady state growth developed. Both the solidification rate as well as the thermal gradient remained constant through the whole ingot which will cause the lamellar spacing of the eutectic to remain constant along the length of the sample.

The similar inter θ -phase eutectic lamellar spacings for both the ground based and space samples are determined by the solute diffusion. Since both the θ phase and α phase lamellae of the eutectic solidify simultaneously, the effect of convective mixing (or lack of it) on the eutectic structure is expected to be small since the lamellae spacing is controlled primarily by the rate of diffusion in the liquid which should not be influenced by the magnitude of gravity.

Table 4-4 (a) Primary Arm Spacings (λ_1) between θ phase

Sample	Distance from Chill (mm)	Prim. Arm Spacings (μm)
Al-50Cu (A)	4	77 ± 1
	12	58 ± 1
	14	66 ± 1
	Aver.	67 ± 1
Al-38Cu (A)	4	97 ± 1
	12	99 ± 1
	14	111 ± 1
	Aver.	102 ± 1
Al-46Cu (B)	4	56 ± 1
	12	69 ± 1
	14	54 ± 1
	Aver.	59 ± 1
Al-41Cu (B)	4	115 ± 1
	12	110 ± 1
	14	85 ± 1
	Aver.	103 ± 1
Al-41Cu (Air cooled)	Average	126 ± 1
Al-41Cu (Furnace cooled)	Average	136 ± 1

Table 4-4 (b) Measurement of Spacings for QUESTS Samples
 (1) Al-38Cu 1 G, vertically solidified sample

Dist. from Bottom (mm)	Primary Spacings of θ phase λ_1 (μm)	Lamellar Spacings of Eutec. λ_{eu} (μm)	Spacings of Eutec. Fault lines λ_f (μm)
22	170 ± 6	4.4 ± 0.5	
25	166 ± 7	4.8 ± 0.2	14.2 ± 0.6
48	175 ± 8	5.8 ± 0.4	19.0 ± 0.6
50	174 ± 5	5.7 ± 0.8	

(2) Al-40Cu 1 G, horizontally solidified sample

Dist. from Bottom (mm)	Primary Spacings of θ phase λ_1 (μm)	Lamellar Spacings of Eutec. λ_{eu} (μm)
20	170 ± 6	5.5
40	158 ± 5	4.7
57	176 ± 7	5.0

(3) Al-36Cu QUESTS space sample

Dist. from Bottom (mm)	Primary Spacings of θ phase λ_1 (μm)	Lamellar Spacings of Eutec. λ_{eu} (μm)	Secondary Spacings λ_2 (μm)	Spacings of Eutec. Fault lines λ_f (μm)
20	690 ± 14	6.4 ± 0.2	190 ± 14	25 ± 0.6
40	640 ± 14	4.8 ± 0.2	250 ± 14	18 ± 0.6
58	680 ± 14	4.2 ± 0.2		16 ± 0.6

4-5 MACROSEGREGATION OF THE SPECIMEN

4-5-1. MACROSEGREGATION IN SERIES A (MELT-STABILIZED-SOLIDIFIED) SAMPLES

The macrosegregation data shown in Table(4-5) was obtained by employing EDS analysis for the Al-42%Cu and Al-50%Cu (series A) samples. The data indicates that segregation of Cu occurred in both ingots. Figures(4-11) and (4-12) illustrate the copper contents as a function of the distance from the chill face. The solute(Cu) concentration is lower at the chill face and gradually increases as the sample solidified further. This phenomenon was due to the dendritic growth induced inverse-segregation. During solidification Al is rejected from the dendrite which caused a higher concentration of Al in regions that solidified earlier.

For the Al-50%Cu sample, the Cu concentration was much lower at the chill face and increased more rapidly further along the sample. This is caused by the lower melting point of the eutectic, which will melt first and be drained to the bottom during the melting and stabilizing period. The eutectic will stay at the bottom due to a lack of mixing. In this case, the initial composition gradient is existing due to melting.

Table 4-5. Macrosegregation of Al-42Cu and Al-50Cu
 (series A samples)

Distance from Chill (mm)	Cu wt%	Cu wt%
	Al-42Cu	Al-50Cu
0	41.4 ± 0.2	48.3 ± 0.2
2	41.5 ± 0.3	49.4 ± 0.3
4	41.1 ± 0.1	50.3 ± 0.2
6	40.9 ± 0.3	50.9 ± 0.1
8	41.3 ± 0.2	50.4 ± 0.1
10	42.3 ± 0.1	50.9 ± 0.2
12	41.8 ± 0.1	50.9 ± 0.3
14	42.9 ± 0.1	51.0 ± 0.2
16	42.9 ± 0.2	51.4 ± 0.1
18	41.2 ± 0.1	51.1 ± 0.1
20	41.9 ± 0.2	51.3 ± 0.2
22	43.4 ± 0.1	51.2 ± 0.2

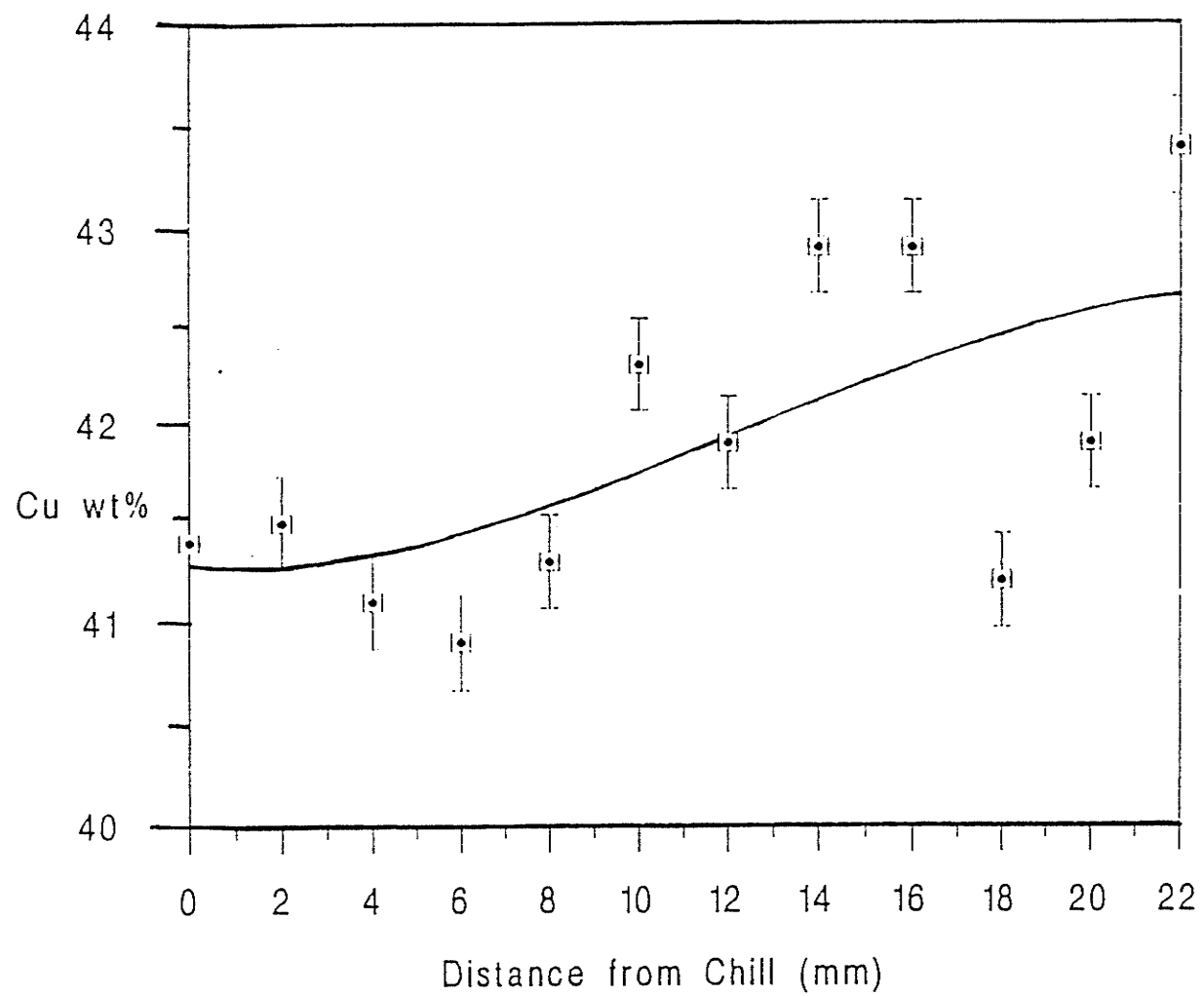


Figure 4.11

Macrosegregation of Al-42Cu series A sample.

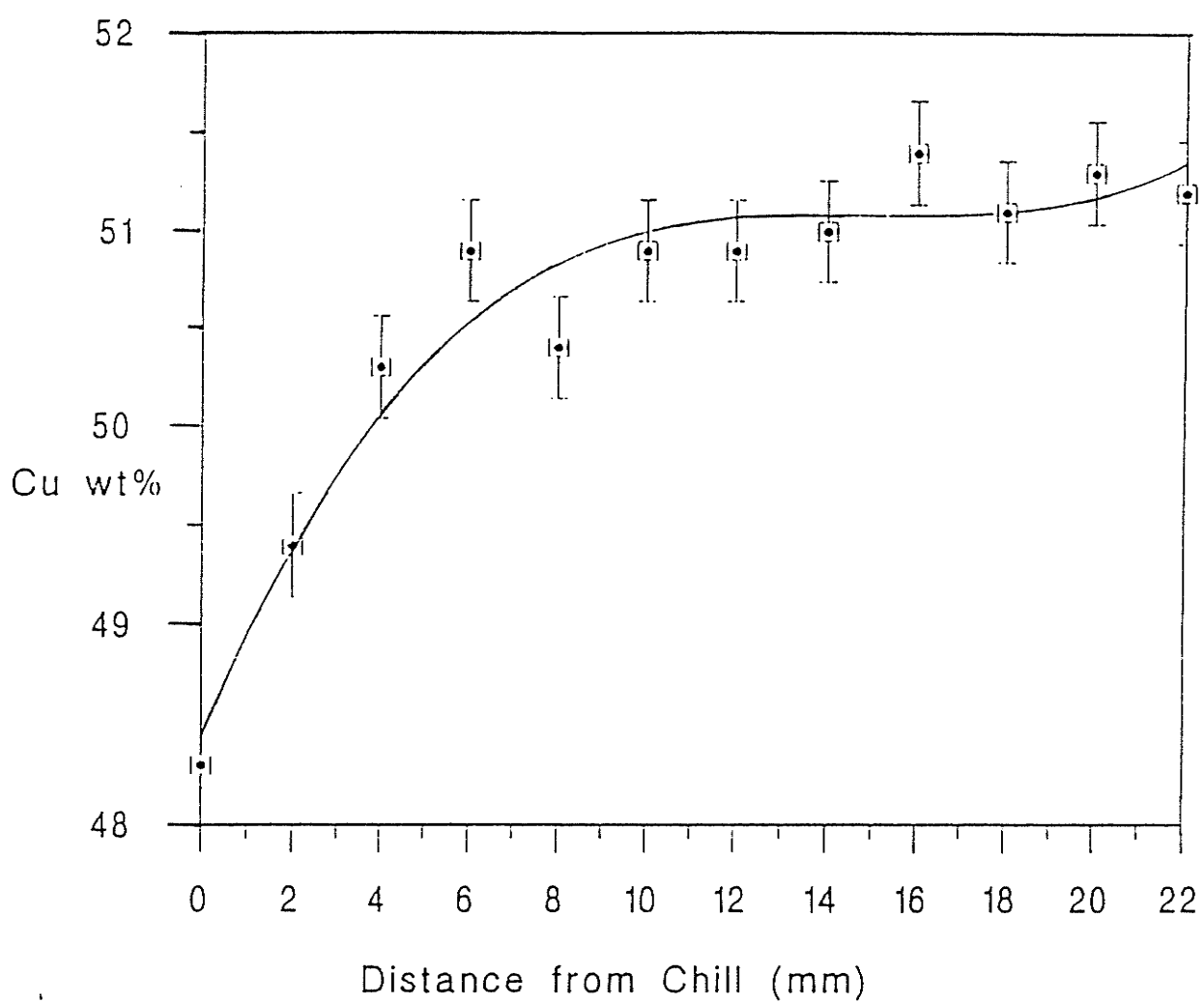


Figure 4.12

Macrosegregation of Al-50Cu series A sample.

4-5-2. MACROSEGREGATION IN SERIES B (MELT-MIXED-SOLIDIFIED)

SAMPLES

Macrosegregation data of the samples from the second series of experiments (series B) is shown in Table(4-6). In this series, the melt was mixed mechanically before solidification. Data were obtained by an EDS analysis. The Al-38%Cu sample was solidified in a direction opposite to gravity. The resulting data indicated that segregation of Cu also occurred in this case. Figure(4-13) illustrates the Cu content as a function of the distance from the chill face. The Cu content is fairly constant along the length of the sample up to a distance of 8mm from the chill. The maximum Cu content occurs at 13mm from the chill. A sudden Cu composition drop is observed at the top. It is noticed that there is no initial composition gradient exist in this sample, which may due to the mechanical mixing and fast solidification process.

The different segregation results from the two sets of experiments can be explained in terms of gravity effects, buoyancy effects and phase-change effects (shrinkage or expansion) during the solidification processes. For hypereutectic Al-Cu alloys, the first solidified θ phase is heavier than the liquid. Gravity will drain the heavier phase down to the chill bottom. This will increase, in turn, the average composition of Cu in the lower portions of the ingot above the nominal composition. However, gravity effects are not only contribution factor to interdendritic fluid flow. In the hypereutectic Al-Cu region, the interdendritic liquid becomes enriched in Al, up to the eutectic composition (33.2%Cu). The density of the bulk liquid at the interface would be lower than the θ phase. Thus there is a density inversion through the solid-

liquid region which causes the less dense liquid to rise. Consequently buoyancy effects lead to a higher Cu content at the lower region of ingot. Phase change effects (shrinkage or expansion) should also be taken into account because the eutectic solid is denser than the eutectic liquid. If the shrinkage effects dominate, the part of the ingot which solidified first is usually richer in Al and lower in Cu. In actual solidification processes, gravity effects, buoyancy effects and phase-change effects will act simultaneously. Buoyancy effects and gravity effects may tend to counteract shrinkage effects. The segregation phenomena observed depends upon which effect predominates.

As the growth rate increases, the amount of macrosegregation will decrease from gravity and buoyancy effect . This would be expected because the amount of time available for the flow decreases as R increases. For the A and B experiments , samples were quickly solidified upwards. The gravity and buoyancy effects were depressed by fast cooling. Mostly because of phase change (shrinkage) effects, the Cu content is lower at the chill as observed in Figure(4-13).

Table 4-6. Macrosegregation of Al-38Cu
(series B sample)

Distance from Chill (mm)	Cu wt% Al-38Cu
0	37.1 ± 0.2
2	37.4 ± 0.1
4	37.1 ± 0.1
6	37.4 ± 0.2
8	37.7 ± 0.1
10	37.5 ± 0.3
12	38.4 ± 0.2
14	37.9 ± 0.1
16	37.7 ± 0.2
18	36.8 ± 0.1

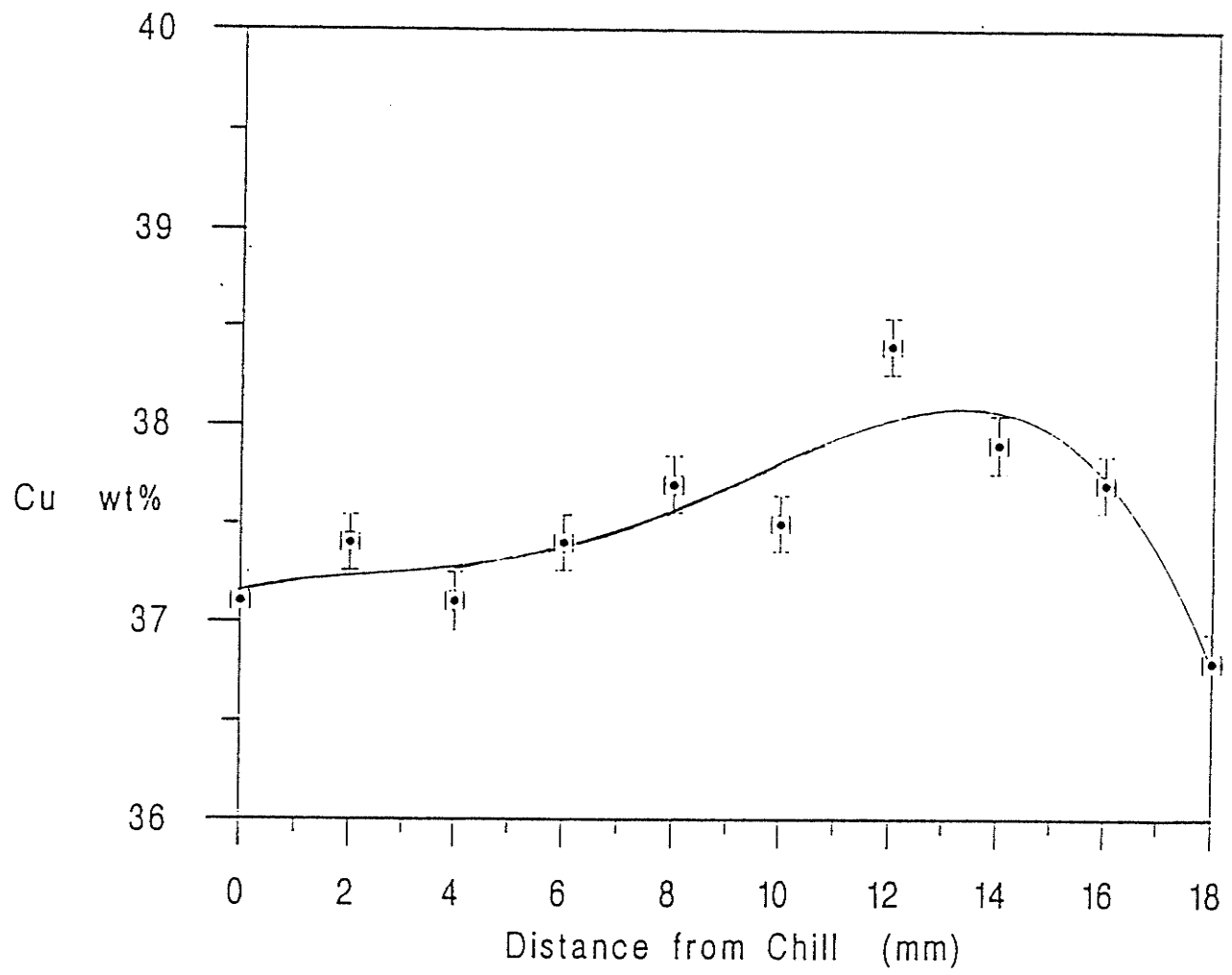


Figure 4.13

Macrosegregation of AL-38Cu series B sample.

4-5-3. MACROSEGREGATION in SERIES C (GRADIENT-FREEZE SLOWLY SOLIDIFIED) SAMPLES

Directional solidification of hyper-eutectic Al-Cu alloys was carried out in the three zone gradient-freeze QUESTS furnace. Alloys of composition of 36, 38 and 40 wt%Cu were unidirectional solidified on the ground both, vertically and horizontally. The macrosegregation data of the ground-based samples are shown in Table(4-7 a).

The microgravity experiment was also performed aboard the space shuttle Endeavour under controlled cooling rates and temperature gradients on the Al-36Cu alloy. After solidification, the sample was cut into 15-25mm long segments. Cross sections were cut from the ends. The segregation data was obtained from transverse sections by the EDS analysis as shown in Table(4-7 b).

Longitudinal segregation was first examined in samples solidified vertically upwards with different solidification rate. The results are given in scaled concentration $C = C_s/C_0$ as a function of the solidified fraction f_s as shown in Figure(4-14). In case (a), the sample with $C_0 \sim 37.5$, solidification at higher rate($R \sim 1.5 \times 10^{-2}$ mm/s) than in case (b), where R is 7.4×10^{-3} mm/s and C_0 is 35.5. It is observed that the segregation in case (a) is higher ($K_E \sim 1.19$) than in case (b), where K_E is 1.08. Clearly, that the segregation is not reduced when solidification rate is increased, but reduced when the nominal composition is lower. It can be concluded that the longitudinal segregation in vertically solidified sample are due to the effect of gravity. For hypereutectic Al-Cu alloys, the first solidified θ phase is heavier than the liquid which results in settling. Also, during solidification the density of the bulk liquid at the interface is lower than

θ phase. The density inversion through the solid-liquid region causes floating. The gravity induced settling and floating result in segregation.

The longitudinal segregation of the horizontal solidification is shown in Figure(4-15). It is noticed that longitudinal segregation in horizontal solidification is slightly more severe ($K_E \sim 1.20$) than in the case of vertical solidification($K_E \sim 1.08$). The partial mixing of the liquid during horizontal solidification has contributed to the segregation.

The longitudinal segregation of the space sample measured from the cross sections of the ingot is shown in Figure(4-16). It is clear that longitudinal segregation is in a much smaller amplitude in microgravity environment. Lack of convection in the microgravity environment has been the result of reduced fluid motions which allows the larger dendrites to grow. During dendritic solidification the flow of the interdendritic liquid is due solely to solidification shrinkage[67] and the flow is normal to the isotherms. Further, when the top of the ingot reached a pasty state, a capillary pressure appeared at the top[30,31] and made the interdendritic liquid flow very difficult. The macrosegregation in the ingots is insignificant because the solidification shrinkage was compensated mostly by the deformation of the ingots rather than by the interdendritic liquid flow.

Table 4-7 (a). Macrosegregation of QUESTS Ground-based Samples

Fraction Solid. g	Al-37Cu (\uparrow) c_s/c_0	Al-35Cu (\uparrow) c_s/c_0	Al-40Cu (\leftarrow) c_s/c_0
0-0.1	0.99	1.06	0.99
0.1-0.1	0.98	1.03	1.00
0.2-0.3	1.09	1.01	1.13
0.3-0.4	1.10	1.00	1.08
0.4-0.5	1.01	0.98	1.13
0.5-0.6	1.02	0.95	1.09
0.6-0.7	0.97	1.03	1.05
0.7-0.8	0.94	0.98	0.97
0.8-0.9	0.91	0.96	0.88
0.9-1.0	0.89	0.94	0.85

* \uparrow indicates the solidification direction.

Table 4-7 (b). Macrosegregation of Al-38Cu QUESTS samples

Trans. Sections (mm from bottom)	Ground-based Sample (Cu wt.%)	Space Sample (Cu wt.%)
20		36.1
22	40.4	
25	40.7	
40		35.97
48	37.9	
50	36.0	
58		35.74

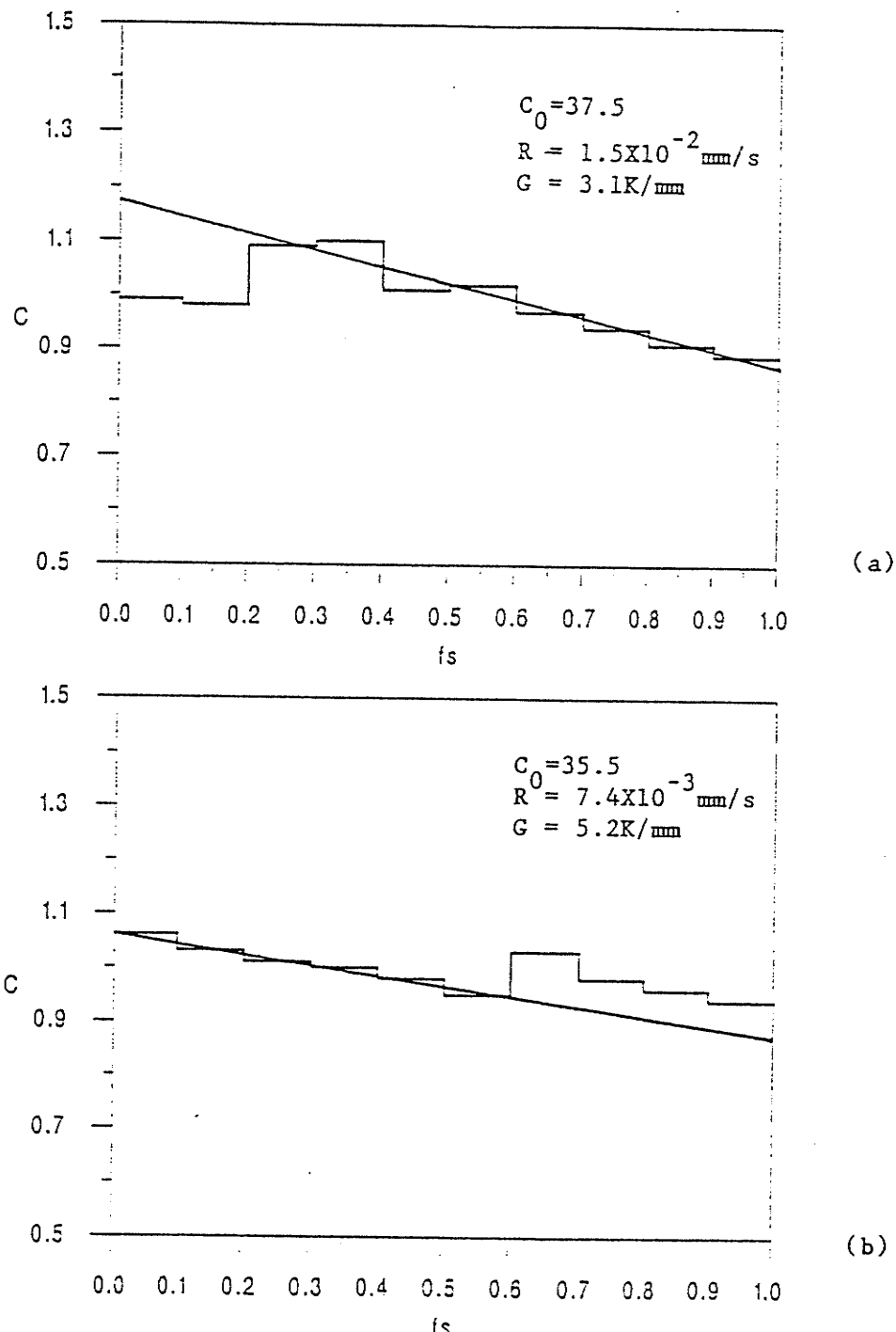


Figure 4.14

Macrosegregation of QUESTS samples in scaled concentration.

(a) Al-37Cu on ground sample(↑)

(b) Al-35Cu on ground sample(↑)

* ↑ indicates the solidification direction.

* The straight line indicates the trend of segregation.

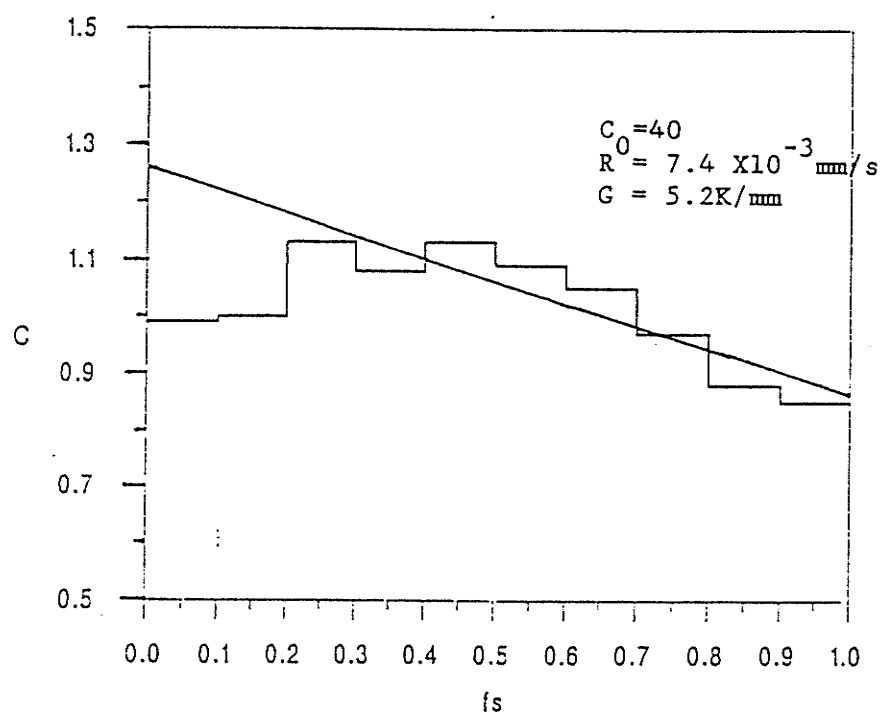


Figure 4.14 continued

(c) Al-40Cu on ground sample(←)

* The straight line indicates the trend of segregation.

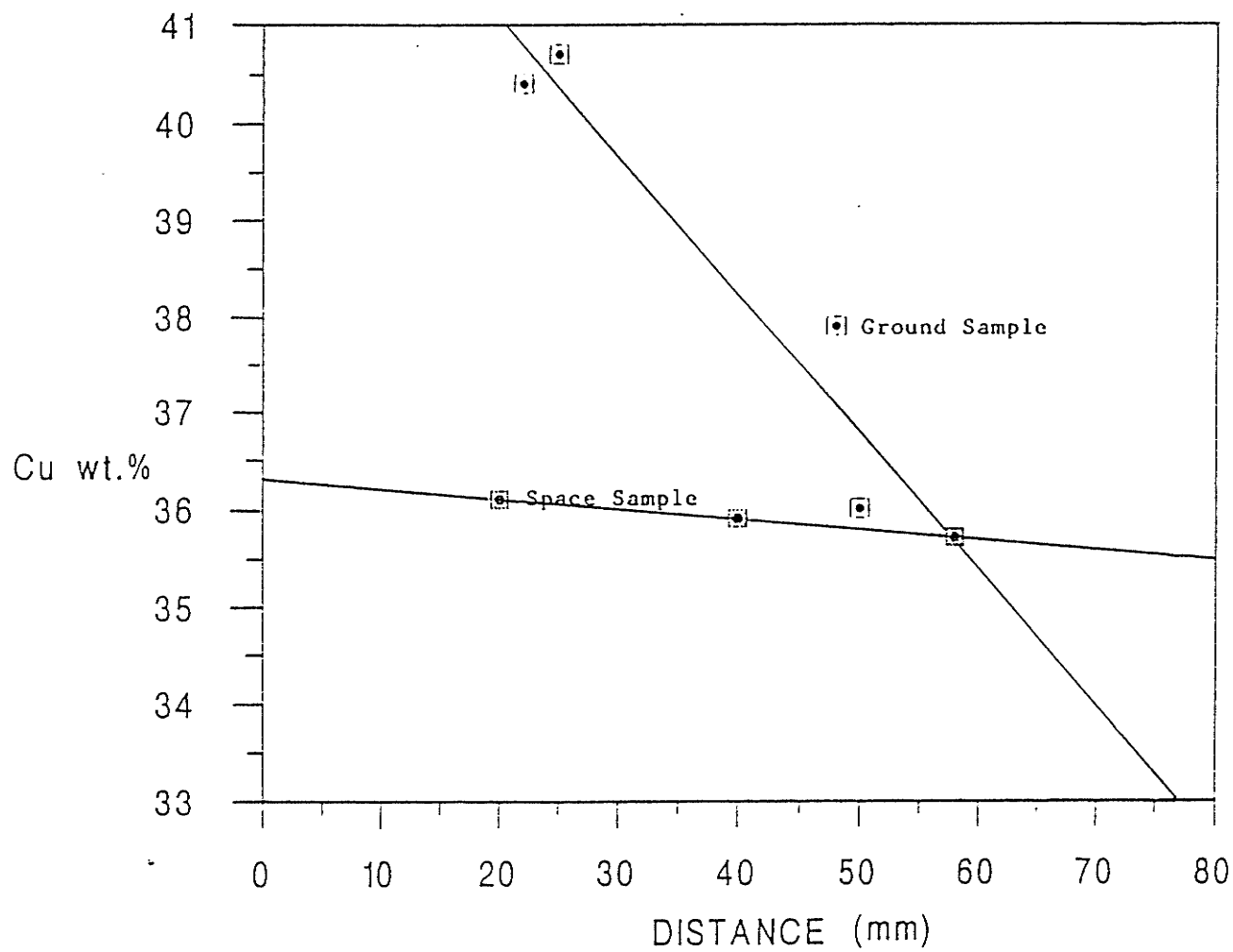


Figure 4.15

Comparison of macrosegregation between Al-38Cu ground-based and space samples.

4-6 K-C 135 SAMPLES

4-6-1 MACRO AND MICROSTRUCTURE

A total of four samples of Al-36%Cu, Al-45%Cu and Al-47%Cu were solidified in zero and 1.8 gravity aboard a KC-135 flight. Longitudinal sections of the samples were examined for directional solidification. Figure(4-16) illustrates the longitudinal sections of four samples at the chill.

The microstructure of the samples were examined by using the SEM. Figure(4-17) illustrates these structures. For the Al-36%Cu sample solidified in zero gravity, the macrostructure at the chill is similar to the one further from chill. However, in higher gravity (1.8 G), primary θ phase particles are much smaller at the chill, as shown in Figure(4-17) (a) and (b). Also, the primary θ phase exhibits dendritic morphology in 0G, whereas, the smooth surfaces with less developed side branches in 1.8G. For the Al-45%Cu sample, primary θ phase particles are faceted and bigger than those in the Al-36%Cu sample. Most θ phase particles are elongated along the heat flow direction. These samples are very brittle and breakage due to polishing can be noticed. However, the microstructure at and away from chill are similar for both 0G and 1.8G samples.

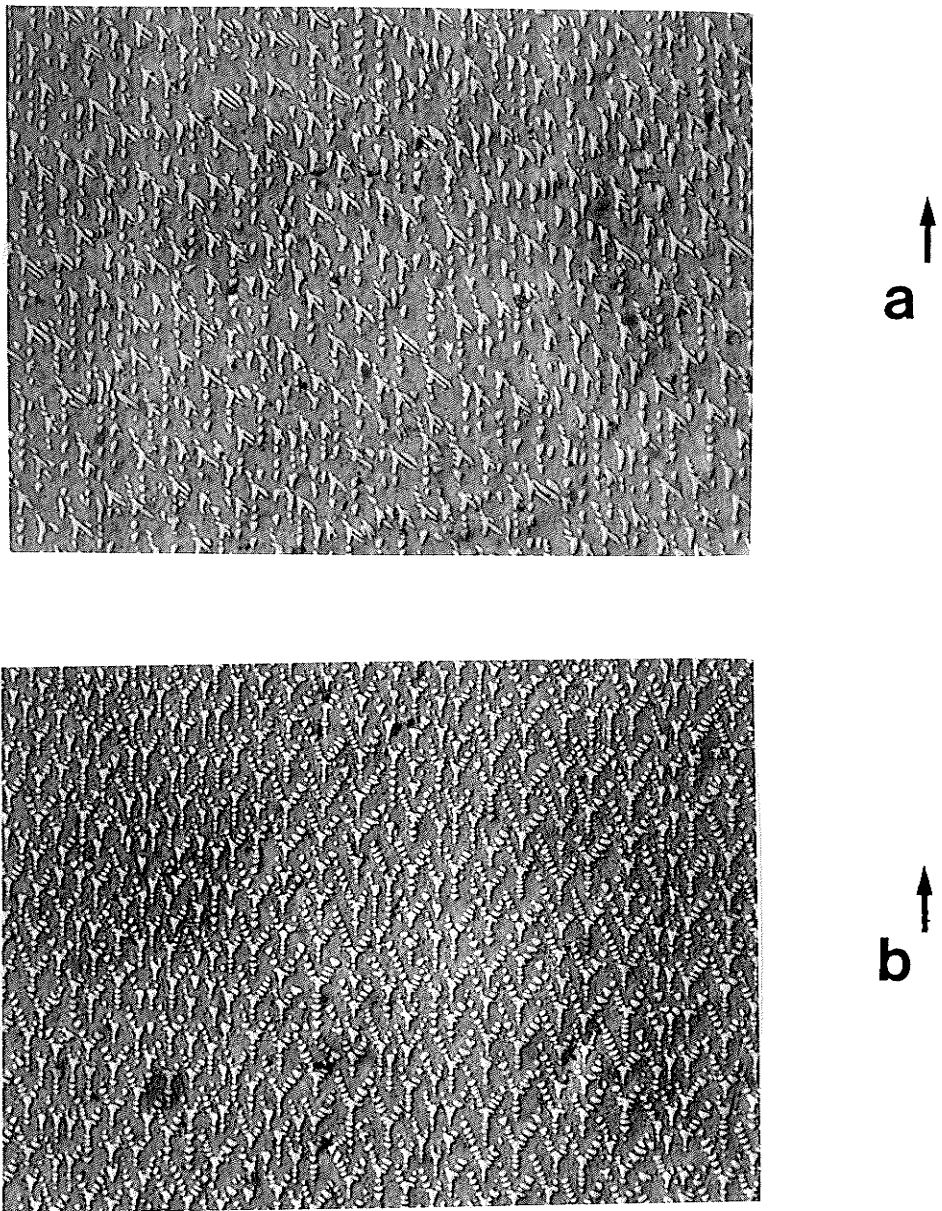


Figure 4.16
Longitudinal sections of KC-135 samples.
(a) Al-36Cu, 0G
(b) Al-36Cu, 1.8G

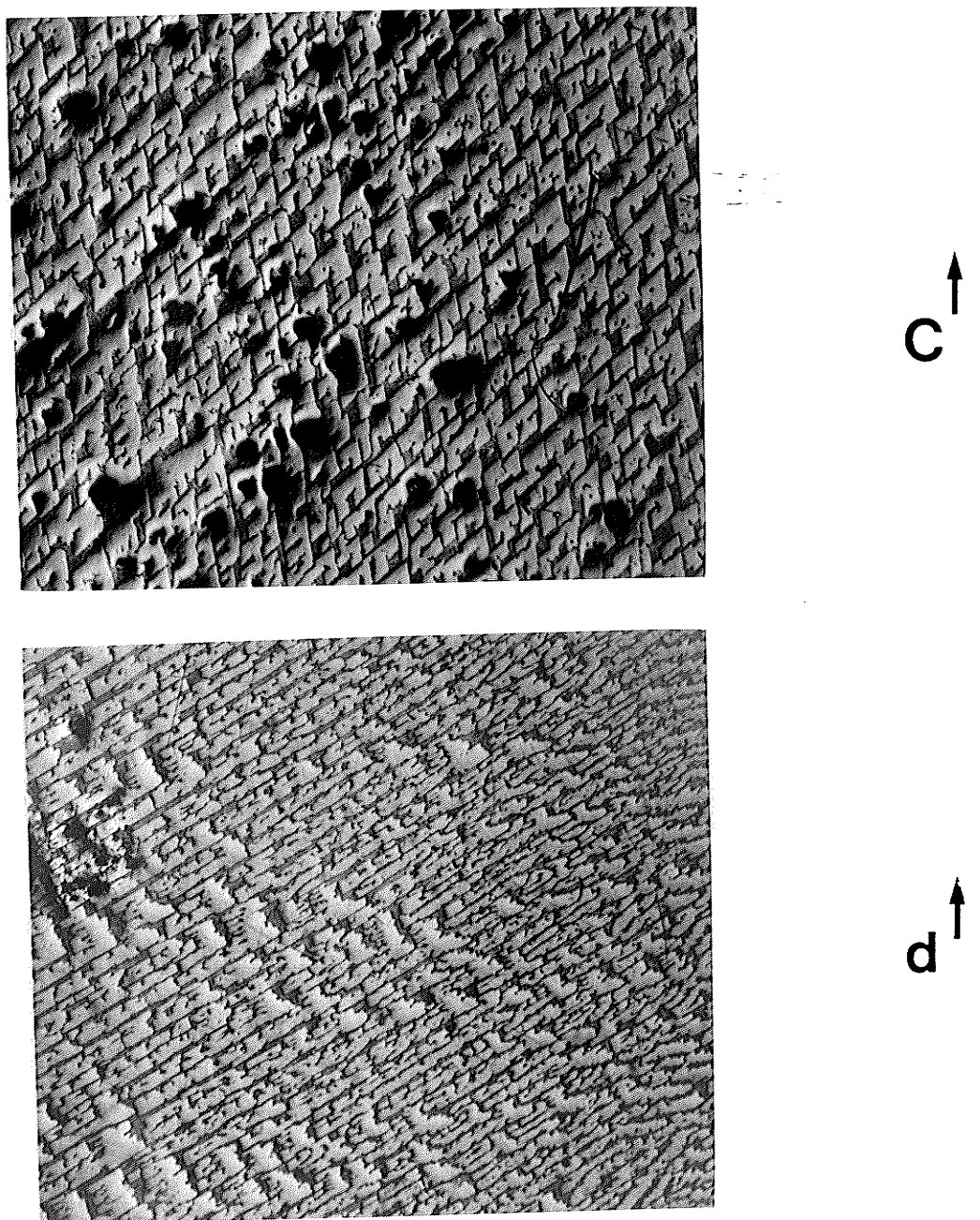


Figure 4.16 continued

(c) Al-47Cu, 0G

(d) Al-45Cu, 1.8G

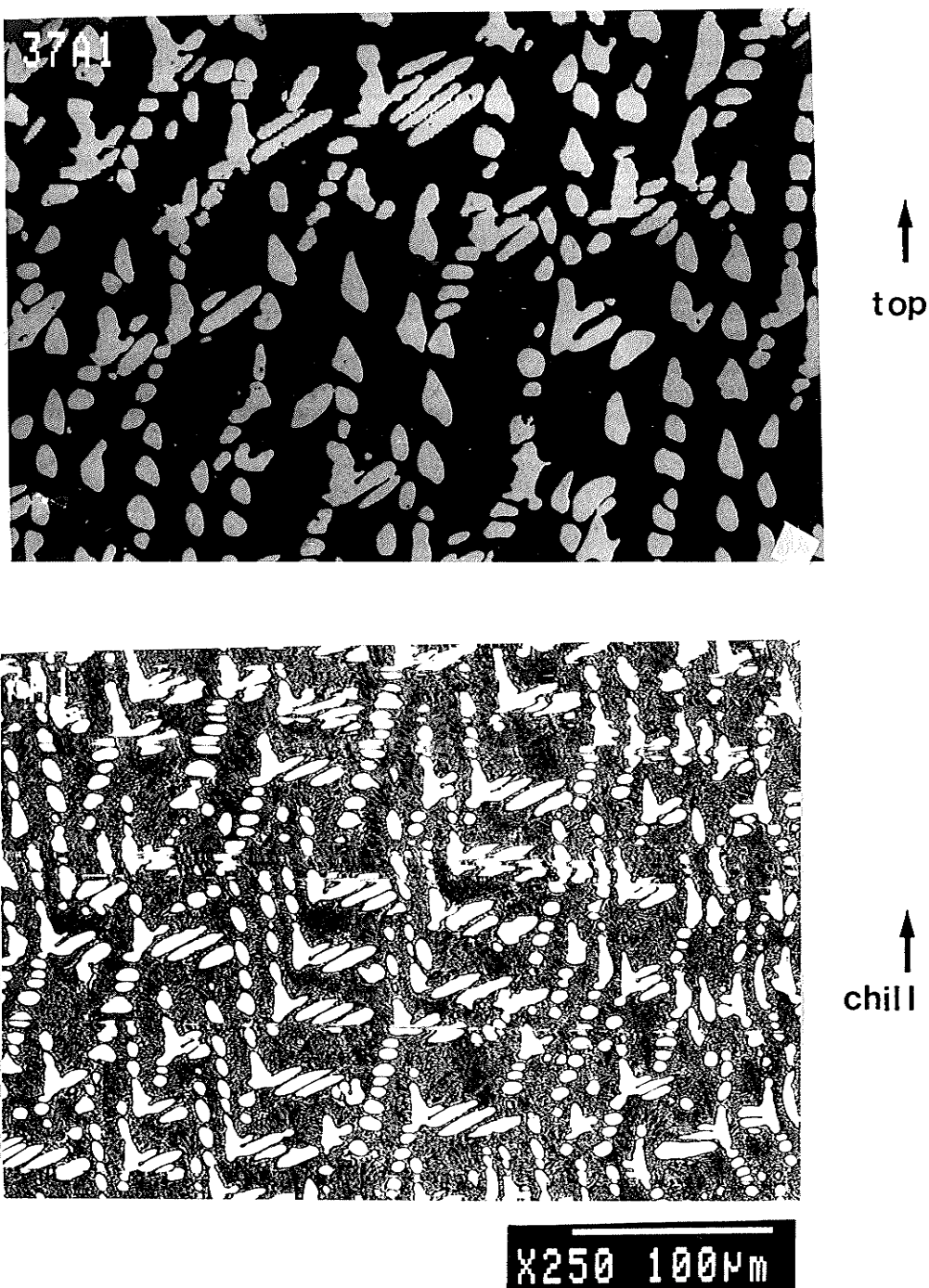


Figure 4.17

Microstructure of KC-135 samples.

(a) Al-36Cu, 0G sample, sections at the top and the chill

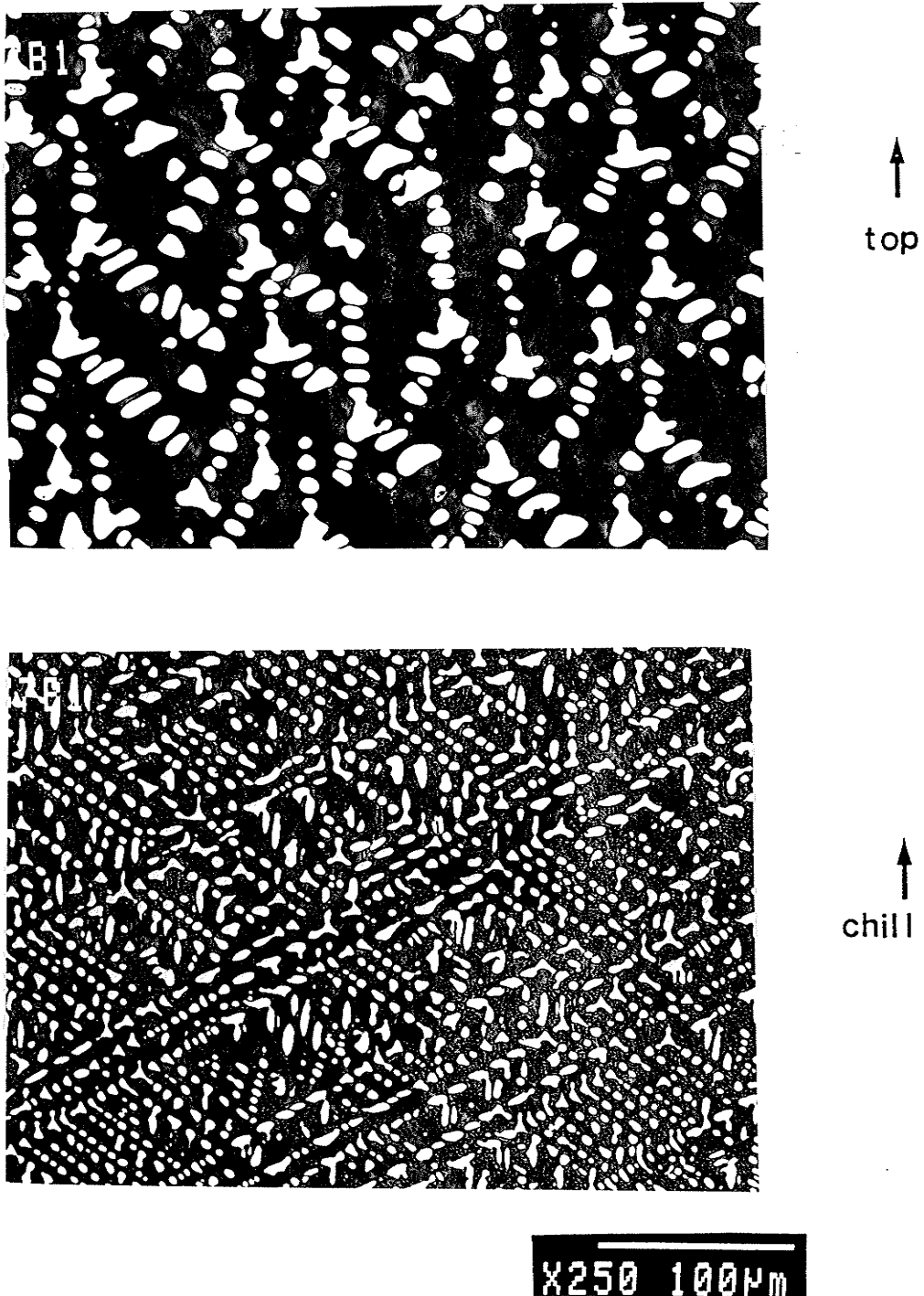
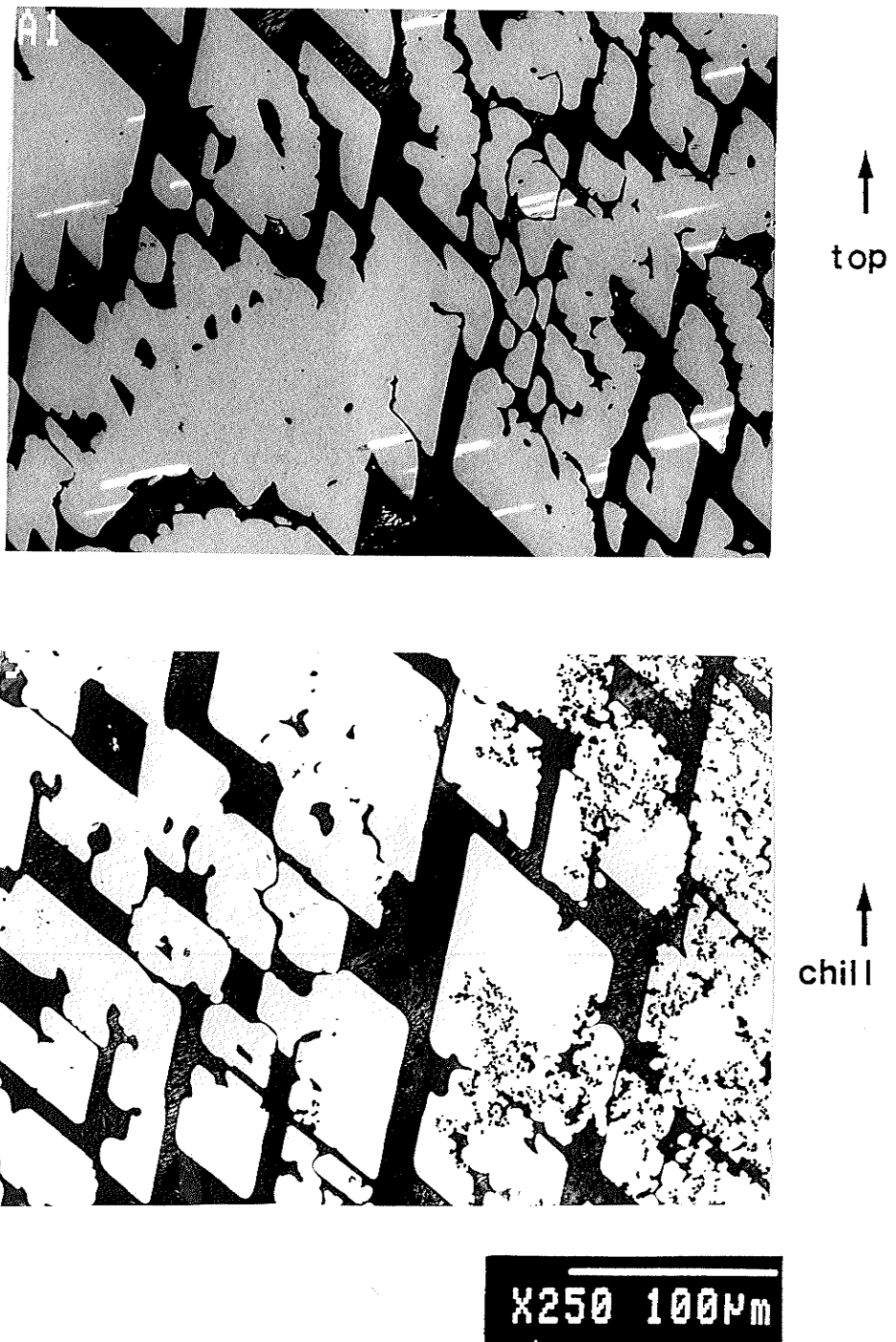


Figure 4.17 continued

(b) Al-36Cu, 1.8G sample, sections at the top and chill



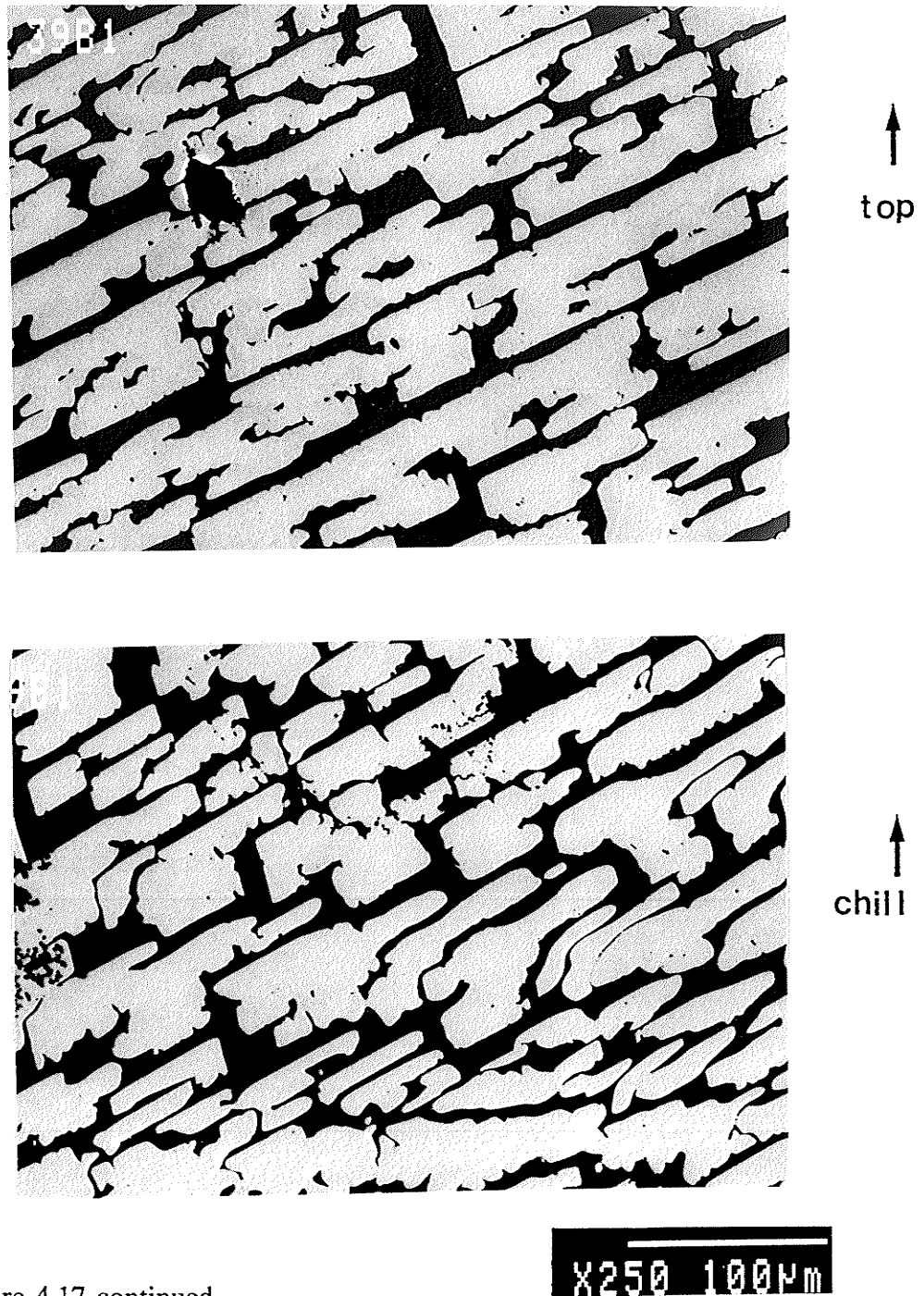


Figure 4.17 continued

(d) Al-45Cu, 1.8G sample, sections at the top and the chill

4-6-2. MACROSEGREGATION

The cooling curves of the KC-135 samples were obtained by using experimental procedure as described in Fariba[44]. Solidification starts at the cooling rate of about 7.4°K/s and the total solidification time was around 13 seconds.

The results of an EDS analysis on the three samples of Al-36%Cu and Al-47%Cu solidified in zero gravity are shown in Table(4-8). The copper content as a function of the distance from the chill are illustrated in Figures(4-18) and (4-19) respectively. Macrosegregation data of both samples showed a fluctuation of compositional change through out the ingot.

Gravity segregation of Cu was noticed in both of the three samples solidified in 1.8 gravity. Figures(4-20) and (4-21) show the copper content as a function of the distance from the chill. For Al-36%Cu sample solidified in 1.8 G, the Cu content is slightly higher at the chill. The minimum Cu content occurred at the middle of the sample. As in the case of the Al-45%Cu sample, the Cu content was higher at the chill and decreased more rapidly along the ingot.

From the samples analyzed, it is obvious that no severe segregation occurred at zero gravity. However, the segregation structure in 1.8G samples are different from the series A samples. The KC-135 samples are much smaller than the one used for series A. The phase change (shrinkage or expansion) has a smaller effect on segregation. Mostly because of buoyancy and gravity effects, the Cu content tends to be higher at the bottom of the ingot and decreases as the solidification progressed along the sample.

Table 4-8. Macrosegregation in KC Samples

Dist.from Chill(mm)	Cu wt%			
	0 G		1.8 G	
	Al-36Cu	Al-36Cu	Al-47Cu	Al-45Cu
0	35.5	35.7	48.1	45.1
0.5	36.2	35.4	48.6	45.3
1.0	35.7	35.1	47.4	45.6
1.5	35.3	35.1	48.3	44.6
2.0	35.5	45.3	47.9	44.7
2.5	36.4	35.4	46.0	43.8
3.0	35.6	35.1	45.3	43.2
3.5	35.8	35.6	47.4	45.8
4.0	36.6	35.9	47.8	44.2

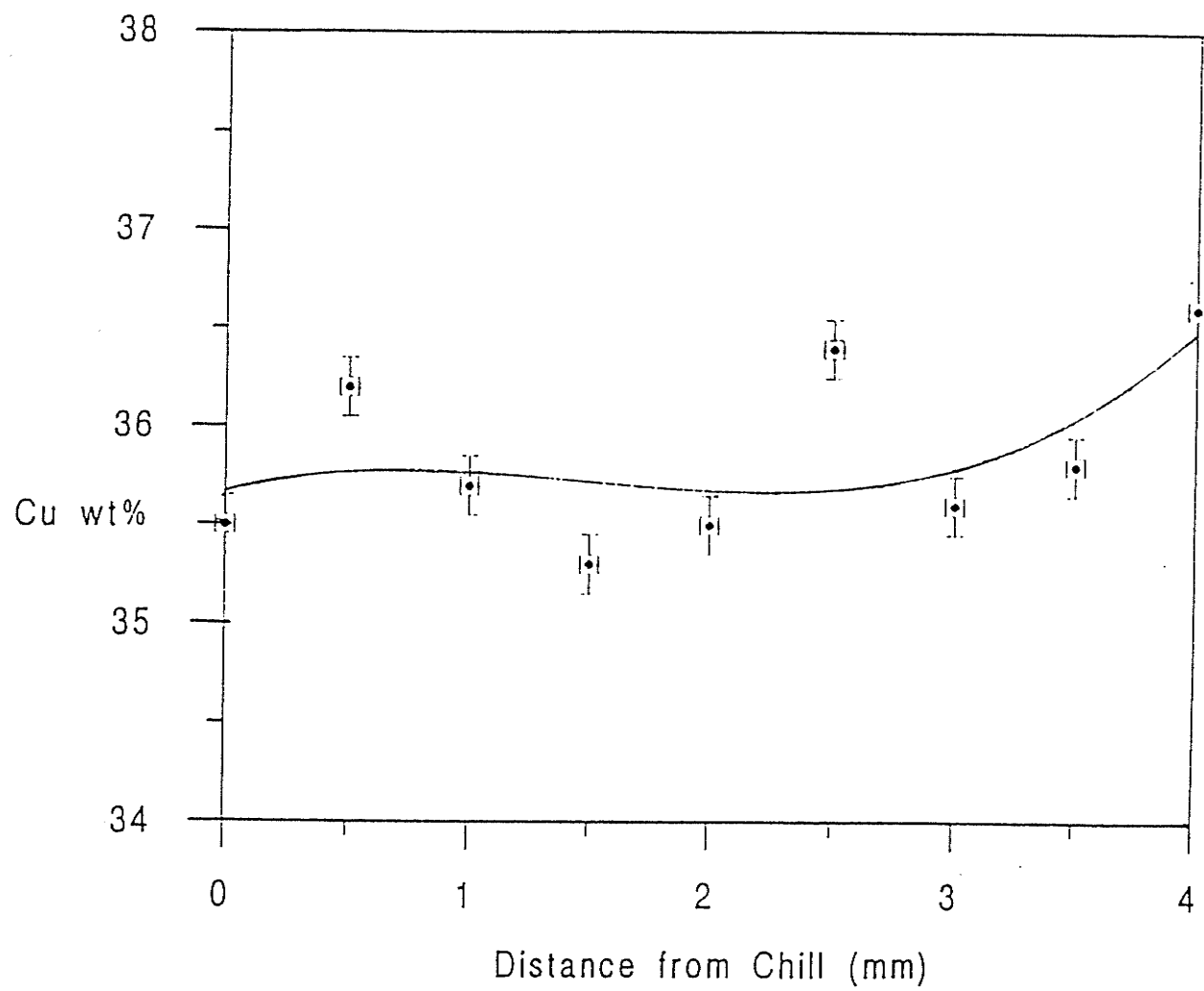


Figure 4.18

Macrosegregation of Al-36Cu 0G, KC-135 sample

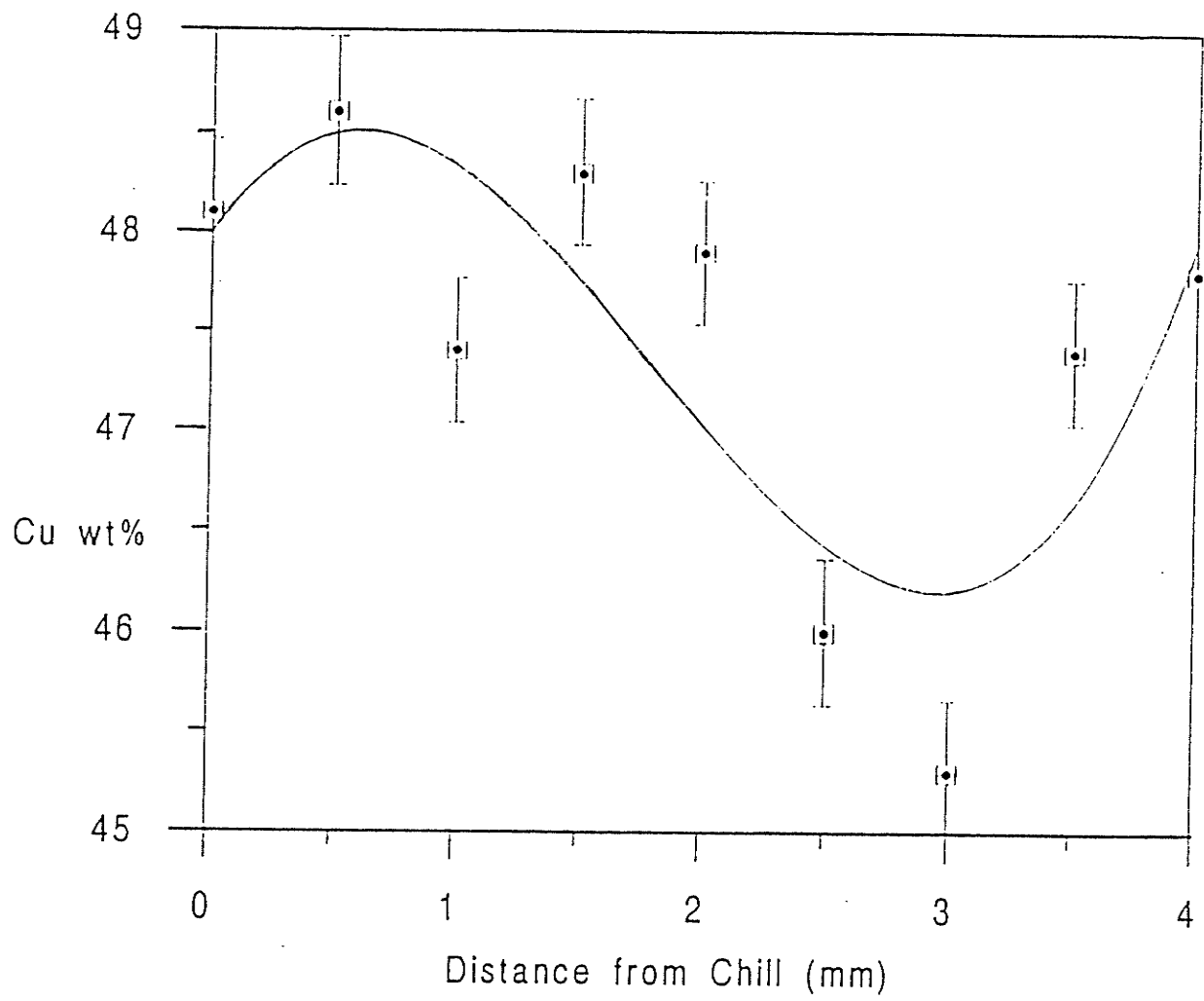


Figure 4.19

Macrosegregation of Al-47Cu 0G, KC-135 sample

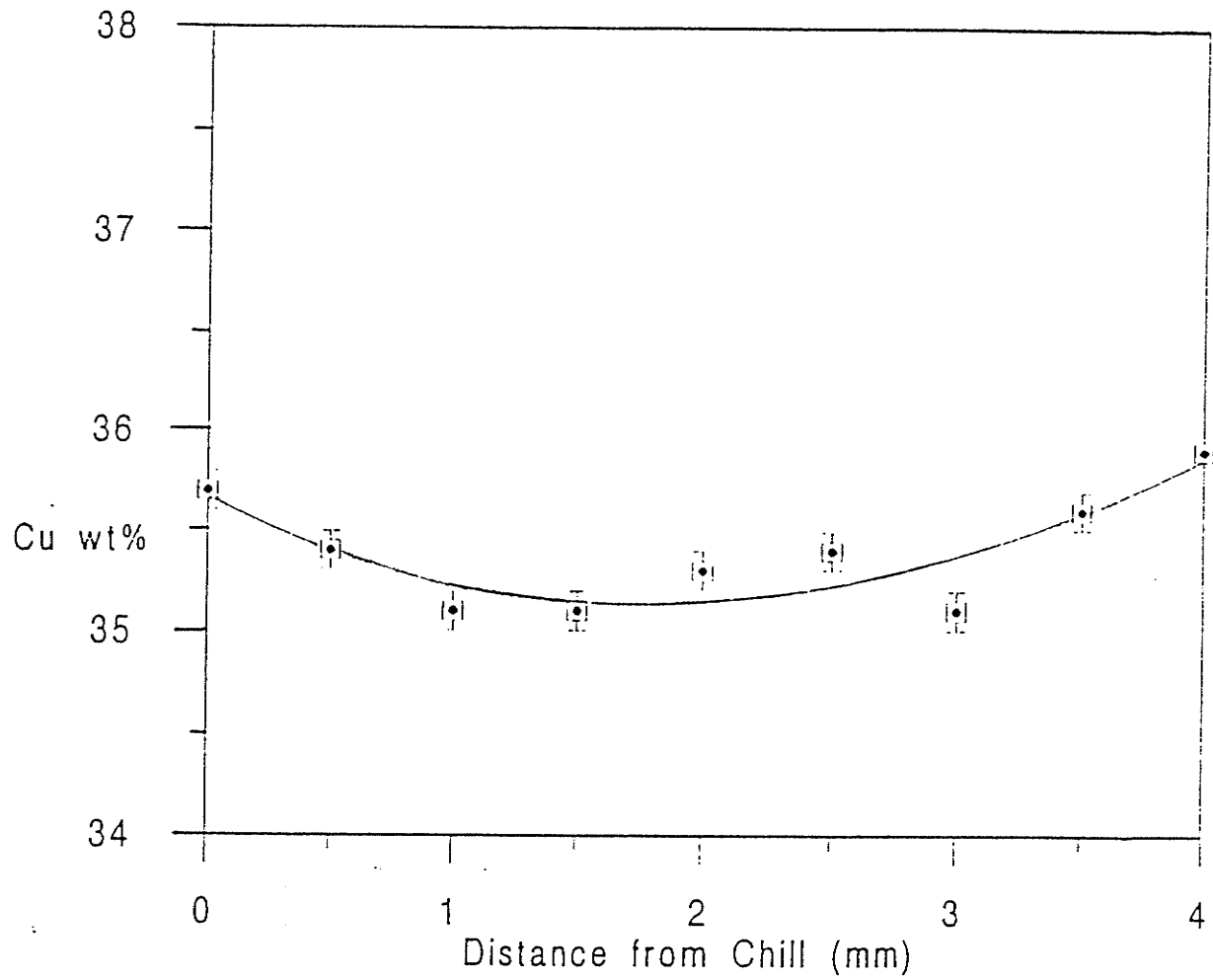


Figure 4.20

Macrosegregation of Al-36Cu 1.8G, KC-135 sample

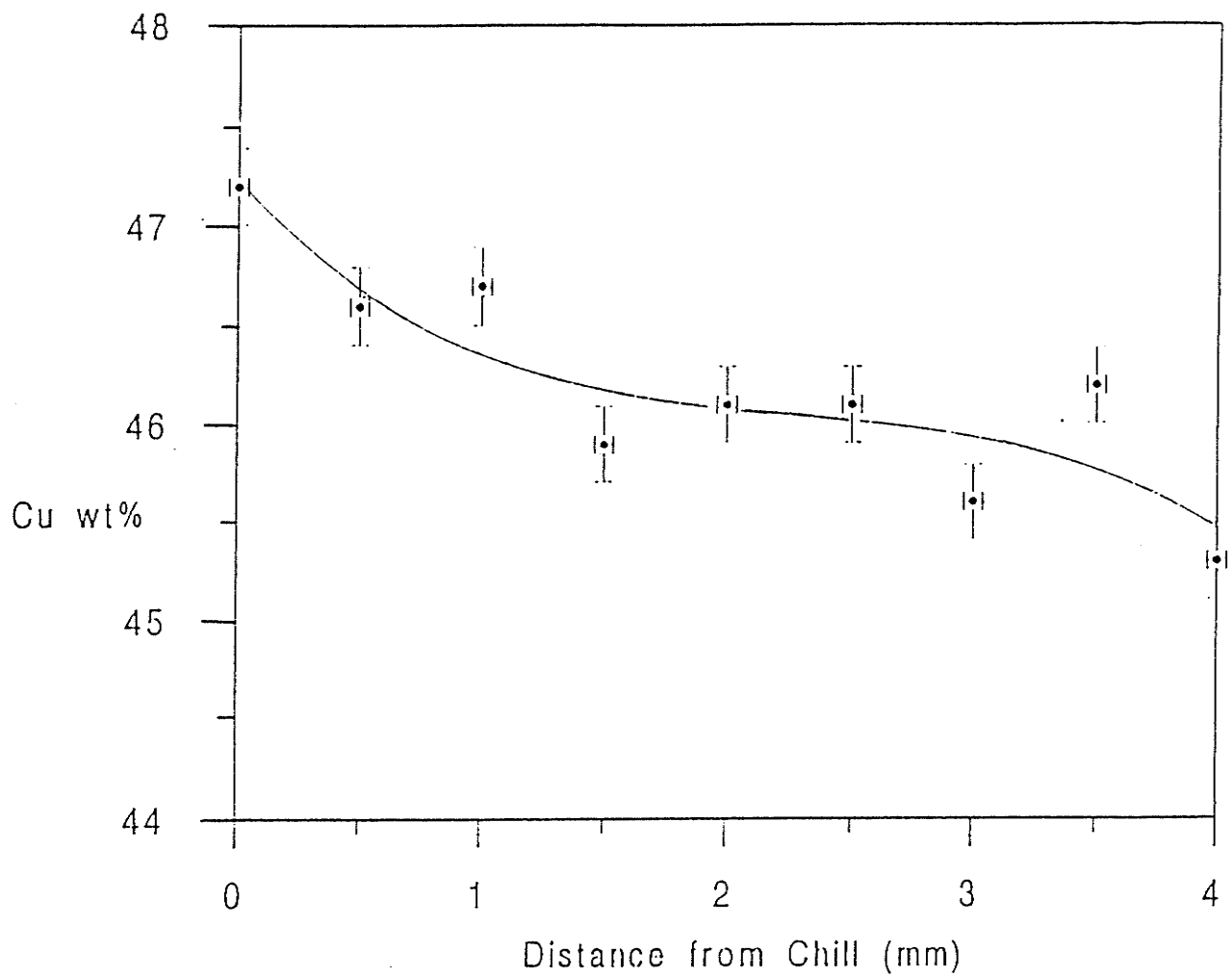


Figure 4.21

Macrosegregation of Al-45Cu 1.8G, KC-135 sample

4-6-3 DENDRITIC ARM SPACINGS

The primary arm spacings between growing θ phase measured from the longitudinal sections of Al-36%Cu samples in 0 and 1.8 G are summarized in Table(4-9). Measurements were carried out by counting the number of the aligned primary θ phase intersected with the perpendicular 10 mm line at the chill and at the other end respectively. For Al-45%Cu and Al-47%Cu samples, primary θ phase is heavy faceted, primary arm spacings can not be measured by this method.

It is noticed that in 0G the primary arm spacings at chill and at the other end are similar. However, at 1.8G the primary arm spacings at chill are much smaller than that at the top. Moreover, smaller spacing in higher gravity is noticed. More experimental data is need to explain the observed phenomenon.

Table 4-9 Primary arm spacings of KC-135 Al-36%Cu ingot

Al-36%Cu	0 G	chill	38.2 $\mu\text{m} \pm 1 \mu\text{m}$
		top	48.1 $\mu\text{m} \pm 1 \mu\text{m}$
	1.8 G	chill	18.3 $\mu\text{m} \pm 1 \mu\text{m}$
		top	42.0 $\mu\text{m} \pm 1 \mu\text{m}$

4-7 Attachment Energy for Solid-liquid Interfaces of Al₂Cu

The attachment energy for solid-liquid interfaces of Al₂Cu has been studied by N. Apaton[7]. Al₂Cu crystallizes in a body centred tetragonal crystal structure with the space group I4/mcm, whilst the lattice parameter a and c are 0.6066nm and 0.4874nm, respectively. The unit cell consists of 12 atoms placed on alternating layers of Al and Cu atoms. In the Al layer, the layer is rotated so that two Al atoms share a Cu atom at the corner of the unit cell. The Al atoms change their positions on the subsequent Al layer by a rotation of 90 degrees which makes the unit cell of Al₂Cu complex. The position of the Al and Cu atoms in each layer in the unit cell of Al₂Cu is shown in Figure(4-24).

The Al₂Cu phase(θ) melts at the relatively low temperature of 864K, and it has a narrow solute solubility range. These intrinsic properties of the intermetallic compound favour an ordered structure developing upon freezing from its own melt. Assume the first couple of liquid layers in front of the interface match with the crystal structure for the solid. A regular associated solution (RAS) model has been suggested, in which the interaction between like and unlike atoms is considered to form a short range ordering in the melt.

First, the coordination of the numbered atoms in the unit cell are analyzed. The interatomic distances between the first and second neighbours are considered. The pair-bond energies of Al-Al, Al-Cu and Cu-Cu in both liquid and solid states are calculated according to Swalin's equation[80]

$$H_s = N Z H_{AA} / 2 \quad (4-4)$$

where Z is the coordination number, N is the Avogadro number(6.023×10^{23}), H_s is the sublimation energy, and H_{AA} is the bond energy for the pair A-A. The sublimation energy for Al and Cu are 76.2 Kcal/mole and 80.7 Kcal/mole[81], respectively. The bond energy between Al and Cu atoms in the solid state is estimated by[80]:

$$\Omega = [H_{AB} - (H_{AA} + H_{BB})/2] Z N \quad (4-5)$$

where Ω is the interaction parameter, and H_{AB} is the bond energy between unlike atoms. Ω is related to the heat of solution ΔH , and the atomic concentration of the constituents in the solid solution by

$$\Omega X_A X_B = \Delta H \quad (4-6)$$

where X_A and X_B present the atomic concentration of Al and Cu in the solid. In the α phase at 0.9 at%Cu, $\Delta H = -1700$ cal/g atom, so that, equation(4-6) gives $\Omega = -18888$. Inserting this value into equation(4-4) as H_s and taking the evaporation energies for Al and Cu as 69.6 and 73.3 (Kcal/mole)[81], the bond energies for Al-Al and Cu-Cu pairs in their melt are $8.05(10^{-20}J)$ and $8.478(10^{-20}J)$, respectively. Using the enthalpy of mixing as -2600 cal/g.atom [82], the interaction parameter, Ω , for liquid atoms is found to be -11700. The bond energy for the Al-Cu pair yields:

$$H_{(Al-Cu)} = 8.94 \times 10^{-20} J.$$

Upon the transfer of liquid atoms onto the solid phase, the net change in bond energy is taken as the difference between each type of bond in the solid and liquid states. The attachment energy for various planes is calculated by using the L&J potential equation[80]:

$$E_{L(ij)} = \epsilon_{ij}/(n-m) [m(l_{ij}^0/l_{ij})^n - n(l_{ij}^0/l_{ij})^m] \quad (4-7)$$

Here ϵ_{ij} is the potential energy, l_{ij}^0 is the equilibrium interatomic distance, l_{ij} represents the interatomic distances for various bonds in the compound phase, the n and m are 12 and 6, respectively. After phase transformation, the L&J potential energy is determined for various bonds. The attachment energies calculated for the {110}, {002}, {112}, {211}, {020} and {022} solid-liquid interface planes are presented in Table (4-10). According to the results, the (112) and (110) planes are expected to be the most likely facet forming planes during growth, because of the lower attachment energy.

Table 4-10. Attachment energy for a group of Al₂Cu atoms for various solid-liquid interface planes[7].

Interface	110	002	112	211	020	022
EU($10^{-20} J$)	3.5	9.4	2.8	7.3	6.3	8.9

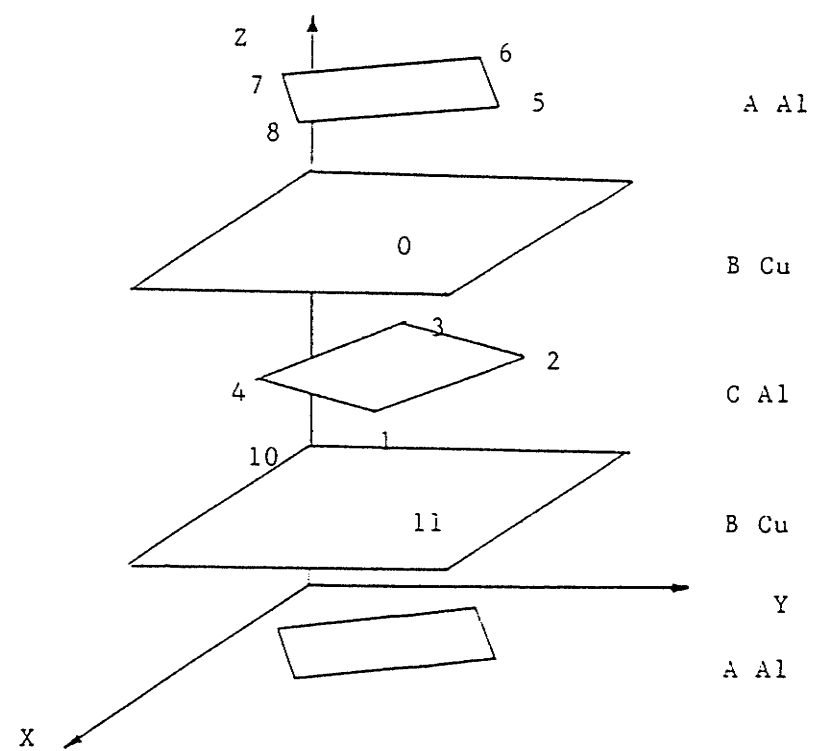


Figure 4-22

The unit crystal structure of Al_2Cu intermetallic compound. A, B, and C indicate the Al, Cu and Al atomic layers, respectively[7].

4-8 Effects of Convection on Al₂Cu growth

It has been suggested[83] that the convective mixing present in a ground-based sample breaks off the dendrite arms of the θ phase and distributes them through the melt to provide nuclei for the growth of more θ phase particles. An analysis is undertaken to compare the convection induced, shear flow with the strength of the material by assuming that the force required to break the dendrites is comparable to that produced by the shear flow at the solid-liquid interface. This situation is shown schematically in Figure(4-25). The shear stress at the surface increases with crystal size so that this constraint would self-limit the process. The terminal size of the crystals could result from the effects of natural convection.

The shear stress at the surface is due to buoyancy driven, natural convection around the growing crystal[84]. This flow is caused by density differences between the fluid adjacent to the surface of the object and the bulk solution far from the crystal. The strength of the motion is characterized by the Grashof number, the ratio of the buoyancy force driving the motion to the viscous resistance. The Grashof number is defined as[85]:

$$G_r = R^3 g \Delta\rho / \rho_\infty \nu^2 \quad (4-8)$$

where g is the gravitational acceleration, $\Delta\rho$ is the density difference, ρ_∞ is the bulk fluid density, ν is kinematic viscosity and R is the crystal's radius. The ratio of the molecular transport coefficients for momentum and diffusion is called the Schmidt

number, $S_c = v/D$, where D is the diffusion coefficient for the solute. For the Al-Cu system, $\Delta\rho=0.05(\text{g}/\text{cm}^3)$, $\rho_\infty=3.45(\text{g}/\text{cm}^3)$, $v=2.9\times10^{-7}(\text{m}^2/\text{sec})$ and $D=4\times10^{-9}(\text{m}^2/\text{s})$. If $R=100(\mu\text{m})$, then the Grashof number is about 2 whereas the Schmidt number is approximately 73. For a relatively small Grashof number but large Schmidt number, the motion scales on the $(G_r/Sc)^{1/2}$ is due to boundary layer structure of the flow. In a weak flow of this sort, the characteristic speed, μ_∞ , is given by[85]

$$\mu_\infty = (G_r/Sc)^{1/2} v/R \quad (4-9)$$

and the shear rate

$$\Gamma = \mu_\infty / \delta \quad (4-10)$$

where δ is the boundary layer thickness. The shear stress at the surface is determined by

$$\tau = \mu \Gamma = \mu \mu_\infty / \delta \quad (4-11)$$

where μ is the fluid viscosity, which is about $0.01\text{g}/\text{cm}\cdot\text{sec}$ for liquid metal. Thus, the characteristic speed is around $5(10^{-4} \text{ m/sec})$. Take δ as $1(\mu\text{m})$ so that the shear rate is about $500(\text{s}^{-1})$. The shear stress acting on the crystal surface calculated from equation(5-8) is approximately 0.5 pa. If the θ phase dendrite is a cube of $50\mu\text{m}$, the shear force acting on a surface ($F=\tau A$) is approximately 10^{-9} N .

The ultimate tensile strength of an Al-Cu alloy at a high 800K temperature is

close to 20 MN/m². The shear strength is about 70~75% of the tensile strength so that the shear strength is around 14 MN/m² (14 X 10⁶ Pa)[86]. The stress generated by free convection is approximately several orders of magnitude too small to break off any side arms.

Another possible approach is to compare the torque at the solid surface with the solid-liquid interface attachment energy. The following model has been suggested by W.B. Russel[85] and it has been used to investigate the possibility of shear-induced denaturation of protein crystals. For the θ phase to grow, the Al and Cu atoms must be in a particular conformation in order to bind to the crystal surface. Crystal growth will be hindered if the shear stress changes the atomic conformation. Consider the spherical nucleus shown in Figure(4-26), and assume it is "hinged" at point B, which is close to the cylinder wall. Suppose the nucleus is held stationary in a uniform flow field of strength μ_∞ . The force F at point A will be estimated from[85]:

$$F = 3\pi R \mu_\infty / 2 \quad (4-12)$$

where R denotes the radius of the nucleus (100 μm).

From equation(4-8), the interface attachment energy is characterized as a function of the interatomic distances, l_{ij} . The weakest bond energy occurred at interface (112) and (110) at approximately 3(10⁻²⁰ J). By taking the interatomic distances (r) close to 0.3(10⁻⁹m), the breaking force (where $F = -dE_l/dr$) is about 1.2(10⁻¹⁰ N). A speed, μ_∞ , of approximately 3(10⁻⁴m/s) is required to disrupt the atomic

bonding at the interface. This speed is comparable in magnitude to the free convection speed estimated earlier. This similarity suggests that the viscous stresses due to natural convection are sufficiently high to disturb the atoms as they approach the surface.

As before, assume that the free convection speed is about $5(10^4 \text{m/sec})$ and the braking force is $1.2(10^{-10} \text{ N})$, so that the maximum size of the θ phase estimated from equation(4-10) is $50\mu\text{m}$. From the transverse section of the ground based sample shown in Figure(4-10), it is evident that the θ phase present in the sample has comparable size to the estimated one.

The θ phase growth can be described in the following two steps: (1) the atoms reach the surface from the bulk solution; and (2) the atoms are incorporated into the crystal. From the above argument, it is clear that the viscous stress due to natural convection disturbs the atoms so that they will not incorporate into the crystal after reaching a certain size. Instead of breaking the dendrite arms of θ phase, the convective mixing promoted the dilution of the melt at the interface and increased the instability. The growth of the primary θ phase is diffusion controlled and, therefore, the convective mixing favours a faceted θ phase morphology. The viscous stress due to natural convection retarded the θ phase growth and controlled the size of the facets. Furthermore, the physical movement of the nucleation sites, due to the natural convection, may provide additional nuclei for the growth of more θ phase particles. Therefore, the θ phase particles in the ground-based sample are smaller, more numerous and more finely spaced than the corresponding phase particles in the space sample.

Further systematic directional solidification experiments in relation to orientation relative to the gravity vector \mathbf{g} , and different solidification conditions are necessary to investigate the effect of gravity and convection on the alloy structures and segregations.

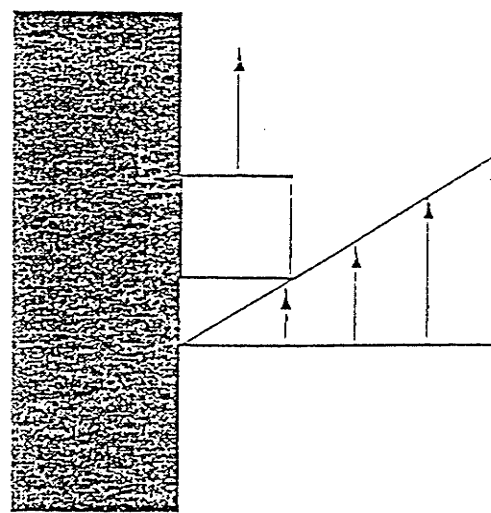


Figure 4-23

Mechanisms by which shear flow may remove dendrite from the primary surface[84].

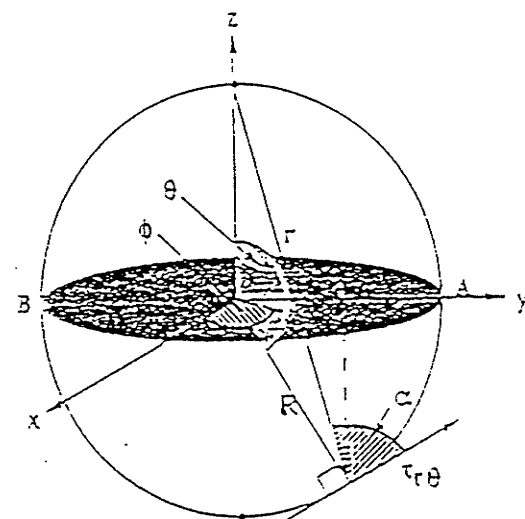


Figure 4-24

Model for calculating the torque at point A due to shear stress[84].

CHAPTER V

CONCLUSIONS

In the present study, the solidification behaviour of hypereutectic Al-Cu alloys having a composition range from Al with 36wt% to 50wt% Cu have been examined under various solidification conditions. The following conclusions have been drawn.

- (a). The morphology of the Al_2Cu primaries showed a gradual transition from non-faceted to faceted crystals with increasing Cu content and decreasing cooling rate. Growth of primary θ phase is diffusion controlled, and, therefore, the instability of the interface is promoted by the dilution of the melt.
- (b). The large tree like primary θ phase observed in KC-135 samples and QUESTS space sample are due to lack of convection in microgravity environment.
- (c). The presence of convective mixing in the ground based sample promoted the faceted θ phase morphology and retarded the dendritic growth. The physically moving of the nucleation sites due to the natural convection may provide more nuclei for the growth of more θ phase. Therefore, the ground based sample will exhibit more but smaller and more smoother θ phase particles than the space sample.
- (d). The effect of convective mixing on the inter θ -phase eutectic spacings and the eutectic fault line spacings is small, due to the simultaneous growth of both

θ phase and α phase lamellas.

(e). Gravity is the major cause of segregation for vertically upwards solidification. However, phase change effects and buoyancy effects are also contribution factors. Macrosegregation phenomenon may change with alloy composition and cooling rate depends on which effect predominates.

(f). Lack of convection in the microgravity environment has resulted in the reduced fluid motion which allowed larger dendrites to grow. During dendritic solidification the flow of the interdendritic liquid is due solely to solidification shrinkage, which is compensated mostly by the deformation of the ingots. The macrosegregation is insignificant in QUESTS microgravity environment.

In the future, systematic directional solidification experiments should be carried out in relation to the orientation relative to the gravity vector, g , and different solidification conditions, in order to investigate the effect of gravity and convection on the alloy structures and segregations. Based on the experimental data, the mechanism and mathematic model on dendritic growth will be achieved. The dendritic spacing and segregation in the ingot after solidification can be predicted.

REFERENCES

1. Bruce Chalmers, Transactions AIME, May 1954, pp 519-532
2. Bruce Chalmers, Principles of Solidification, John Wiley and Sons Inc., New York, (1964)
3. W. C. Wingard, An Introduction to the Solidification of Metals, Institute of Metals, London, (1964)
4. Merton C. Flemings, Solidification Processing, Mc Graw Hill Inc., New York
5. I. Minkoff, Solidification and Cast Structure, John Wiley and Sons, New York, (1986)
6. Metals Handbook, 9th Edition, Vol 15, American Society for Metals, Metal Park, Ohio, (1988), pp 101-158
7. N. Apaydn and R. W. Smith, Queen's University, Solidification Morphology of Al₂Cu in Hypereutectic Al-Cu Alloys. Phd. Thesis
8. M. E. Gilksman, R. J. Schaefer and J. D. Ayers, Metall. Trans, A. Vol 7A, (1976), pp1747-1759
9. T. F. Bower, H. D. Brody and M. C. Flemings, Trans. AIME, (1960), Vol.236, pp624-634
10. M. H. Burden and J. D. Hunt, J. Cryst. Growth (1974), Vol 22, pp99-108
11. T. Bower, H. Brody and M. C. Flemings, Trans. TMS-AIME (1966), Vol.236, pp624

12. C. Zener. Trans AIME (1946), Vol. 167, pp550
13. R. Trivedi, J. Cryst. Growth (1980), Vol. 49, pp219-232
14. W. Kurz and D. J. Fisher, Acta Metall. Trans. A, (1985) Vol. 16A, pp1799
15. Yasunori Miyata and Toshio Suzuki, Metal. Trans. A, (1985) Vol. 16A, pp1807-1814
16. Yasunori Miyata, Toshio Suzuki and Jun-Ichi Uno, Metal. Trans A, Vol. 16A, (1985) pp1799-1805
17. K. P. Youg and D. H. Kirkwood, Metal. Trans A. Vol. 6A, (1975) pp197-205
18. Hillig, W. B. Acta Metall. (1966), Vol. 14, pp1868
19. Keith, H. D. and Padden, Jr., F. J. J. Appl. Phys., (1963), Vol. 34, pp2409
20. G. A. Chadwich, J. Inst. Met. (1963), Vol. 91, 169 and Vol. 92, pp18
21. R. W. Craft, Trans. Met. Soc. AIME (1962), Vol 224, pp65
22. K. A. Jackson and J. D. Hunt, Trans. AIME. (1966), Vol. 236, pp1129
23. T. Sato and Y. Sayama, J. Crystal Growth. (1974), Vol. 22, pp259
24. Hieoshe Kato and J.R. Cahoon, Met. Trans. A. Vol. 17A, pp823
25. J.R. Cahoon and H.W. Paxton, Trans. TMS-AIME, Vol. 245, pp1401
26. Y. Miyata, T. Suzuki and J.I. Uno, Met. Trans. A, (1985) Vol. 16A, pp1799-1805
27. Yasumori Miyata and Toshio Suzuki, Met Trans. A, (1985), Vol, 16A, pp1807-1814

- 28.** B.A. Mueller, Materials Sci. and Eng., (1988), Vol. 98, pp153-156
- 29.** M.D. Dupouy, D.Camel and J.J.Favier, Acta Metall., (1989), Vol. 37, pp1143-1157
- 30.** C.Y. Liu, K. Murakami and T. Okamoto, Materials Sci. and Eng., (1987), Vol. 96, pp259-265
- 31.** C.Y. Liu, K.Murakami and T. Okamoto, Materials Science and Engineering, (1989), Vol. A 108, pp265-270
- 32.** Flemings, M. C. and G. E. Nereo, Trans. AIME, (1967), Vol. 239, pp1449
- 33.** R. M. Sharp and A. Hellawell, J. Crystal Growth, (1970), Vol, 6, pp253-260
- 34.** Brower T. F., Brody, H. D. and Flemings, M. C., Trans. AIME, (1966) Vol.236, pp624
- 35.** Brody, H. D. and Flemings, M. C., Trans. AIME. Vol. 236 (1966), pp615
- 36.** Sharp, R. M. and Hellawell, A. J. Crystal. Growth, (1970), Vol. 6, pp253
- 37.** Harold D. Brody and Merton C. Flemings, Trans. AIME.,(1966), Vol. 236, pp615
- 38.** Theodoulos Z. Kattamis and Merton C. Flemings, Trans, AIME, (1965), Vol.233, pp992
- 39.** T. W. Clyne and W. Kurz, Metal. Trans. A. (1981), Vol. 12A, pp965
- 40.** J. A. Sarraeal and G. J. Abbaschian, Metall. Trans. A. (1986), Vol. 17A, pp2063
- 41.** B. Giovanola and W. Kurz, Metal. Trans. A., (1990), Vol. 21A, pp260

- 42.** Stefanos M. Skolianos, Zeitschrift Fuer Metallkde, (1991), Vol. 82, n2, pp89-95
- 43.** D. J. Allen and J. D. Hunt, Metall. Trans. A., (1979), Vol. 10A, pp1389-1397
- 44.** D. E. Adams, J. Inst. Met. (1948-1949), Vol. 75, pp805
- 45.** J. S. Kirkaldy and W. V. Youdelis, Trans. Met. Soc. AIME, (1958), Vol. 212, pp833
- 46.** E. Scheil, Metall for Schung, (1947), Vol. 2. pp69
- 47.** W. V. Youdelis, D. R. Colton, Trans. TMS-AIME, (1960), Vol. 218, pp628-631
- 48.** J. R. Cahoon, A Re-evaluation of Inverse Segregation in Al-Cu System, Submitted for Publication
- 49.** M. C. Flemings and G. E. Nereo, Trans AIME, (1967), Vol. 239, pp1449-1461
- 50.** M. C. Flemings, R. Mehrabian and G. E. Nereo, Trans. TMS-AIME (1968), Vol. 242, pp41-49
- 51.** M. C. Flemings and G. E. Nereo, Trans. TMS-AIME, (1968), Vol. 242, pp50
- 52.** J. R. Cahoon and W. V. Youdelis, Trans TMS-AIME, (1968), Vol. 242, pp757-759
- 53.** J. R. Cahoon and W. V. Youdelis, Trans. TMS-AIME, (1964), Vol. 230, pp1734

- 54.** Fariba Saadat, University of Manitoba, The Effect of Gravity Convection on Segregation and Microstructure in Binary Alloys.
- 55.** N. Streat and F. Weinberg, Metall Trans, A. (1974), Vol. 5A, pp2539-2548
- 56.** L. Wang, V. Laxmanan and J. F. Wallace, Metall. Trans. A, (1988), Vol. 19A. pp2687-2694
- 57.** S. Ganesan an D. R. Poirier, Metall. Trans. A. (1987), Vol. 18A, pp721-723
- 58.** M. D. Dupouy, D. Camel and J. J. Favier, Acta Metall. (1989), Vol. 37, pp1143-1157
- 59.** D.J. Allen and J.D. Hunt, Metall. Trans. A, (1979), Vol. 10A, pp1389-1397
- 60.** C. Beckermann and R. Viskanta, Int. J. Heat Mass Transfer, (1988), Vol. 31, pp69-79
- 61.** C. Beckermann, R. Viskanta and S. Ramadhyani, J. Fluid Mech. (1988) Vol. 186, pp257-284
- 62.** W.D. Bennon and F.P. Incropera, Int. J. Heat Mass Transfer, (1987), Vol. 30, pp2171-2187
- 63.** M.E. Thomposon and J. Szabolcs, J. Fluid Mech. (1988), Vol. 187, pp409-433
- 64.** Wei Shyy and Ming-Hsiun Chen, Int. J. Heat Mass Transfer, (1990), Vol.33, pp2565-2578

- 65.** R. Mehrabian, M. Keane and M.C. Flenings, Metall. Trans. (1970), Vol.1, pp1209-1220
- 66.** M. Simpson and M. C. Fleming, Metall Trans, (1984), Vol. 15A, pp2095-2097
- 67.** A.L. Maples and D.R. Poirier, Metall. Trans. B, (1984), Vol. 15B, pp163-172
- 68.** M.D. Dupouy, D.Camel and J.J. Favier, Acta. Metall. Vol. 40, (1990), pp1791-1801
- 69.** P.W.Wilson, T.Z.Kattamis and Y.Shiohara, J. Material Science,(1988), Vol. 23, pp2882-2892
- 70.** B. Feuerbacher, H.Hamacher and R.J. Naumann, Materials Sciences in Space, (1986), Springer-Verlag Berlin
- 71.** Doru M. Stefanescu, Peter A. Currerl and Michael R. Fiske, Metall. Trans, A. (1986), Vol. 17A, pp1121
- 72.** D. Thevenard and H.B. Hadid, Int. J. Heat Mass Transfer, Vol. 34, pp2167-2173
- 73.** Mary H. Johnston and Carolyn S. Griner, Metall. Trans. A. (1977), Vol. 8A, pp77
- 74.** Heinz J. Sprenger, Directional Solidification of a Eutectic Alloy Results for The D-1 Experiment, Proc. 6th European Symposium on Material Sciences and Microgravity Conditions, Bordeaux, France. 1986 pp2-5 (ESA-SP-256, Feb 1987)

- 75.** N.V.Stoichev, S.B.Yaneve, L.L.Regel and I.M.Safonova, Appl. Microgravity Tech. II. (1990), 4, pp181-185
- 76.** P.A. Curreri, J.E.Lee and D.M.Stefanescu, Metall. Trans. A. Vol. 19A, (1988), pp2671-2676
- 77.** Hans M. Tensi, Metall. Trans. A, (1988) Vol. 19A, pp2681
- 78.** Z. Huang, Scripta Metall, (1991) Vol. 25, pp149-152
- 79.** J.J. Favier, J.Berthier, Ph. Arragon, Y.Malmejal, V.T.Khryapov and I.V.Barmin, Acta Astronomica, (1982), Vol. 9, No.4, pp255-259
- 80.** R.A. Swalin, Thermodynamics of Solids, John Wiley & Sons, New York, (1962)
- 81.** O. Kwasniewski and C.B. Alcock, Metallurgical Thermochemistry, Pergamon Press, New York, (1975)
- 82.** R. Hultgren, R.L. Orr. P.P. Anderson, and K.K. Kelly, Selected Values of Thermodynamic Properties of Metals & Alloys, John Wiley & Sons, New York, (1963)
- 83.** K.N. Tandon, Hong Yu, J.R. Cahoon and M.C. Chaturvedi, Solidification Behaviour of A Hyper-eutectic Al-Cu Alloy in Microgravity- A Space Shuttle Experiment, Spacebound'93, Canadian Space Agency
- 84.** M.L. Grant and D.A. Saville, J. Crystal Growth, (1991), Vol, 108, pp8-18
- 85.** S. OStrach, Ann. Rev. Fluid Mech. (1982), Vol, 14, pp313
- 86.** L.F. Mondolfo, Aluminum Alloys: Structure & Properties, Butter Worths,

London-Boston, (1979), pp704

87. R. Kohli, P.L. Brusky, S. Diamond, A.J. Markworth, Microgravity Materials Processing for Commercial Applications, Met. Res. Soc. Symp. Vol. 87, (1987), pp183-196

88. G. Tyc and D. Gates, QUESTS- A Microgravity Research Facility for Material Science Experiments, Proceedings Second Workshop on Microgravity Experimentation, May 8-9, 1990, Ottawa, Canada, pp61

89. S.M. Pimputkar and S. Oatrach, J. Crystal Growth (1981), Vol. 55, pp614-640